From mine-face to micron-scale investigation of the Cretaceous McMurray Formation at Kearl Mine, northeastern Alberta, Canada

by

Trevin Ferens

A Thesis

Submitted to the Faculty of Graduate Studies of

The University of Manitoba

in partial fulfillment of the requirements for the degree of

MASTER OF SCIENCE

Department of Earth Sciences

University of Manitoba

Winnipeg, Manitoba

ABSTRACT

River meander-belt morphodynamics are critical to understanding fluvial sedimentology, however, the process-to-product relationships are highly complex. Fluvial deposit heterogeneity is observed in dense and comprehensive subsurface data sets within hydrocarbon reservoirs where accurate subsurface modelling is essential for successful mining and drilling projects. Despite the available information, localized modelling discrepancies are still commonplace, often occurring between boreholes where data is lacking. Unmodelled mudstone-rich deposits are of particular importance, as fine-grained deposits are impermeable and limit hydrocarbon saturation and mobility.

To improve understanding of meander belt heterogeneity and depositional processes this thesis investigates the Lower Cretaceous McMurray Formation at Kearl mine, northeastern Alberta. The research objectives are to i) utilize extensive mine-face exposures by integrating them with related borehole data to reconstruct the local paleoenvironment, ultimately interpreting the paleochannel morphodynamic evolution through time; and ii) investigate fluvial mudstone microstructure of point-bar mudstones from Kearl mine using scanning electron microscopy (SEM).

The area of interest at Kearl mine is a 1.9 x 1.1 km area that was excavated from May 2022 to August 2023. The mine-faces here were continuously excavated while on-site geologists documented notable geologic features. The studied interval of this research is an approximately 20-meters-thick channel-belt deposit that comprised nine architectural elements including four

point bars, three counter-point bars and two abandoned-channel fills. A focus of the study is the atypical channel-belt deposit trends observed in one of the point bars.

The atypical point-bar deposits comprise inclined heterolithic stratification (IHS) that was interspersed with mudstone clast breccias and mudstone-lined trough cross-bedded sandstone. The deposits were localized in a segment of the point bar that did not conform to upward- nor downstream-fining trends in typical point-bar models. To better understand these peculiar deposits, this research produces and utilizes a planform reconstruction to investigate the fluvial processes that occurred during the atypical deposition, noting that the upstream cutbank material was mudstone-rich and may have influenced the atypical point-bar heterogeneity. Furthermore, a mudstone sample downstream from the atypical deposits is analyzed with SEM to observe microstructure characteristics, which reveals evidence of sub-mm-sized mudstone aggregates. The presence of these micron-scale mudstone aggregates implies that a broader range of hydrodynamic conditions should be considered for fluvial mudstone deposition, particularly the mudstone component of point-bar IHS.

ACKNOWLEDGEMENTS

I would like to thank my advisor Dr. Paul Durkin for guiding me through my undergraduate thesis and now master's thesis. His continued tutelage has been of the utmost value. Thanks to B. Joan Carter and Dr. Bogdan Varban for sharing their geologic expertise over the last three years and helping to integrate me with the wonderful geoscience team at Imperial. Thanks to Chad Sisulak for supervising my project and giving me the opportunity to work as a site geologist at Kearl mine. Thanks to fellow site geologists Andrea Morgan, Phillip Labrecque, Brandon Hogberg, Jamie Neil and Sam Metteer for being outstanding coworkers and their contributions to assembling and maintaining the vast outcrop photograph library at Kearl. Thanks to Dr. Ricardo Silva and Dr. Guy Plint for their valuable input on the preparation and evaluation of mudstone microstructure.

CONTRIBUTIONS OF AUTHORS

Authorship of chapter two in this thesis is credited to Trevin Ferens and Dr. Paul Durkin. The research and contents of chapter two were produced by Trevin Ferens, and reviews and guidance were provided by Dr. Paul Durkin.

Authorship of chapter three of this thesis is credited to Trevin Ferens, Dr. Paul Durkin and Dr. Ricardo Silva. The research and contents of chapter three were produced by Trevin Ferens, and reviews and guidance for chapter three were provided by Dr. Paul Durkin. Guidance for sections 3.3 - 3.5 of chapter three was provided by Dr. Ricardo Silva.

TABLE OF CONTENTS

LIST OF TABLES

Chapter 2

Chapter 3

LIST OF FIGURES

Chapter 2

Chapter 3

CHAPTER ONE:

INTRODUCTION

1.1. Research Motivation

Meandering rivers are the driving force behind channel-belt deposits, a dominant depositional system on the surface of the Earth (e.g., Sylvester et al., 2017; Shan et al., 2018). Therefore, accurately prescribing the 3-D distribution of modern and ancient meander-belt deposits is beneficial in several branches of global advancements (Rosenshein, 1988). For example, understanding of subsurface lithofacies distributions, and therefore fluid flow interactions, helps to investigate water resources (Larkin and Sharp, 1992; Nyberg et al., 2013) and the fate of harmful subsurface contaminants (Worman et al., 2007). Additionally, the energy industry benefits significantly from precise modelling capabilities that enable efficient planning and execution of hydrocarbon resource extraction, and subsequent environmental reclamation projects within fluvially-dominated subsurface reservoirs (e.g., Crerar and Arnott, 2007; Willis and Tang, 2010; Nardin et al., 2013; Martinius et al., 2017). The motivation for this research is improving model building and predictive potential in ancient and modern channel-belt sediments.

The Athabasca Oil Sands Region (AOSR) is a 93,000 km^2 area in northeastern Alberta comprising hydrocarbon-bearing stacked meander-belt deposits of the Lower Cretaceous McMurray Formation (Alberta Energy Regulator, 2023). Dense subsurface data sets are gathered here for pre-extraction 3-D modelling (e.g., Hein and Cotterill, 2006; Crerar and Arnott, 2007; Peng et al., 2022), but modelling difficulties are still common due to meander-belt heterogeneity (e.g., Jordan and Pryor, 1992) and the complex channel-belt stacking patterns in the McMurray Formation (Hein and Cotterill, 2006; Peng et al., 2024). Geologists risk potential errors when building model frameworks where localized and drastic lithofacies changes are present, and when borehole drill grids do not capture rapid transitions. Furthermore, modelling through

predictive distributions of lithofacies (i.e., stochastic modelling) may be erroneous if the deposit in question is atypical, and therefore not properly understood. Conversely, if the same atypical feature is sufficiently documented and subsequently typified by investigating the processes and paleoenvironmental conditions that produced its irregularity, it can be predicted in future characterizations even when missed by traditional data collection methods. In this research, atypical point-bar deposits within the Cretaceous McMurray Formation were examined at Kearl mine, northeastern Alberta.

At Kearl mine the 3-D subsurface model is verified by on-site geologists when the deposits are sequentially exposed during excavation. Once exposed the atypical deposits at Kearl mine contained segments of unmodelled heterolithic interbeds within high-energy structures (e.g., trough cross-bedding). Borehole data provides a 1-D intersection of these features which was incorrectly interpreted as fluctuating and low-energy, inclined heterolithic stratification (IHS) deposits. The modelling errors resulted in significant ore volume discrepancies from inaccurate data-driven geological interpretation. The presence of interbedded mudstone within trough cross-bedded deposits is not a well understood, nor documented, phenomenon. Furthermore, mudstone-clast dominated breccias are often localized thin packages, however, mudstone clast breccia is the dominant lithofacies in the lower 5 – 10 m of atypical deposits in the study.

The present research looks to investigate the processes leading to the atypical deposition described above. A possible explanation comes from growing evidence that suspended muds often travel as aggregates and can therefore be deposited in a wider range of hydrodynamic conditions (Bennett et al., 1991; Li and Schieber, 2018). Suspended mud-particle aggregation is pervasive in aquatic environments (Bennett et al., 1991), and flume experiments show that mud

aggregates may also travel as bedload in flowing water (Schieber et al., 2007). There is also evidence of mud aggregate deposition in ancient mudstone microstructure analyses using scanning electron microscopy (SEM) imaging (Plint, 2014; Laycock et al., 2017). If such aggregation exists in terrestrial systems, particularly in fluvial environments, a refinement in understanding ancient fluvial mudstone deposition may be needed. This includes the mudstone component of IHS (e.g., Thomas, 1987) deposits in point bars.

1.2. Research Questions

To address the research motivation, the research questions and objectives are as follows:

1) Using mine-face observations in tandem with subsurface data sets in Kearl mine, what methods can we employ to improve the predictive capabilities and understanding of depositional processes in the McMurray Formation and analogous fluvial deposits in the subsurface?

2) Can we observe fluvial mudstone microstructure in poorly indurated sediments of the Cretaceous McMurray Formation and, if successful, what do our results imply for sedimentological processes of fluvial mudstones?

To address the questions this research utilizes borehole data and McMurray Formation outcrop availability in Kearl mine. In the present study Kearl mine was fully accessible for a 16-month data collection period (May 2022 – August 2023), during which the removal of over 400,000,000 tonnes of subsurface material, primarily within the Cretaceous McMurray Formation, commenced. A detailed meander-belt reconstruction is created in a 1.9 x 1.1 km area of interest within the mine. Spatiotemporal evolution of the channel-belt is interpreted, therefore

defining the processes that lead to deposition. Attention was focused on the atypical point-bar deposits that are documented within the area of interest.

To investigate the mudstone microstructure, a mudstone sample was collected from the point bar containing atypical deposits and experimental techniques were performed to prepare the sample for SEM investigation using methods revised from previous work in Sanchez-Roa et al. (2018). The method includes saturating the sample with ultra-low viscosity epoxy resin (LR White) to view an undisturbed cross-section of the mudstone with SEM imaging. Furthermore, the results are compared and contrasted with previous research and SEM analyses on mudstone microstructure.

1.3. Research Organization

This thesis is organized into four chapters: chapter one is an introduction to the thesis topics, chapter two and three are presented as standalone papers that address research questions 1) and 2), respectively, and chapter four is an encompassing conclusion and discussion of potential future work stemming from this research. The overall premise of this thesis involves analyzing fluvial processes and resulting deposits in channel-belt sediments of the Early Cretaceous McMurray Formation.

Chapter 2 presents a comprehensive 3-D reconstruction of an approximately 20-meter-thick, 1.1 x 1.9 km area within Kearl mine, utilizing a data set of borehole and outcrop photograph data. Results include typical channel-belt features that strengthen current point-bar models. In addition, atypical point-bar deposits are noted and further discussed in detail. Chapter 3 comprises research based on a sampled mudstone deposited on the same point bar, immediately downstream from the atypical deposits discussed in Chapter 2, with an aim to investigate

microstructure properties using SEM imaging. Chapter 4 summarized the results of this research and organizes them into a fluvial process to sedimentary product evaluation that ranges from macro- to micro-scale. Further direction in research is also discussed, suggesting that future research can benefit from expanding on the conclusions herein.

1.4. References

Alberta Energy Regulator, (2023). Oil Sands Area Assessment. https://www.aer.ca/provi ding-information/data-and-reports/statistical-reports/st98/reserves/oil-sands-area -assessment.

Bennett, R.H., Bryant, W.R., Keller, G.H., (1981). Clay fabric of selected submarine sediments: fundamental properties and models. Journal of Sedimentary Petrology. 51(1), 217-232.

Crerar, E.E., Arnott, R.W.C., (2007). Facies distribution and stratigraphic architecture of the Lower Cretaceous McMurray Formation, Lewis property, northeastern Alberta. Bulletin Canadian Petroleum Geology. 55(2), 99-124.

Hein, F.J., Cotterill, D.K., (2006). The Athabasca Oil Sands – A regional geological perspective, Fort McMurray area, Alberta, Canada. Natural Resources Research. 15, 85-102.

Jordan, D.W., Pryor, W.A., 1992. Hierarchical levels of heterogeneity in a Mississippi River meander belt and application to reservoir systems: Geologic note 1. American Association of Petroleum Geologists Bulletin. 76 (10), 1601-1624.

Larkin, R.G., Sharp, J.M., (1992). On the relationship between river-basin geomorphology, aquifer hydraulics, and ground-water flow direction in alluvial aquifers. Geological Society of America Bulletin. 104(12), 1608-1620.

Laycock, D.P., Pederson, P.K., Montgomery, B.C., Spencer, R.J., (2017). Identification, characterization, and statistical analysis of mudstone aggregate clasts, Cretaceous Carlile Formation, Central Alberta, Canada. Marine and Petroleum Geology. 84, 49-63.

Li, Z., Schieber, J., (2018). Composite particles in mudstones: Examples from the Late Cretaceous Tunuk Shale Member of the Mancos Shale Formation. Journal of Sedimentary Research. 88, 1319-1344.

Martinius, A.W., Fustic, M., Garner, D.L., Jablonski, B.V.J., Strobl, R.S., MacEachern, J.A., Dashtgard, S.E., (2017). Reservoir characterization and multiscale heterogeneity modelling of inclined heterolithic strata for bitumen-production forecasting, McMurray Formation, Corner, Alberta, Canada. Marine and Petroleum Geology. 82, 336-361.

Nardin, T.R., Feldman, H.R., Carter, B.J., (2013). Stratigraphic architecture of a large-scale point bar complex in the McMurray Formation: Syncrude's Mildred Lake Mine, Alberta, Canada, *In* Hein, F.J., Leckie, D., Larter, S., Suter, J.R., (eds), Heavy-Oil and Oil-Sand Petroleum Systems and Beyond, AAPG Studies in Geology 64, pp. 273-311.

Nyberg, B., Henstra, G., Gawthorpe, R.L., Ravnas, R., Ahokas, J., (2023). Global scale analysis on the extent of river channel belts. Nature Communications. 14, 2163.

Peng, Y., Hagstrom, C.A., Horner, S.C., Hodgons, C.A., Martin, H.K., Leckie, D.A., Pederson, P.K., Hubbard, S.M., (2022). Low-accommodation foreland basin response to long-term transgression: A record of change from continental-fluvial and marginal-marine to open-marine sequences over 60,000k km^2 in the western Canada foreland basin. Marine and Petroleum Geology. 139, 105583.

Peng, Y., Durkin, P.R., Martin, H.K., Leckie, D.A., Horner, S.C., Hubbard, S.M., (2024). Early Cretaceous evolution of the McMurray Formation: A review toward a better understanding of the paleo-depositional system. Earth-Science Reviews. 252(2024), 104740.

Plint, G.A., (2014). Mud dispersal across a Cretaceous prodelta: Storm-generated, wave-enhanced sediment gravity flows inferred from mudstone microtexture and microfacies. Sedimentology. 61, 609-647.

Rosenshein, J. S., (1988). Hydrogeology of North America, region 18—Alluvial valleys, *In* Back, W., Rosenshein, J. S., and Seaber, P. R., (eds), The geology of North America, Volume 0-2: Boulder, Colorado, Geological Society of America, 165-176.

Sanchez-Roa, C., Bauluz, B., Nieto, F., Abad, I., Jimenez-Millan, J., Faulkner, D., (2018). Micro- and nano-scale study of deformation induced mineral transformations in Mg-phyllosilicate-rich fault gouges from Galera Fault Zone (Betic Cordillera, SE Spain). American Mineralolgist, 103, 1604-1621.

Schieber, J., Southard, J., Kevin, T., (2007). Accretion of mudstone beds from migrating floccule ripples. Science. 318(5857), 1760-1763.

Shan, J., Lin, Z., Chen, L., Zhang, B., Fang, S., Yan, X., Fang, W., Xie, L., Liu, B., Zhang, L., (2018). Reconstruction of meandering paleo-channels using dense well data, Daqing Oil Field, Songliao Basin, China. Petroleum Science. 15, 722-743.

Sylvester, Z., Durkin, P., Covault, J.A., (2019). High curvatures drive river meandering. Geology. 47, 563-566.

Thomas, R.G., Smith, D.G., Wood, J.M., Visser, J., Calverley-Range, E.A., Koster, E.H., (1987). Inclined heterolithic stratification – Terminology, description, interpretation and significance. Sedimentary Geology. 53(1-32), 123-179.

Willis, B.J., Tang, H., (2010). Three-dimensional connectivity of point bar deposits. Journal of Sedimentary Research. 80, 440-454.

Worman, A., Packman, A.I., Marklund, L., Harvey, J.W., Stone, S.H., (2007). Fractal topography and subsurface water flows from fluvial bedforms to the continental shield. Geophysical Research Letters, 34, L07402.

CHAPTER TWO:

INTEGRATION OF BOREHOLE AND OUTCROP DATA FOR PLANFORM RECONSTRUCTION OF AMALGAMATED MEANDER-BELT DEPOSITS, CRETACEOUS MCMURRAY FORMATION AT KEARL MINE, ALBERTA

2.1. Introduction

Meandering river channel evolution exerts a primary control on the distribution of sediment in a meander-belt. In ancient meander-belt deposits, understanding the formative processes can be difficult from limited and sparse data sets. Therefore, integrating multiple data sources to produce channel evolution reconstructions is critical to accurately interpret river dynamics from an ancient meander-belt deposit (Willis, 1989; Ghinassi et al., 2014; Ielpi and Ghinassi, 2014; Durkin et al., 2015; Durkin et al., 2017; Viseras et al., 2018). The results can elucidate and contextualize otherwise enigmatic successions that do not apparently conform to our existing meandering river facies models.

Various data sets have been utilized to produce interpretations concerning channel evolution. For example: 1) observing modern channel-belt evolution through satellite imagery and in-field measurements (e.g., Smith et al., 2009; Sylvester et al., 2020), 2) well-log and core analyses (e.g., Smith et al., 2009; Shan et al., 2018), and 3) three dimensional (3-D) seismic surveys (e.g., Hubbard et al., 2011; Smith et al., 2011; Durkin et al., 2017). Findings from these studies help to refine the deterministic capabilities in geoforecasting and subsurface modelling, particularly within typical point bars, by understanding the evolving characteristics of channel-belts in 3-D. The necessity of such work is apparent in fluvial deposits that are known for drastic facies changes and heterolithic diversity both laterally and vertically. Despite the many challenges of fluvial sedimentology, progress has been made to improve deterministic modelling by understanding channel-belt evolution and their governing morphodynamics (i.e., morphological changes over time).

Architectural elements in meander-belts respond to changes in the depositional system they are a part of. For example, counter-point bars (also sometimes referred to as downstream-migrating point bars (e.g., Ghinassi et al., 2016)), are common when meandering channels respond to lateral confinement caused by cohesive bank material (Page and Nanson, 1982; Smith et al., 2011; Ghinassi et al., 2016; Durkin et al., 2017); and abandoned-channel fills are deposited when upstream channel avulsions or meander bend cut-offs occur (Miall, 1981; Toonen et al., 2012; Bellizia et al., 2021). Furthermore, internal lithofacies distributions within each architectural element are influenced by the morphodynamic evolution of the channel. Fining upward grain-size trends in migrating rivers are due to a decrease in energy from the thalweg to point-bar surface (Allen, 1965; Bridge, 1985), and grain sizes typically decrease downstream from the bend apex of a point bar as shear forces and gravity deter energy around a meander bend (Labrecque et al., 2011; Hagstrom et al., 2019). Both trends are linked to the fundamental relationship between increasing mean grain size with bed shear stress above the depositional surface (Bridge, 1985). However, atypical fluvial trends that oppose these models exist as well. For example, larger volumes of floodplain muds often exist where energy regimes should dictate the deposition of more coarse-grained sediment (Lamb et al., 2020). Atypical sediment deposition presents potential challenges to hydrocarbon recovery planning and execution (Musial et al., 2012; Nardin et al., 2013; Martinius et al., 2017; Clift et al., 2019) and other predictive subsurface fluid flow characterizations for hydrogeological and environmental evaluations (Willis and Tang, 2010; Clift et al., 2019). To help mitigate such challenges, a 3-D model that directly links deposit to subsurface data is needed.

A common strategy to understand complex sedimentology in 3-D is outcrop analysis. Outcrops supply the most intimate and empirical information of the depositional features for

quantitative data input in planform channel-belt reconstruction (e.g., Ielpi and Ghinassi, 2014; Durkin et al., 2015; Viseras et al., 2018; Mayo et al., 2023). Outcrops provide analogues for subsurface deposit interpretations and environmental context for conventional borehole data. They may be utilized to fill the gaps where insufficient information is available or when conventional data resolution is larger than the dimensions of the geobody they are meant to capture. Nonetheless, a lack of direct comparison between outcrop and conventional data exists.

To improve understanding of enigmatic features in meander-belt deposits, this study integrates a dense subsurface data set in the Lower Cretaceous McMurray Formation with vast outcrop availability in the form of mine-face photography at Imperial Oil Ltd.'s Kearl mine, an open-pit heavy bitumen oil sands mine located the Athabasca Oil Sands Region (AOSR) in northeastern Alberta. Freshly exposed mine faces were observed and photographed by site geologists. A planform reconstruction with several fluvial architectural elements highlights atypical fluvial trends that were revealed during excavation. This study aims to provide direct correlation between outcrop and conventional subsurface data, presented in detailed channel-belt reconstructions. These findings can optimize modelling capabilities in analogous deposits in the future and refine point-bar models.

2.2. Background Geology

The McMurray Formation was deposited in the Early Cretaceous (Aptian – Albian) along the northeastern edge of the Western Canadian Sedimentary Basin during long-term-sea-level rise amid smaller scale relative sea-level oscillations (Mossop and Flach, 1983; Ranger and Pemberton, 1992; Hein and Cotterill, 2006; Horner et al., 2019). The Late Triassic Cordillera orogeny of western North America created voluminous accommodation in its retro-arc foreland

basin, enabling fluvial to fluvial-tidal deposits of the McMurray Formation (Leckie and Smith, 1992; Mossop and Shetsen, 1994). Dissolution and collapse of underlying Devonian carbonates and evaporites formed a network of confined drainage pathways that hosted the basal McMurray Formation deposits (Flach and Mossop, 1985; McPhee and Wightman, 1991; Broughton, 2015; Barton et al., 2016), and, once the negative topography was infilled, unconfined meander-belt deposition continued (Flach and Mossop, 1985; Crerar and Arnott, 2007). The stratigraphy of the McMurray Formation therefore comprises relatively thinner, segmented and geologically complex stacks of channel, floodplain and lacustrine deposits near the base (Carrigy, 1959; Barton et al., 2016), and thicker continental-scale channel-belt sedimentation in the deposits above (Carrigy, 1959; Hein and Cotterill, 2006; Benyon et al., 2014; Blum and Pecha, 2014). The deposition of the McMurray Formation was subsequently terminated after inundation of the southward prograding Boreal Sea, resulting in muddy and glauconitic marine sediments of the Wabiskaw Member of the Clearwater Formation (Hein and Cotterill, 2006; Ahmad and Gingras, 2022).

The McMurray Formation is informally sub-divided into three units based on work from Carrigy (1959): the lower, middle and upper McMurray units (Fig. 2.1); however, this tripartite system has since been improved for chronostratigraphic accuracy (Hein and Cotterill, 2006) and continues to be improved incrementally with ongoing study (e.g., Chateau et al., 2019; Horner et al., 2019; Hardekopf et al., 2022; Hagstrom et al., 2023; Peng et al., 2024). Nonetheless, the informal system is still used for its simplicity in lithologic and environmental delineation. The lower McMurray unit comprises fluvial sandstone intervals, often thinner and less laterally extensive than middle McMurray units, bounded by finer-grained lacustrine and floodplain deposits. Fluvial packages here range from up to 30-meters thick to localized sandstone lenses

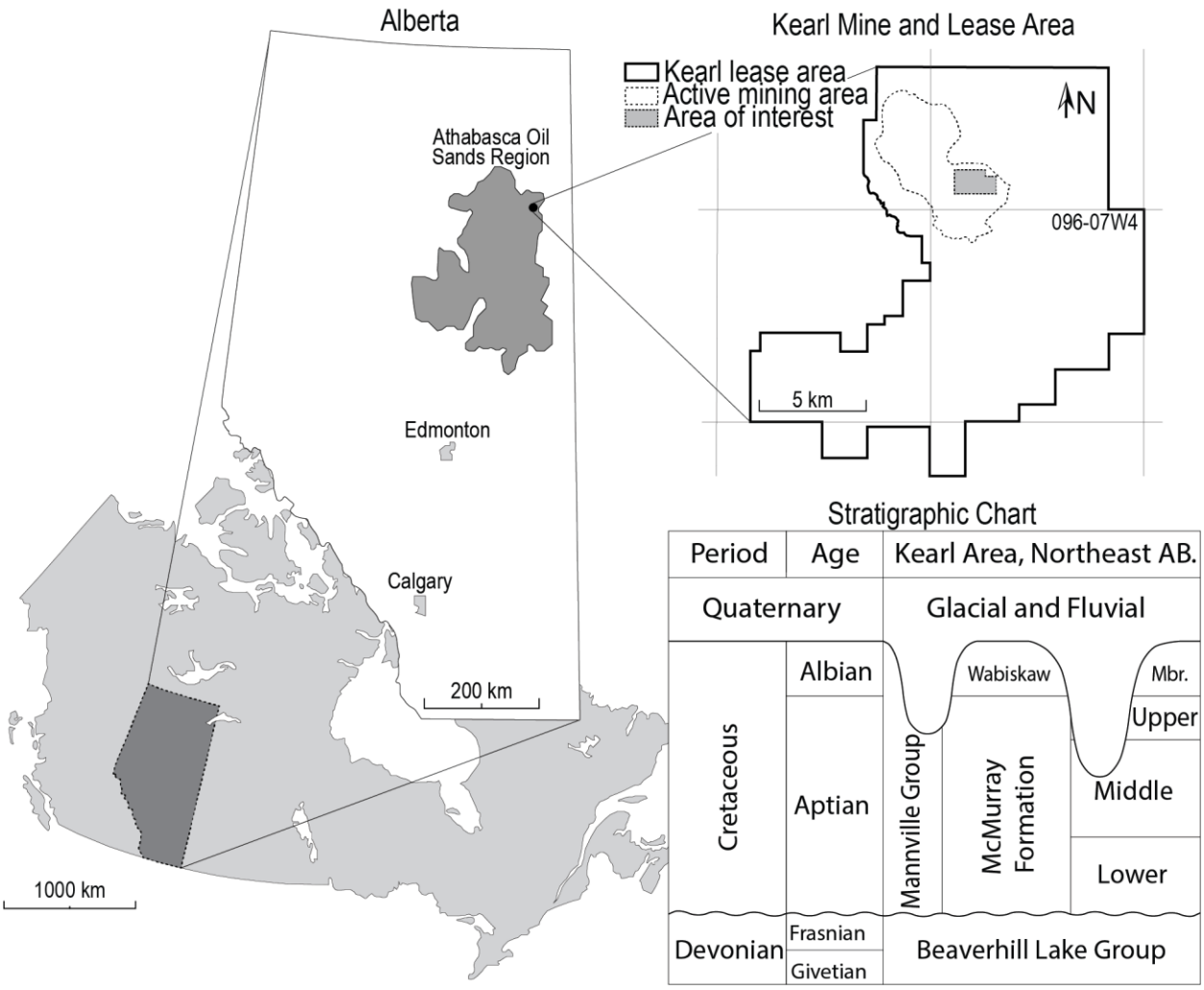

Figure 2. 1 The location of Kearl mine and the area of interest for the current study and a stratigraphic chart for the Mannville Group (McMurray Formation and Wabiskaw Member) and bounding units that are present in Kearl mine.

less than 5-meters thick, bounded by terrestrial floodplain mudstones. The overlying middle McMurray unit comprises thick (up to 45 m) channel-belt deposits with point bars, counter-point bars and abandoned-channel fills that were the result of a continental-scale drainage basin comparable to the modern Mississippi River (Benyon et al., 2014). The upper McMurray unit comprises regionally correlatable, coarsening upward parasequence sets (PSS) coinciding with

prograding paleo-shorelines (Hein et al., 2006; Baniak and Kingsmith, 2018; Chateau et al., 2019).

The revised stratigraphy of Hein and Cotterill (2006) is divided by the PSS and the valley fills that subtend from them. The PSS are named from oldest to youngest, as C, B1, B2, A1, and A2 PSS. The associated valley cut-and-fill deposits are named C-, B1-, B2-, A1- and A2-channel-belts. C-channel-belt deposits are generally thick fluvial intervals of the lower McMurray Formation, while the remainder of the overlying channel fills, from B1 to A2, belong to the middle McMurray. The middle McMurray comprises both single- or multi-storied meander-belts, where the stacked deposits are observed as two or more fining-upward intervals. Finally, each channel-belt interval transitions upwards into regional parasequence sets that represent shoreline progradation in the upper McMurray units deposited during cyclic marine inundation.

2.3. Study Area

Kearl mine is located approximately 75 km NNE of Fort McMurray, Alberta, Canada, in Townships 95 to 97 and Ranges 7 and 8, 4th meridian west (Fig. 2.1). The 1.9 x 1.1 km area of interest within Kearl mine was excavated during data collection, providing opportunity to continuously observe sequential outcrop exposures of the McMurray Formation. The study location was chosen because of the ease of accessibility, optimizing the parameters for data acquisition and mine safety, and for the presence of heterolithic deposits that caused geomodelling issues during excavation (i.e., atypical deposits). The southern and western borders of the study area were chosen based on the difficulty of interpreting the increasingly complex stratigraphy to the south, and the lack of historic mine-face photographs for relevant geologic information. The northern and eastern borders were selected based on mining strategy at the time

of the study, where excavation reached the planned limits due to local geology and existing mining infrastructure. The targeted stratigraphic interval in the area of interest is the basal channel-belts of the middle McMurray unit, averaging approximately 15- to 20-m thick.

The stratigraphy in Kearl mine contains basal McMurray Formation valley fills (i.e., lower McMurray; Carrigy, 1959) with pervasive floodplain fines overlain by at least two amalgamated channel-belt deposits (i.e., middle McMurray; Carrigy, 1959; Fig. 2.2A). The uppermost channel-belt is often incomplete, top-truncated by marine deposits in the Wabiskaw Member or Pleistocene glacial till. Top truncation accounts for the difficulty in identifying the correct channel-belt nomenclature derived by Hein and Cotterill (2006). Therefore, this study uses adjusted nomenclature based on the chronostratigraphic framework (Hein and Cotterill, 2006; Fig. 2.2A). The stratigraphy at Kearl mine comprises McMurray 1 PSS (M1PSS), McMurray 2 PSS (M2PSS) and McMurray 3 PSS (M3PSS), each with subtending channel-belt fills entitled McMurray 1 (M1), McMurray 2 (M2), and McMurray 3 (M3), respectively (Fig. 2.2A). It is likely that the Kearl area comprises basal C-channel incision-and-fill in the M1, overlain by two or more subsequent B- and/ or A-channel deposits in the M2 and M3, each subtending from regionally deposited parasequence sets (Fig. 2.2A).

In Kearl mine the M1 interval ranges from over 40-meters-thick to locally absent and comprises an amalgam of fluvial sandstone lenses within a thick succession of floodplain or lacustrine mudstone. The M2 deposits contain upward-fining sediments that indicate deposition from a relatively smaller-scale channel-belt system compared to the overlying M3. The M2 is up to 25-meters-thick and averages 15 – 20 m of one or more fining-upward sequences. It is unclear whether stacked upward fining intervals in M2 are separated by events caused by sea-level fluctuations and, therefore, subtending from different PSS; by local channel-belt avulsions and

subsequent re-occupations; or by the same channel-belt with a vertical aggradational component. Without significant evidence of stratigraphic demarcation for the medial fining-upward interval in M2, it is named McMurray 2.5 (M2.5) and includes the possibility of an additional PSS (M2.5PPS; Fig. 2.2A). The M3 interval is up to 45-meter-thick, comprising upward-fining channel-belt deposits that are comparable to A2 channel descriptions in stratigraphic framework studies nearby (e.g., Chateau et al., 2019; Horner et al., 2019; Hardekopf et al., 2022; Hagstrom et al., 2023), and are located north of A2 deposits comprising paleoflow data directed towards the present study area (Durkin et al., 2020a).

The interval of interest for this study comprises the M2 and M2.5 channel-belt packages. Mining strategies targeted the base of M2 across the majority of the mine, which greatly benefited this research. The specific area of interest contains two laterally juxtaposed groups of point-bar, counter-point-bar, and abandoned channel-fill deposits, distinguishable by well-log character and outcrop. These included M2 deposits that comprised north-migrating bedforms, and the subsequently deposited M2.5 comprising south-migrating bedforms. Minimal post-depositional deformation is present in much of the study area and interval of interest, evidenced by low differential relief in the base M2 surface with a standard deviation of less than 2.5 meters throughout (calculated from the base M2 elevation in each well in the study area; n = 140; Fig. 2.2B). The southwest of the study area is an exception, where the base of the M2 undulates and rises significantly to the southwest corner (Fig. 2.2B).

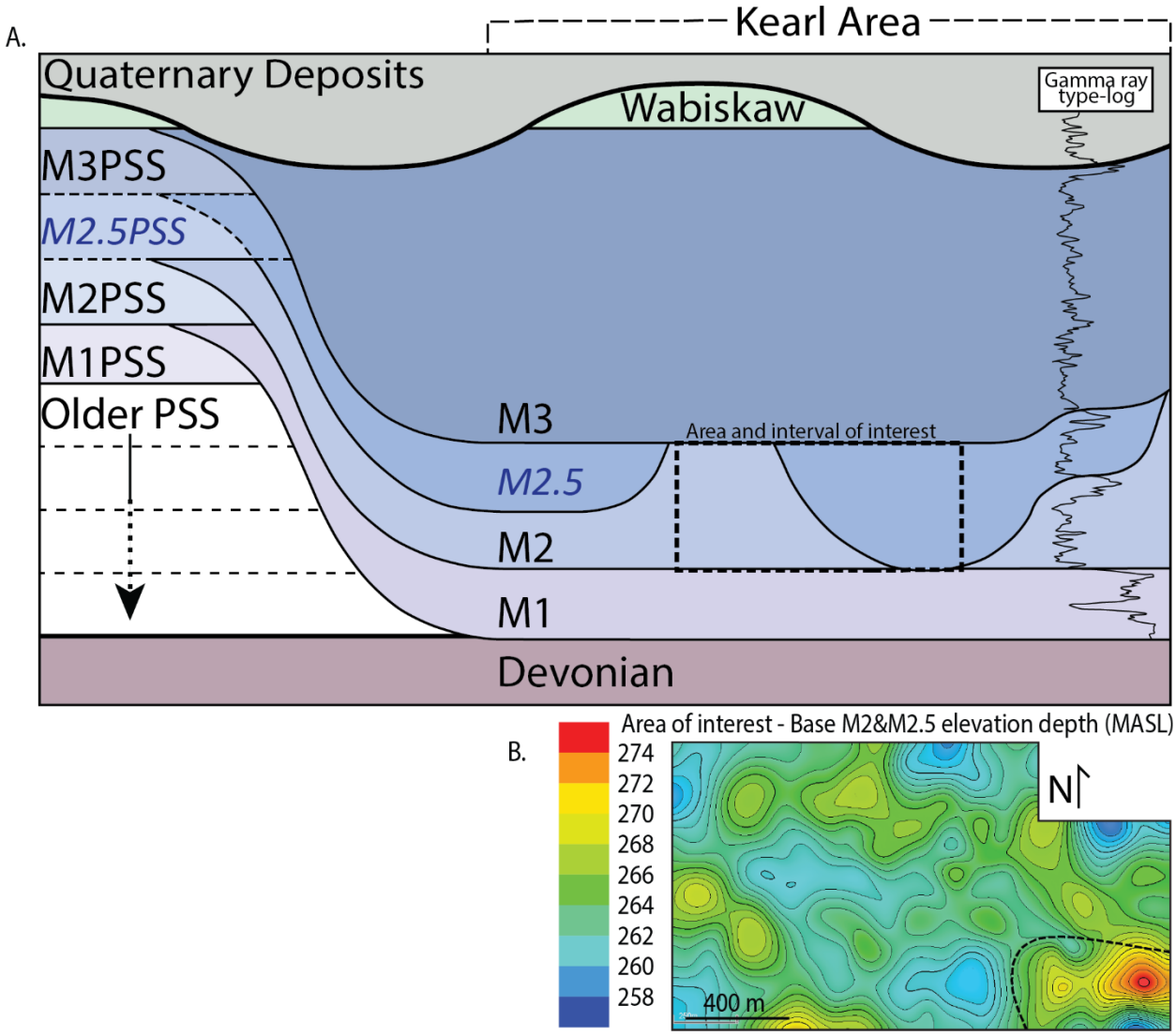

Figure 2. 2 (A) A schematic stratigraphic cross section/ model of the McMurray Formation and bounding units in Kearl mine. The McMurray Formation comprises Older PSS to M3PSS and the M1 to M3 channel-belts. It is unclear if the M2.5PSS is present. M2.5 is observed as a separate meander-belt from M2 in Kearl. The area of interest is commonly excavated to top of M1. The gamma-ray type-log was taken from a well-log in the study area (Type-log location shown in Fig. 2.3) and displays a floodplain (M1) overlain by two relatively smaller channel-belts (M2 and M2.5) and a larger channel-belt (M3). (B) A topographic map of the contact between M1 and M2/ M2.5 in the area of interest. The black dotted line in the southeast corner represents an area of anomalously high positive relief on the M2.5 base.

2.4. Data Set and Methods

The study area comprises 140 wells accompanied by well-logs and core photographs that were used to derive a lithofacies scheme and delineate facies associations, architectural elements and stratigraphic boundaries (Fig. 2.3). LiDAR surveys, drone post-processing kinematics surveys and mine-equipment GPS data were utilized for mapping and photograph locations. Gamma-ray and dip-meter well-logs were used in tandem to derive spatiotemporal paleo-channel evolution. Paleoflow and bar migration directions are determined from dipmeter well logs and displayed as scroll patterns that represent sequential evolution of channel meandering over time. IHS bedding plane dip directions were used to determine accretion directions. Paleoflow was derived from foreset dip directions of trough-cross-bedded sandstones, primarily located near or at the base of channel-belt deposits. The perpendicular relationship between paleoflow and lateral accretion directions provided further confidence in paleo-environmental interpretations and orientation of bar scroll patterns. Boreholes with flat-lying, mudstone-dominant deposits were recorded to show interpreted abandoned channel locations.

On a daily basis, dozens of photographs of vertical mine-face exposures were taken by site geologists from May 2022 to August 2023. Photographs were taken based on relevance to production (i.e., modelling concerns, ore and waste headings, requests from mine planning staff, etc.), for daily documentation of excavated material, and for geologic information in the present study. Specific areas of interest were re-visited when mining equipment was clear for further observation using binoculars and higher resolution photographs. Photograph locations were obtained using weekly LiDAR surveys and real-time GPS coordinates in mining equipment (Fig. 2.3). Photograph scales were derived by LiDAR and the teeth markings left on mine faces from excavation equipment shovel buckets that scrape the deposits during excavation.

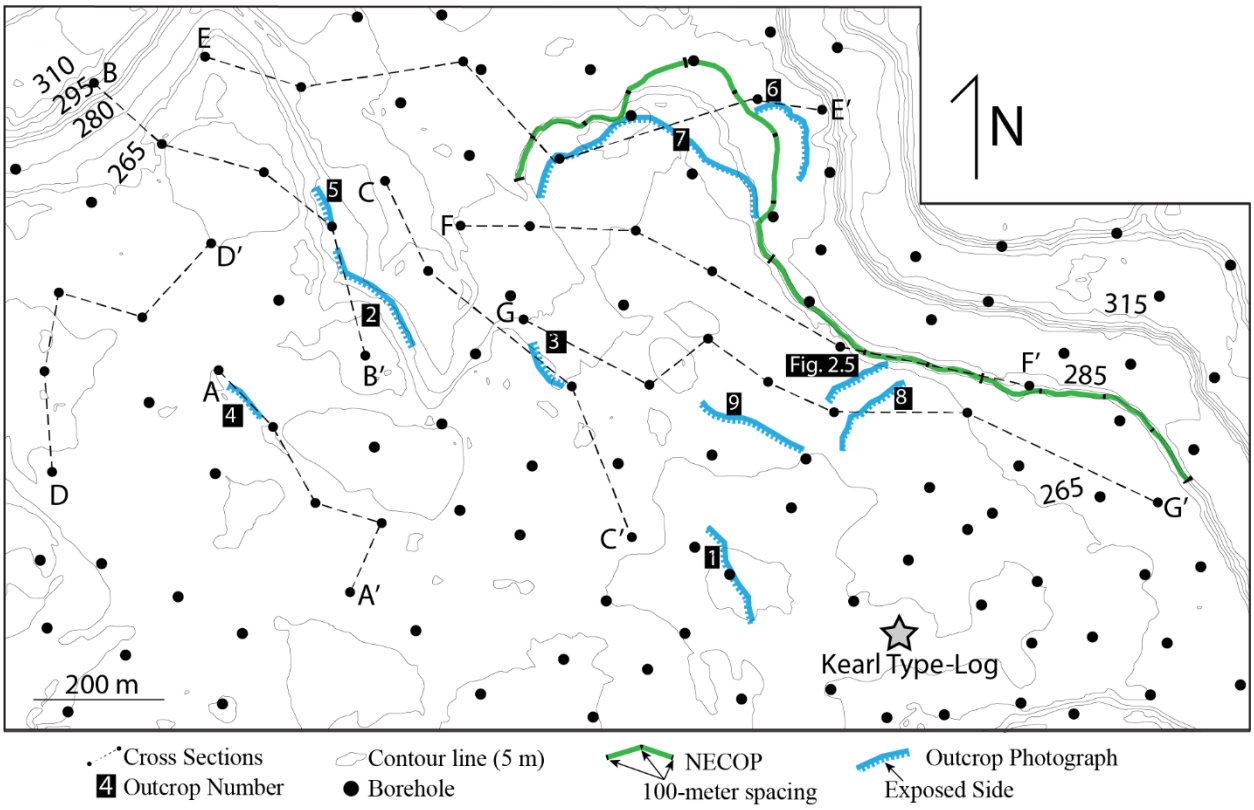

Figure 2. 3 A topographic map of the study area in Kearl mine. Topography was recorded with LiDAR scanning surveys April 2023. Elevation is recorded in meters above sea level (MASL). Kearl type-log (star) is displayed in Figure 2.2A. Outcrop locations are displayed with blue and green lines. Outcrop for FA5 is shown in Figure 2.5; outcrops 1 – 5 are shown in Figure 2.8; outcrop 6 is shown in Figure 2.11; outcrop 7 is shown in Figure 2.12; outcrop 8 is shown in Figure 2.14; outcrop 9 is shown in Figure 2.16; NECOP is displayed in Figure 2.10; cross sections A-A', B-B', C-C' and D-D' are displayed in Figure 2.7; cross sections E-E', F-F' and G-G' are displayed in Figure 2.9.

Mine-face photographs for M2 deposits were gathered from historic mining photograph documentation from January 2016 – May 2022, before the conception of this study. These photographs were collected to document *in-situ* and placed sediment ore quality, and not always beneficial for this research. M2 outcrops are presented as five panoramic and stitched photographs chosen from a library of thousands of photographs (Fig. 2.3). Photographs for M2.5 were taken by the author and site geologists with sedimentological research purposes in mind from May 2022 – August 2023. These photographs are presented as a single 1.6 km-long

panoramic exposure of an *in-situ*, laterally continuous mine face in a single M2.5 point-bar deposit, averaging 17-meters thick, called the northeastern combined outcrop photographs (NECOP); and six smaller-scale photographs and panoramic photographs of various lengths (Fig. 2.3). NECOP and several smaller-scale panoramic photographs were stitched together using an image editing software.

Outcrop observations were used to investigate lithofacies distributions and their lateral extent. The continuity of point-bar and counter-point-bar IHS observed in outcrop increased confidence in demarcating channel-belt architectural elements. Precise locations of disconformal boundaries were documented for environmental context including abandoned-channel fill locations, intra-point-bar erosional surfaces and stratigraphic boundaries. The majority of on-site investigations were made from within a work truck at least 30-meters away from the mine-faces to adhere to mine safety standards.

2.5. Results and Analysis

Borehole data and outcrop observations were utilized for a comprehensive reconstruction of the channel-belt in M2 and M2.5 in the area of interest. The IHS generally displays congruent bedding planes with gently sloped dips between 3 - 15° towards the time-equivalent channel thalweg. Bar scroll patterns and channel evolution are derived based on the assumption that bar surfaces dip perpendicularly to the length of the associated channel upon deposition. Dip directions often diverge in planform, representing the arcuate shape of point bars and the lateral accretion direction during channel migration. When preserved, IHS deposits directly downstream of point bars often decrease in grain size and dip directions may begin to converge in planform. These characteristics represent counter-point-bar deposits or concave bank-bench deposits

(Taylor et al., 1971; Page and Nanson, 1982; Smith et al., 2009), where lateral bar migration is inhibited and down-stream translation of the point bar becomes the primary mobilization method (Smith et al., 2009; Ghinassi et al., 2016). Abandoned-channel fills are characterized by mudstone-rich sediments that displayed flat-lying or bottom-channel-conforming dips.

2.5.1. Facies Analysis

Seven lithofacies (F0 to F6) are identified in this study (Table 1). Sedimentary structure, grain size and percent-fines (grain-sizes less than 44 μm are herein termed mud) from well-logs and core photograph observations were used for lithofacies classification. The results are broadly consistent with previous facies studies of channel-belt deposits in the McMurray Formation, and for further information we refer to these facies studies (Hein and Cotterill, 2006; Crerar and Arnott, 2007; Musial et al., 2012; Horner et al., 2019; Tang et al., 2019). Based on the proportion of interpreted lithofacies, facies associations 1 – 5 are used to characterize each well (FA1 – FA5; Table 1).

Facies Association 1 – Sandstone-dominated upward fining IHS

Description

Facies association 1 (Fig. 2.4A; Table 1) is dominated by medium- to coarse-grained sandstone (F1) with trough cross-bedding, variable mudstone-clast distributions (F0b, F0c) and local coal and wood debris near the base to middle portion of the interval, approximately 5 - 10 m thick on average. Outcrop and core of the lower intervals of M2 and M2.5 show trough cross-bedded sandstone with high-angle bedding planes that are represented by poorly organized dip-meter responses between 0 - 40º. There is an upwards transition to very fine- to fine-grained sandstone (F2) with some sandstone-dominated IHS (F3) and rare intervals of proportionate parts

Table 2. 1 Facies and facies associations

Facies		Lithology	Sedimentology	Interpretation	Facies Association Occurrence				
					FA1	FA2	FA3	FA4	FA5
F0	a	Mudstone clast breccia; 10 - 35% clasts	Trough cross-bedded, fine- to medium-grained sandstone matrix. Angular to sub-rounded, moderately well sorted mudstone clasts from < sand- to pebble-sized. Clasts sometimes line trough cross bedding planes. Absent bioturbation.	Moderate to high energy occurring in lower bar from cutbank mud erosion or as intermittent upper bar IHS clast rip up and redeposition.	Common	Common	Rare	Rare	Common
F0	b	Mudstone clast breccia; 35 - 65% clasts	Trough cross-bedded, fine- to coarse-grained sandstone matrix. Angular to sub-rounded, poorly sorted mudstone clasts from < sand- to cobble-sized. Clasts have graded bedding and line trough cross bedding planes. Absent bioturbation.	Moderate to very high energy occurring in lower bar from cutbank mud erosion and redeposition or as intermittent upper bar IHS clast rip up and redeposition.	Moderate	Moderate	Rare	Rare	Common
F0	c	Mudstone clast breccia; 65 - 90% clasts	Trough cross-bedded, fine- to very coarse-grained sandstone matrix. Angular to sub-rounded, very poorly sorted mudstone clasts from < sand- to boulder-sized. Clasts have graded bedding and line trough cross bedding planes and scour surfaces. Absent bioturbation.	High to very high energy occurring in lower bar from cutbank mud erosion and redeposition or as intermittent upper bar IHS bedding breakup and clast rip up and redeposition.	Rare	Rare	Rare	Rare	Common
F1		Sandstone	Trough cross-bedded, medium- to very coarse-grained sandstone. Rare mudstone layers, laminae and clasts. Local coal and woody debris. Uncommon bioturbation.	Moderate to very high energy channel bottom and lower bar dunes. Some intermittent upper bar scour and fill.	Common	Moderate	Moderate	Rare	Common
F2		Sandstone	Trough cross-bedded, very fine- to fine-grained sandstone. Rare mudstone layers, laminae and clasts. Uncommon bioturbation.	Moderate energy channel bottom and lower bar, downstream migrating dunes. Some intermittent upper bar dune deposition.	Common	Common	Moderate	Moderate	Moderate
F3		Sandstone w/ mudstone interbeds	Trough cross bedded to rippled, fine- to medium-grained sandstone beds w/ dm- to m-scale bed thickness. Laminated to massive mudstone, < 1 cm - cm's thick. Sandstone is dominant. Inclined beds 5 - 15°. Moderate to absent *Planolites* and *Cylindrichnus* burrowing.	Cyclic high to low energy fluctuations resulting in laterally accreting interbeds. Common on lower to middle bar. Rare on upper bar.	Moderate	Common	Common	Moderate	Common
F4		Sandstone-mudstone interbeds	Trough cross bedded to rippled, fine- to medium-grained sandstone beds w/ cm- to dm-scale bed thickness. Laminated to massive mudstone, < 1 cm - cm's thick. Sandstone sub-equal to mudstone. Inclined beds 5 - 15°. Common to absent *Planolites* and *Cylindrichnus* burrowing.	Cyclic medium to low energy fluctuations, laterally accreting interbeds. Common throughout bar interval.	Rare	Common	Common	Common	Common
F5		Mudstone w/ sandstone interbeds	Rippled, very fine- to fine-grained sandstone beds w/ cm-scale bed thickness. Laminated to massive mudstone, < 1 cm - dm's thick. Mudstone is dominant. Inclined beds 5 - 15°. Abundant to uncommon *Planolites* and *Cylindrichnus* burrowing.	Cyclic medium to very low energy fluctuations, laterally accreting interbeds. Common on upper bar, moderate on middle bar, rare on lower bar intervals.	Rare	Moderate	Common	Common	Moderate
F6		Mudstone	Laminated to massive with some wavy-bedded mudstone. Carbonaceous mudstone intervals present (dark grey). Some sandstone/ siltstone interbeds. Abundant to uncommon *Planolites*, *Cylindrichnus* and *Gyrolithes* burrowing.	Low to absent energy, vertical aggradation. Rare periods of elevated energy. Intense bioturbation in shallow stagnant conditions, absent bioturbation in deep water.	Rare	Rare	Rare	Common	Rare

sandstone and mudstone IHS (F4) with organized and less than 15º dip-meter character. IHS deposits (F3, F4) are often located 10 – 20 m above the base of M2 and M2.5 and continue until M3 truncation. IHS is locally top truncated lower in the interval by sandstone, mudstone clast breccia (F0) or IHS bedding with bedding plane re-orientation. Erosional surfaces are planar and shallowly dipping (< 15º) or locally shaped as upward concave boundaries up to 60-meters in length.

Interpretation

The dominance of coarse-grained lithofacies (F1 – F3) in facies association 1 represents high energy deposits relative to the other facies associations. High angle bedding planes within trough cross-bedded sandstone indicate foresets of migrating channel-bottom dunes (Brekke et al., 2017; Hagstrom et al., 2019). Intervals upwards of 10-meters from the base of M2 and M2.5 containing sand-dominated IHS indicate deposition on the mid- to upper-point bar in fluctuating and lower energy, shallower water depths relative to the channel thalweg (Bridge, 1995). Rhythmic sandstone and mudstone interbeds with consistent bedding thicknesses suggest semi-stable periods of energy flux, perhaps representing seasonal variations in precipitation and episodic periods of deposition and erosion (Bridge et al., 1995; Jablonski and Dalrymple, 2016). IHS bedding plane re-orientations suggest periods of significant point-bar erosion, or intra-point-bar erosion; a process that often involves migration, expansion or rotation and overall bar reorientation during flooding events and modifying the shape or mean lateral accretion direction of the point-bar deposits (Durkin et al., 2015; Martinius et al., 2017; Hagstrom et al., 2019). The accompanied mudstone clasts are interpreted to be from re-working IHS on the point-bar surface or eroded mudstone-rich material in the cutbank (Leopold and Wolman, 1960; Labrecque et al., 2011; Chen et al., 2022). Coal and woody debris are often associated with higher energies in F1

and represent the inundation and erosion of channel adjacent woodland growth (Chen et al., 2022). The overall sandstone-dominance observed in both well data and outcrop represent a relatively high energy deposition that is commonly observed in the upstream point bar location near the meander bend apex (Labrecque et al., 2011; Hagstrom et al., 2019; Bellizia et al., 2021).

Facies Association 2 – Mudstone-dominated upward fining IHS

Description

Facies Association 2 (Fig. 2.4B; Table 1) comprises very fine- to fine-grained trough cross-bedded sandstone (F2) with some IHS (F3) or mudstone clasts (F0a, F0b) in the basal 10-meters of the M2 and M2.5 intervals. Thin units of coarser-grained sandstone (F1) and mudstone clast breccia (F0) may be present. Horizontal to shallowly dipping (< 8º) bedding plane boundaries in F1 and F2 are locally lined with mudstone laminae. FA2 transitions upwards to equal proportions of mudstone and sandstone IHS (F4), to mudstone-dominated IHS (F5). IHS deposits contain local erosional boundaries with mudstone clast breccia and apparent IHS bedding re-orientation. IHS packages are vertically continuous for up to 15-meters. Dip-meter character is similar to FA1, comprising unorganized trends in dip directions for F1 and F2 and increasing overall organization in bedding orientation in mudstone-rich IHS deposits (F3 – F5).

Interpretation

Facies association 2 contains elevated mudstone content on average relative to FA1, indicating a depositional setting with less overall energy conditions. Upward fining IHS indicates point-bar deposition and lateral bar accretion (Allen, 1965). The mudstone laminae within trough cross-bedded sandstone (F1, F2) bedding plane boundaries represent dune bottomset and lower foreset mudstone preservation in dune troughs (Ferens and Durkin, 2020; Bzdziuck, 2023).

Dune trough mudstones deposits are potentially caused by flow separation across the dune apex, causing subsequent mudstone deposition and preservation that is restricted within dune trough (Becker et al., 2013; Ferens and Durkin, 2020). IHS bedding re-orientation represents point bar geometry re-working during elevated energy events (Hagstrom et al., 2018). FA2 is interpreted to represent downstream point-bar deposits located further from the bend apex than FA1, where flow energy decreases and results in elevated proportions of fine-grained sediment (Ferguson et al., 2003; Labrecque et al., 2011; Hagstrom et al., 2019).

Facies Association 3 – Mudstone-dominated IHS

Description

Facies association 3 (Fig. 2.4C; Table 1) comprises mudstone-dominated IHS (F5) with lesser proportions of sandstone-rich intervals (F3, F4). Unlike FA1 and FA2, deposits in FA3 do not typically fine upwards. Instead, deposits remain mudstone-rich throughout the majority of the interval, comprising up to 20-meters of vertically continuous IHS (F4, F5). Thin intervals (< 3 m) of sandstone deposits (F1, F2) are present locally at the base of FA3. Mudstone proportions above 90% (F6) are sometimes present in FA3. Dip-meter character is commonly shallow (< 15º) and organized throughout, with some thin intervals of elevated dip angles (> 20°). FA3 wells are adjacent to FA2 wells and are differentiated from them by a lack of upward fining trends and IHS bedding dip directions that converge in planform.

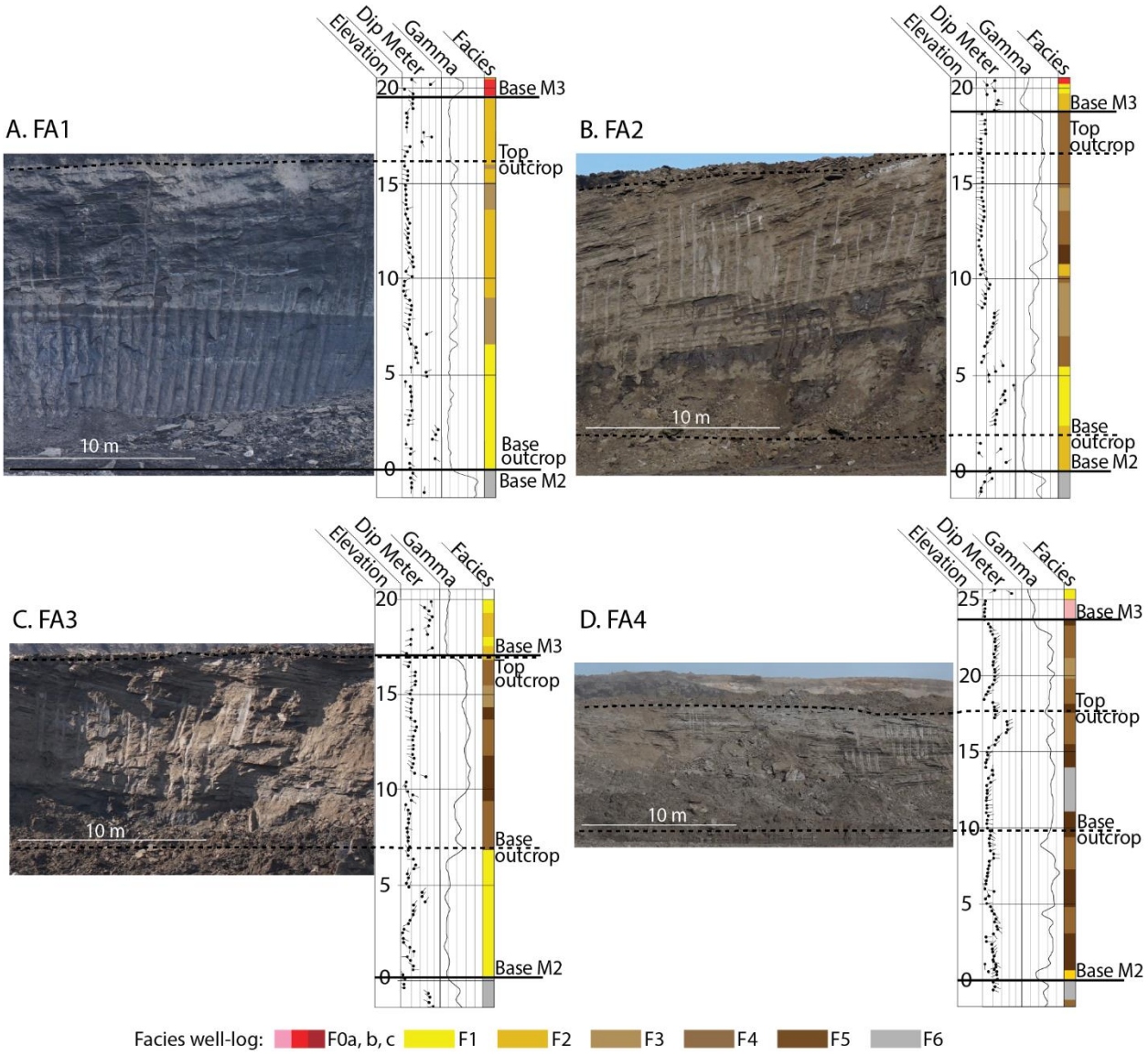

Figure 2. 4 Outcrop and well-log examples of facies associations 1 – 4. Outcrop scale is derived by shovel teeth markings. Elevation well-log scales are equivalent to outcrop scale. Outcrop base and top are traced by dotted black lines. Well-logs are taken from boreholes nearest to the outcrop locations. Well-log tracks, from left to right, are elevation in meters above base M2; dip-meter on a scale of 0 - 50°; gamma-ray on a scale of 0 – 150 API; lithofacies distributions are based on Table 1 lithofacies. (A) Facies association 1 – Sandstone-dominated upward fining IHS. (B) Facies association 2 – Mudstone-dominated upward fining IHS. (C) Facies association 3 – Mudstone dominated IHS. (D) Facies association 4 – Mudstone with sandstone interbeds.

Interpretation

The mudstone-rich and shallowly inclined interbedding in FA3 is indicative of lateral accretion in low energy conditions similar to FA2. Unlike point-bar deposits in FA1 and FA2, these deposits do not fine upwards, representing consistently lower energy with minor fluctuations for most or all of the interval (Ghinassi et al., 2016). Planform convergence of IHS bedding dip directions indicate downstream bar translation and the preserving of concave bank deposition (Page and Nanson, 1982) that is consistent with descriptions of counter-point-bar deposits (Ghinassi and Ielpi, 2015; Durkin et al., 2018). These deposits tend to form when flow energy is deflected downstream of the bend apex, often due to erosion-resistant material in the cutbank (Page and Nanson, 1982; Ghinassi et al., 2016). This hydrodynamic change leads to flow-separation and produces reverse-eddy currents that are directed upstream (Taylor et al., 1971; Ghinassi et al., 2016) where the decreased energy enables fine-grained deposition along the outer concave channel bank immediately downstream from a point bar (Durkin et al., 2017).

Facies Association 4 – Mudstone with sandstone interbeds

Description

Facies association 4 (Fig. 2.4D; Table 1) comprises mudstone-rich interbedded deposits (F4, F5) with flat to very-low-angle bedding (< 5º) that is not always consistent in dip direction. Mudstone content may be above 90% (F6) in some intervals. FA4 deposits can contain a sand-rich base (F1 – F2) that sharply transitions to mudstone-rich deposits above. Outcrop exposure preserves a concave up base delineating mudstone-rich deposits from coarser material below. In planview FA4 is often located adjacent and downdip of IHS in FA1, FA2 and FA3 deposits, and occur in a linear channel-form that partially encases FA1 and FA2 IHS deposits.

Interpretation

The relatively horizontal bedding of mudstone-dominated deposits (F5, F6) in FA4 indicate vertical aggradation in quiescent, channel bottom depositional conditions (Miall, 1981; Willis and Tang, 2010; Hubbard et al., 2011; Toonen et al., 2012). Sandstone interbeds suggest intermittent pulses of energy, perhaps during seasonally wet conditions (Willis and Tang, 2010). The presence of a concave-upward shape in mudstone bedding likely indicates deposition in a channel-form container, and suggests that no further channel migration took place due to upstream flow cut-off (Willis and Tang, 2010; Toonen et al., 2012).These characteristics are consistent with abandoned-channel conditions (Toonen et al., 2012; Bellizia et al., 2021). Channel abandonment occurs when the meander bend is cut-off, leaving a channel-form container outside of the active channel and below the surrounding floodplain. Meander cut-off can occur by neck cut-off, chute cut-off or channel avulsion (Allen, 1965b). Neck and chute cut-off abandoned-channel fills are often mudstone-dominated similar to FA4 deposits (Allen, 1965b; Bellizia et al., 2021).

Facies Association 5 – Unorganized heterolithic stratification and mudstone clast breccia

Description

Facies association 5 (Fig. 2.5; Table 1) contains various sedimentary features observed in each of the previous facies associations. The basal 5 – 10 m comprises coarse-grained sandstone (F1) commonly disseminated with mudstone clasts of various sizes and concentrations (F0a – F0c). The overlying middle and upper intervals contain varying proportions of sandstone, mudstone and mudstone clast breccia interbeds. The sandstone layers are fine- to coarse-grained (F1, F2) with mudstone layers and laminae lining sandstone bedding plane boundaries. The

mudstone beds range from mm's to dm's thick and are inclined and planar or have wavy bedforms that are laterally discontinuous. Mudstone clast breccia is common at the base of sandstone-rich bedsets. Mudstone clasts are sand- to boulder-sized, elongate and angular to sub-angular. In core mudstone clasts appear to be randomly oriented and without sorting, however, outcrop exposures show mudstone clasts lining trough cross-bedding structures. Local horizontally bedded mudstone up to dm's thick often contain sharp lateral mudstone termination. In well-log the gamma profile varies from saw-tooth, upward-fining, or upward-coarsening with no consistent trend throughout; and the dip-meter logs often display randomly oriented dip direction and inclination. Some wells display short intervals (< 5 m) of organized and shallow dips of apparent IHS bedding but dip-meter trends are dissimilar between adjacent wells. FA5 are grouped together in a localized portion of the study area, representing eight total wells.

Interpretation

The presence of coarse-grained sandstone, mudstone bedding truncation and pervasive mudstone clasts throughout FA5 indicates high energy conditions. The common presence of mudstone bedding in the upper intervals would indicate regular energy fluctuations, however, the lateral and vertical discontinuity of mudstone-rich facies and dominance of trough cross-bedding structures indicates elevated energy regimes in the middle to upper portions of the point bar as well. Although borehole interpretations would suggest the presence of continuous intervals of mudstone-rich IHS, outcrop observations show that large (gravel-sized), horizontally oriented mudstone clasts and mudstone-lined foresets and bottomsets in trough cross-bedded sandstone may have been mistaken for lower and fluctuating energy IHS facies like F4 and F5. Based on outcrop evaluations FA5 deposits are likely located near the bend apex of the point bar where energy is elevated. A more detailed analysis of FA5 is discussed later.

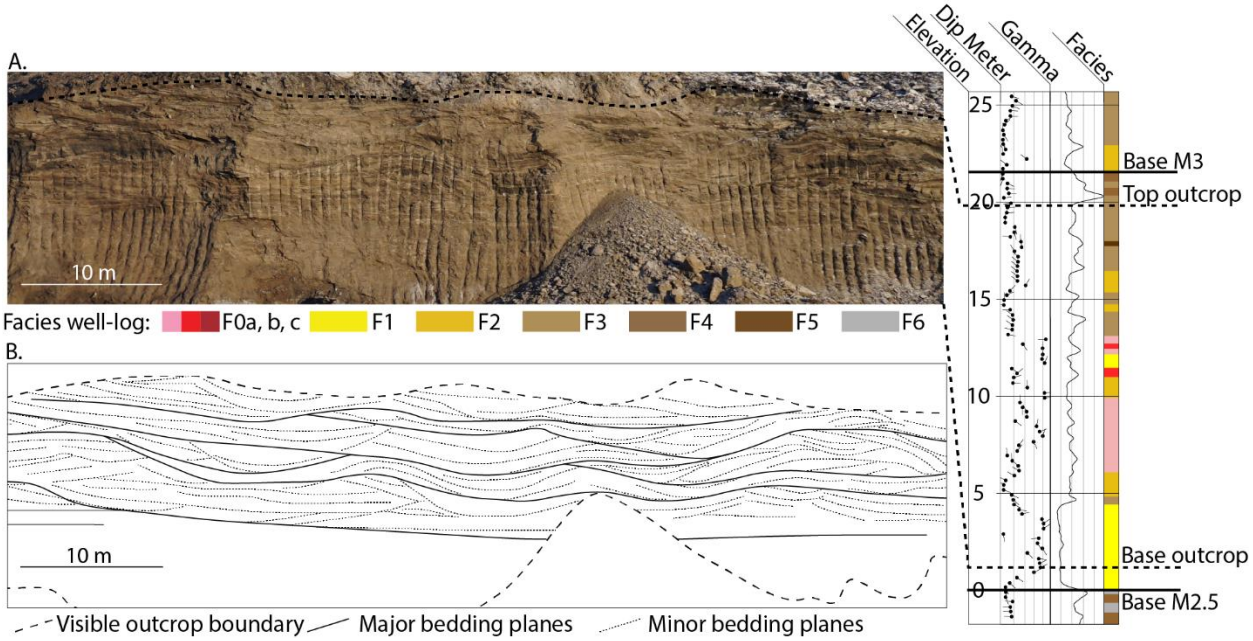

Figure 2. 5 Facies association 5. (A) Outcrop and well-log of facies association 5 – Unorganized heterolithic stratification and mudstone clast breccia. Outcrop scale is derived by shovel teeth markings. Outcrop location is displayed in Figures 2.3 and 2.6B. Elevation well-log is not equivalent to outcrop scale. Outcrop base and top are traced by dotted black line. Outcrop location is marked in Figure 2.3A and Figure 2.6A. Well-log is taken from borehole near outcrop location. Well-log tracks, from left to right, are elevation in meters above base M2.5; dip-meter on a scale of 0 - 50°; gamma-ray on a scale of 0 – 150 API; lithofacies distributions based on Table 1 lithofacies. The white rectangle represents the traced bedding displayed in 2.5B. (B) Traced bedding showing major and minor depositional planes and erosional surfaces. Note the peculiar trough-shaped bedding consistently lined with mudstone.

2.5.2. Channel-belt Reconstruction

The following section combines facies association distributions, paleoflow and bar migration direction interpretations, with maps and outcrop to build a planform reconstruction of the paleoenvironment and describe the spatiotemporal evolution of the channel-belt(s). The area of interest is divided into nine architectural elements (AE) based on facies associations distributions, macroform migration trends, and the dominant depositional processes (AEI –

AEIX; Table 2.2; Fig. 2.6A). The elements include four point bars (AEI, AEIV, AEVI, AEVIII), three counter-point bars (AEII, AEV, AEVII) and two abandoned-channel fills (AEIII, AEIX).

Point Bars

AEI, AEIV, AEVI and AEVIII contain upward-fining IHS deposits (FA1, FA2) and diverging IHS bedding dip directions in planform (Table 2.2; Fig. 2.6A). Paleoflow measurements are often perpendicular to IHS dip direction. Lateral fining from FA1 to FA2 occurs down-depositional-dip, and, based on paleoflow indicators, downstream. The deposits transition downstream to FA3, and, in AEI and AEVIII, transition down-dip into FA4. Trends down-dip of AIV and AVI occur outside of the area of interest to the west and north, respectively. In planform point bars contain scroll patterns with towards-channel convexity. Therefore, these features describe laterally accreting point bars caused by lateral channel migration.

Counter-Point Bars

AEII, AEV, and AEVII contain mudstone-dominant IHS deposits (FA3) with converging bedding dip directions in planform (Table 2.2; Figs. 2.6A, 2.6B). Paleoflow indicators are often perpendicular to IHS dip directions, but lack of sandstone-rich intervals in FA3 relative to FA1 and FA2 makes paleoflow data difficult to interpret in some locations. These architectural elements are shaped as elongate geobodies that form immediately downstream of point bars. They transition down-dip into FA4 and the up-dip direction points towards and/ or obliquely to the edge of the meander-bend deposit. In planform these deposits contain scroll patterns with towards-channel concavity, providing evidence of downstream meander bend translation (Smith et al., 2009; Ghinassi and Ielpi, 2015; Ghinassi et al., 2016). Due to their FA3 features and planform locations and geometries, these architectural elements are defined as laterally accreting

counter-point bars with downstream translation of the bar (2009; Ghinassi and Ielpi, 2015; Ghinassi et al., 2016).

Abandoned-Channel Fills

AEIII and AEIX contain mudstone-dominant flat lying or very low angle bedding of FA4 (Table 2.2; Fig. 2.6A). Based on well locations these architectural elements form elongated and consistently 150 – 200 m-wide, channel-form geometries when mapped. They occur parallel to scroll patterns, down-dip and adjacent to IHS in FA1, FA2 and FA3 deposits. FA4 morphology and lithology indicate that they are vertically aggrading abandoned-channel fills that partially encase point-bar deposits (Toonen et al., 2012).

Architectural Elements

Architectural Element I: Point Bar 1

AEI is an 800 x 800 m point-bar deposit located in the south-midwestern portion of the area of interest (Fig. 2.6A). AEI transitions to AEII and AEIII to the northeast and north, respectively. Dip-meter measurements indicate flow was primarily north-northwest to north-northeast, with northwest bar accretion and lateral point-bar migration. An increasing arc in radial dip-meter measurements during migration indicates that the bar was expanding and increasing in curvature (Fig. 2.6B). Upward fining trends are observed in cross section (Fig. 2.7), and both down dip and downstream fining trends are evident in planform and outcrop (Figs. 2.6A, 2.8A, 2.8B). The lateral fining towards the northeast demonstrates the hydrodynamic response to increased channel sinuosity (Allen, 1965; Willis, 1989; Hagstrom et al., 2019) as the paleochannel migrates further away from center valley, increasing in mudstone content towards eventual abandonment (Miall, 1981; Durkin et al., 2015).

Table 2. 2 Architectural elements.

Sub-environment	Point bar		Counter point bar	Abandoned channel fill
Architectural Element	AEI, AEIV, AEVI	AEVIII	AEII, AEV, AEVII	AEIII, AEIX
Depositional process	Lateral accretion		Lateral accretion	Vertical aggradation
Migration trend	Lateral migration		Downstream translation	No migration
Facies Associations	FA1, FA2	FA1, FA2, FA5*	FA3	FA4
Bedding character	Diverging IHS bedding dip directions		Converging IHS bedding dip directions	Flat to very low angle bedding
Grain-size trends	Upward fining, down-dip fining, downstream fining		Fine-grained deposits throughout; may contain sandstone base	Fine-grained deposits throughout; may contain sandstone base

Architectural Element II: Counter-Point Bar 1

AEII is an elongated counter-point-bar deposit that trends northwest-southeast, subparallel to an erosional boundary to the northeast, and adjacent to AEI to the southwest (Fig. 2.6A). AEII gradually transitions to AEIII to the northwest. Paleoflow measurements indicate flow towards the northeast and north, and IHS bedding suggests north-northwest bar accretion. Due to the planform concavity of scroll patterns in AEII, it is interpreted that the counter-point bar is translating downstream towards the north-northwest (Page and Nanson, 1982; Ghinassi et al., 2016). The inflection of scroll pattern curvature between AEI and AEII (Fig. 2.6B) indicates a change in depositional style and demarcates point-bar from counter-point-bar deposits (Sylvester et al., 2021).

Architectural Element III: Abandoned-Channel Fill

AEIII is an abandoned-channel fill that lies adjacent to AEI and AEII to the north as an east-to-west elongated mudstone-dominant geobody (Fig. 2.6A). It is truncated by M2.5 deposits to the north and transitions to AEV to the west. The AEIII geobody is up to 24-meters thick (Figs. 2.7, B-B', C-C', D-D'; 2.8D), however, some underlying basal sandstone packages up to

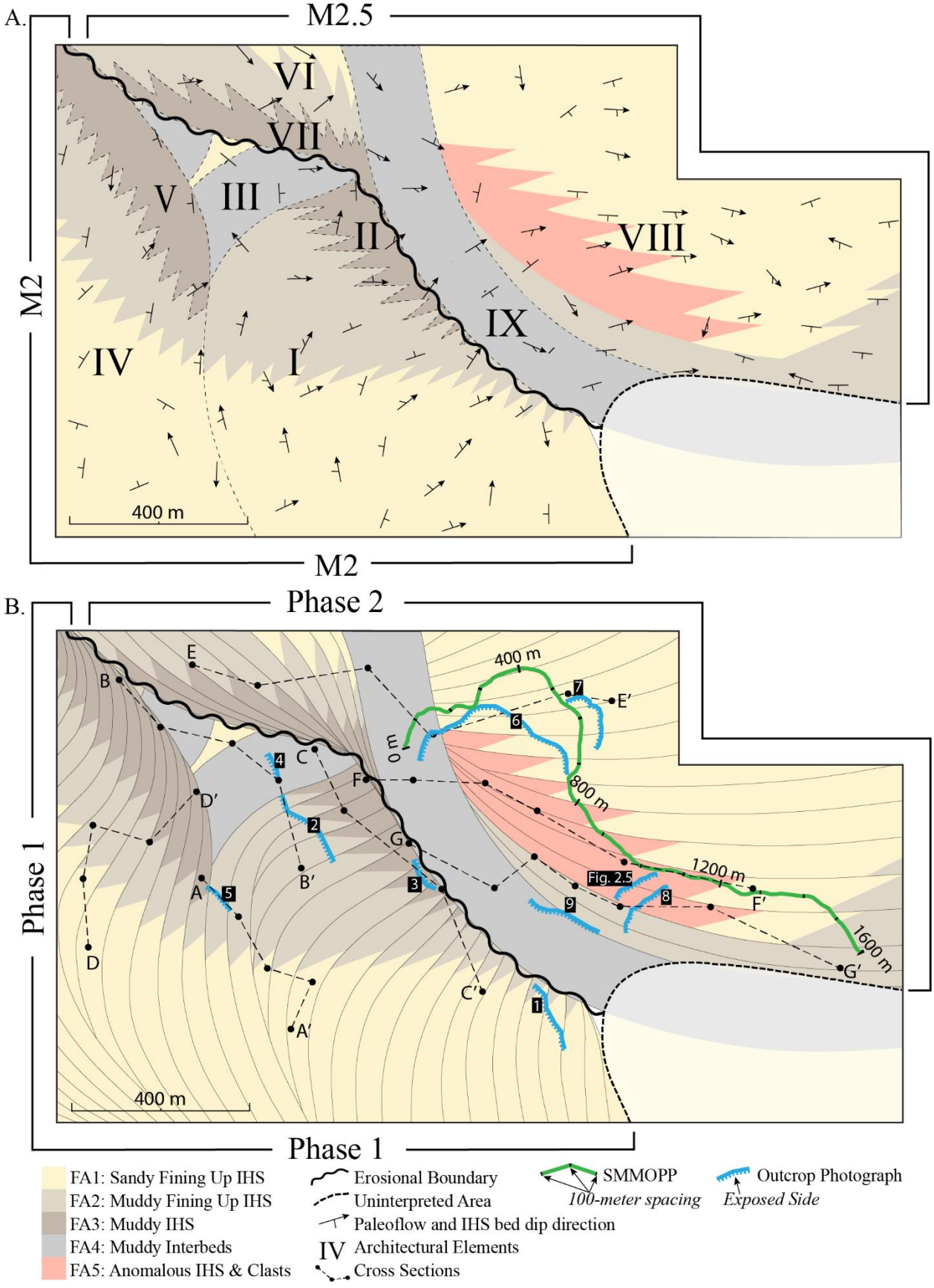
A.
M2.5
M2
VI
VII
V
III
II
VIII
IX
IV
I
400 m
M2
B.
Phase 2
Phase 1
E
B
C
F
D′
G
A
B′
D
A′
C′
E′
F′
G′
400 m
800 m
1200 m
1600 m
Fig. 2.5
1
2
3
4
5
6
7
8
9
Phase 1
FA1: Sandy Fining Up IHS
FA2: Muddy Fining Up IHS
FA3: Muddy IHS
FA4: Muddy Interbeds
FA5: Anomalous IHS & Clasts
Erosional Boundary
Uninterpreted Area
Paleoflow and IHS bed dip direction
IV Architectural Elements
Cross Sections
SMMOPP
100-meter spacing
Outcrop Photograph
Exposed Side

Figure 2. 6 Map analysis of the area of interest. Map colours display facies associations according to well-log and outcrop data. (A) Map that displays the dominant dip direction of sandstone-rich foresets for paleoflow measurements, dominant dip direction of IHS bedding planes for bar migration direction measurements. I – IX represent architectural elements. M2 and M2.5 are separated by the erosional boundary diagonally transecting the map. (B) Map that displays the interpreted scroll patterns derived from dip-meter data in (A). Phase 1 and Phase 2 are equivalent to M2 and M2.5, respectively, and are separated by the erosional boundary diagonally transecting the map. Outcrop locations are displayed with lines. Outcrop for FA5 is shown in Figure 5; outcrops 1 – 5 are displayed in Figure 2.8; outcrop 6 is displayed in Figure 2.11; outcrop 7 is displayed in Figure 2.12; outcrop 8 is displayed in Figure 2.14; outcrop 9 is displayed in Figure 2.16; NECOP is displayed in Figure 2.10; cross sections A-A', B'B', C-C' and D-D' are displayed in Figure 2.7; cross sections E-E', F-F' and G-G' are displayed in Figure 2.9.

10-meters thick are present, providing additional context for paleochannel morphology and size before abandonment. Dip-meter paleoflow measurements in basal sandstone in well 5 of D-D' (Fig. 2.7) suggest, on average, eastward flow. Conversely, well 1 of B-B' (Fig. 2.7) shows paleoflow to the south or southeast. The diverging flow directions are interpreted to represent the locations of the southern (upstream) limb, and northern (downstream) limb of the meander bend before cut-off (Figs. 2.6A, 2.7, B-B', D-D').

Well 4 in B-B' (Fig. 2.7) is located near the meander bend apex of the AEI point bar before abandonment. The bend apex in a channel meander (i.e., point-bar pool; Milne, 1982; Dietrich and Whiting, 1989) is often the deepest point of the channel due to the generation of maximum erosive forces along the outer bank when flow energy is forced through a curved channel (Milne, 1982; Dietrich and Whiting, 1989; Willis and Tang, 2010; Forst, 2019). With subsequent cut-off, the abandoned-channel fill in AEIII preserved upwards of 20-meters of mudstone-dominant sediment here (Fig. 2.7, B-B', wells 3, 4), suggesting that the M2 paleochannel was up to, or over 20-meters deep in some locations.

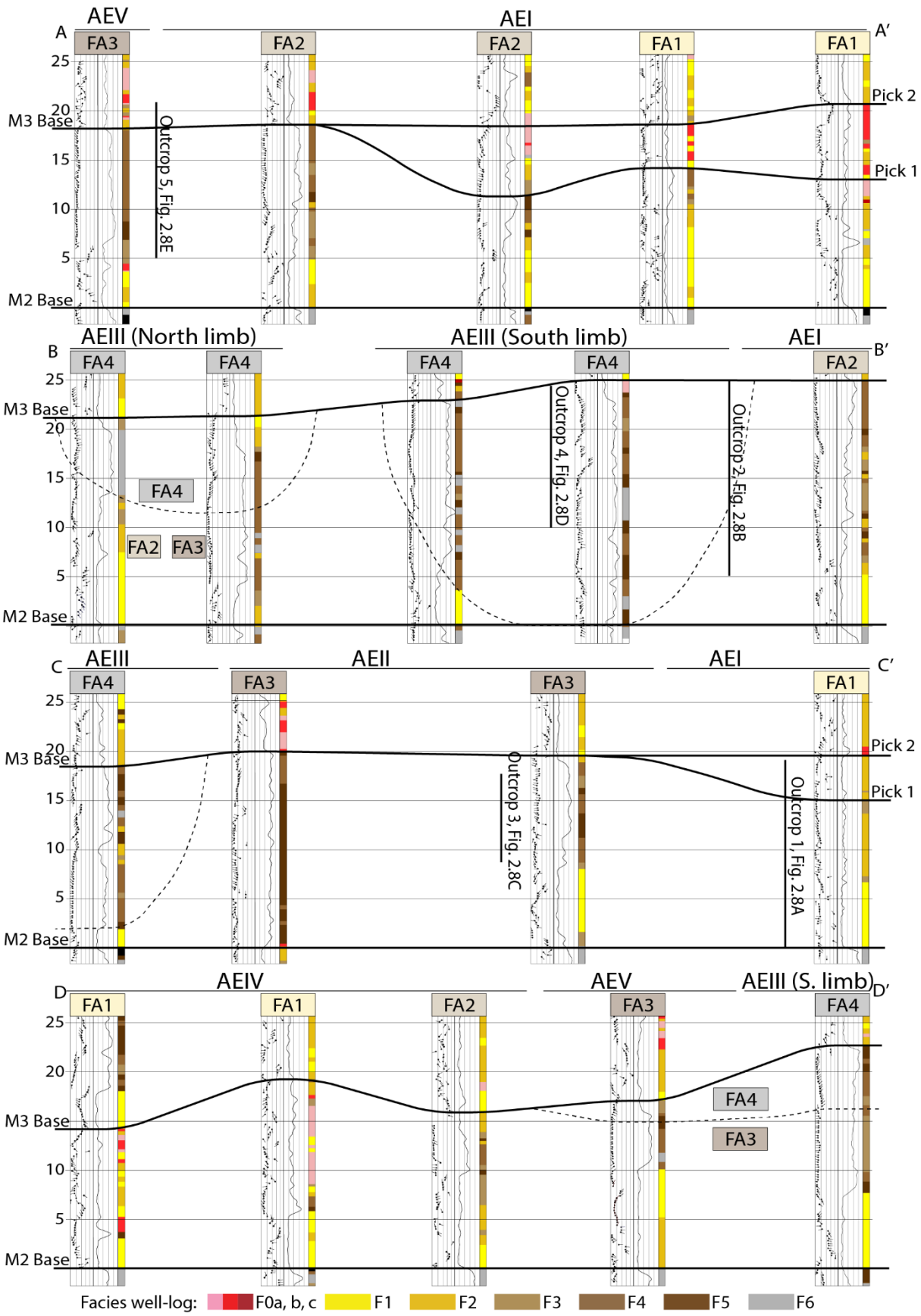
AEV
AEI
A
A′
FA3
FA2
FA2
FA1
FA1
25
20
15
10
5
M3 Base
M2 Base
Pick 2
Pick 1
Outcrop 5, Fig. 2.8E
AEIII (North limb)
AEIII (South limb)
AEI
B
B′
FA4
FA4
FA4
FA4
FA2
FA4
FA2
FA3
Outcrop 4, Fig. 2.8D
Outcrop 2, Fig. 2.8B
AEIII
AEII
AEI
C
C′
FA4
FA3
FA3
FA1
Outcrop 3, Fig. 2.8C
Outcrop 1, Fig. 2.8A
AEIV
AEV
AEIII (S. limb)
D
D′
FA1
FA1
FA2
FA3
FA4
FA4
FA3
Facies well-log:
F0a, b, c
F1
F2
F3
F4
F5
F6

Figure 2. 7 Cross sections A-A', B-B', C-C', and D-D'. Each cross-section location is labelled in Figures 2.2 and 2.6B. Cross section datums are aligned with the base of M2 (0 m in elevation logs). Well-log tracks, from left to right, are elevation in meters above base M2; dip-meter on a scale of 0 - 50°; gamma-ray on a scale of 0 – 150 API; lithofacies distributions based on Table 1 lithofacies. Illustrated bold black lines represent stratigraphic boundaries for base M2, M2.5 and M3. Pick 1 and pick 2 represent possible base M3 picks that are discussed in 2.6.1. Outcrop locations are illustrated on cross sections by vertical lines, representing general locations on the cross section and the exposed mine face elevation. Dotted concave-up lines represent interpreted locations of abandoned-channel fills. Each well-log is labelled by facies association and architectural element above the well-log.

Evidence of a neck cut-off avulsion in AEIII channel abandonment is present in 1) the increasing sinuosity of scroll patterns and fining grain size towards the northwest in AEI (i.e., towards abandonment; e.g., Durkin et al., 2015); 2) the proximity of the interpreted north and south limbs of the abandoned-channel fill, based on basal paleoflow directions, in AEIII; and 3) the thick (> 20 m) mudstone-dominant fill (F5, F6) in AEIII. Mudstone-dominated abandoned-channel fills are common in neck cut-off style avulsions when there is a high-angle of connection with the active channel, promoting rapid plug bar deposition at the entrance to the avulsed meander loop (Toonen et al., 2012; Bellizia et al., 2021). Although a complete meander-fill geometry (i.e., oxbow lake-shape) is not observed to the northeast, it is interpreted that subsequent channel erosion (i.e., M2.5 processes) replaced the northeastern portion of the AEIII abandoned-channel fill (Fig. 2.6A).

Architectural Element IV: Point Bar 2

AEIV is a point bar located along the west and northwestern corner of the area of interest (Fig. 2.6A), bordered by AEV to the northeast, AEI to the southeast and continues outside of the area of interest to the west. AEIV comprises paleoflow indicators and IHS dip orientations that describe a low curvature meander flowing northeast and migrating northwest. A downstream fining component is evident from south to north, continuing grain-size trends observed in AEI.

Based on the lithology and bedding orientation continuity between the AEI and AEIV contact, it is interpreted that AEIV deposition was subsequent to the meander cut-off and termination of AEI deposition.

Architectural Element V: Counter-Point Bar 2

AEV is a thin south-to-north-northwest elongated counter-point-bar deposit that transitions west to AEIV, and east to both AEIII and AEI (Fig. 2.6A). FA3 in AEV comprise mudstone-dominant bedding (Fig. 2.8E) with dip orientations converging in planform towards the west (Fig. 2.6A; Fig. 2.7). No discernable contact is observed during the transition between AEI (FA2) and AEIV (FA3; Fig. 2.8E), however, along the AEIII-AEV contact a vertical transition from FA3 to FA4 can be observed in B-B' (wells 1 and 2) and D-D', (wells 4 and 5; Fig. 2.7). Each of these wells contain sandstone-rich basal deposits with eastward paleoflow indicators, with the exception of B-B', well 2 (Fig. 2.7), which weakly suggests southward paleoflow. Wells with basal deposits indicating eastward paleoflow were likely deposited during AEI, before channel cut-off occurred and overlying deposition of AEIII and AEV began, demarcating a significant adjustment in channel orientation and flow direction in overlying deposits.

Architectural Element VI: Point Bar 3

AEVI is a small, wedge-shaped point-bar deposit in the north-central-west edge of the area of interest, and transitions to AEVII to the south (Fig. 2.6A). Paleoflow and IHS bedding well-log data suggest that AEVI is a north-northeastern migrating point bar with eastern flow (Fig. 2.6A). Data here is sparse as the northern portion of the point bar is located outside of the study, however, some evidence of downstream fining is present from north to south (Fig. 2.6A).

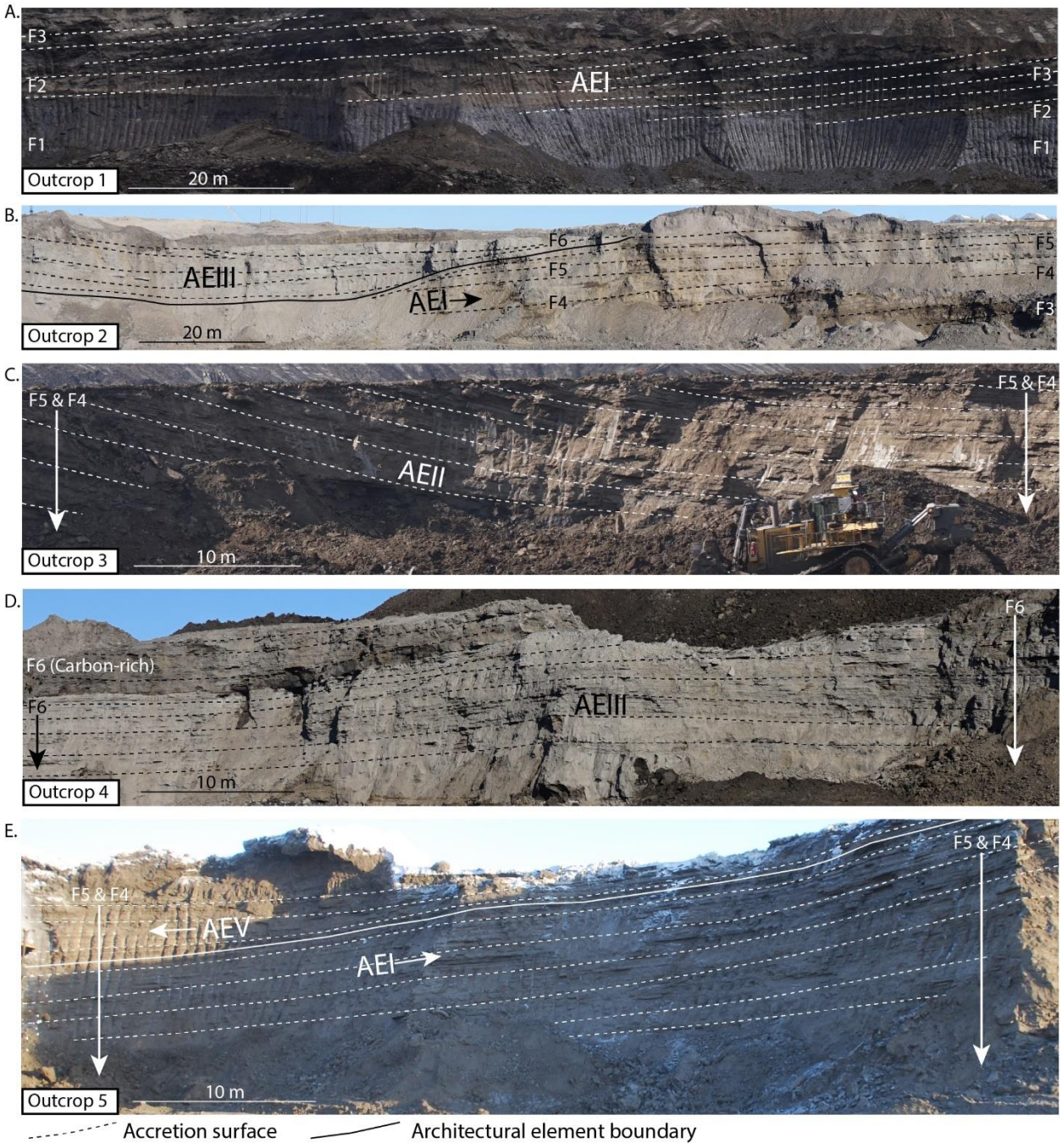

Figure 2. 8 Outcrops in phase 1 (i.e., M2). Each outcrop location is labelled in map-view in figures 2.3 and 2.6B, and in cross sections, showing outcrop elevations, in figure 2.7. Outcrop scales are derived from shovel teeth markings. (A) An outcrop of FA1 located in AEI. (B) An outcrop of FA2 located in AEI (right-side and middle of outcrop) transitioning north into FA4 located in AEIII (far left-side of outcrop). (C) An outcrop of FA3 located in AEII. (D) An outcrop of FA4 located in AEIII. (E) An outcrop of FA2 and FA4 located in AEI and AEIII, respectively.

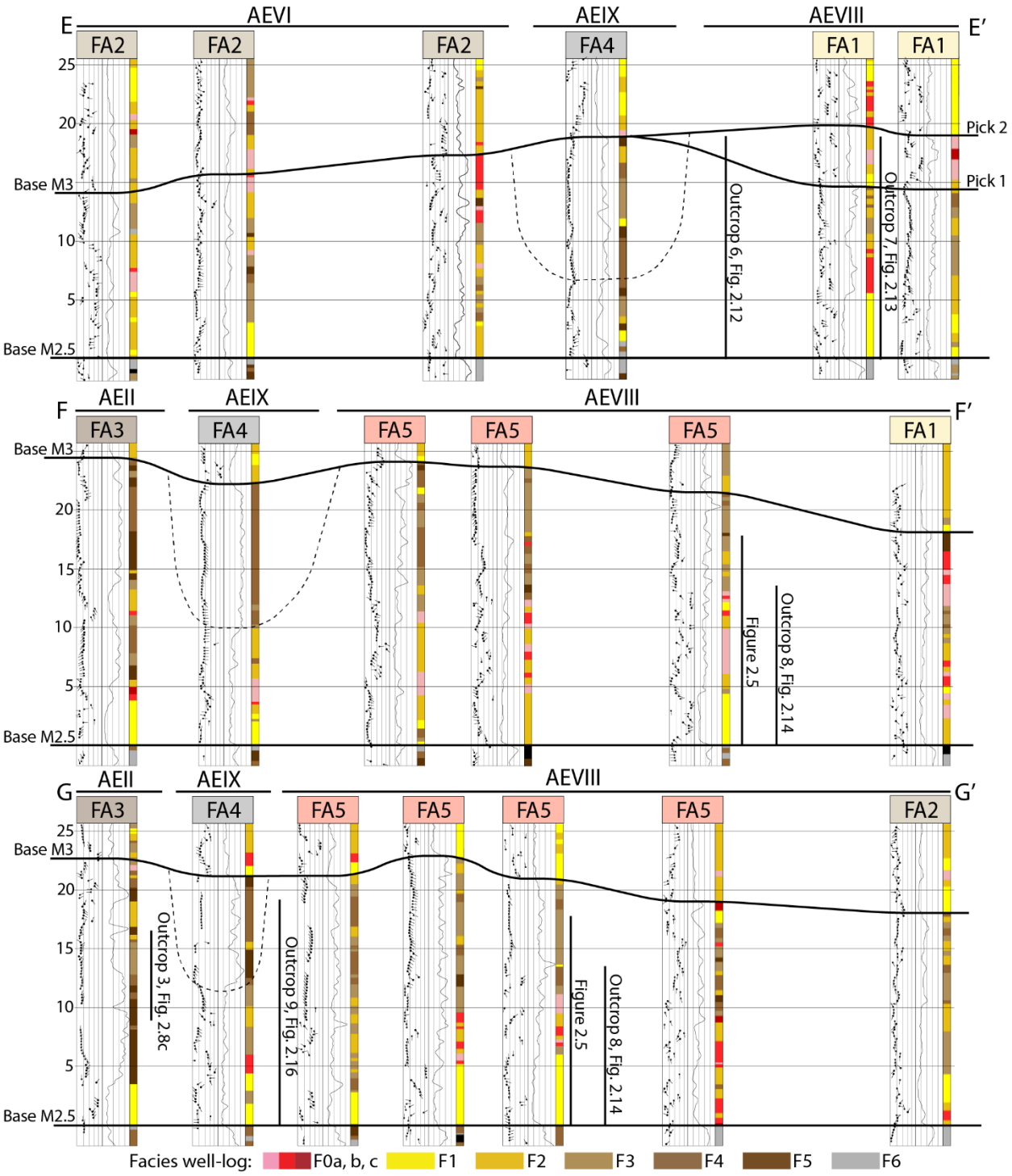

Figure 2. 9 Cross sections E-E', F-F', and G-G'. Each cross-section location is labelled in figures 2.3 and 2.6B. Cross section datums are aligned with the base of M2.5 (0 m in elevation logs). Well-log tracks, from left to right, are elevation in meters above base M2.5; dip-meter on a scale of 0 - 50°; gamma-ray on a scale of 0 – 150 API; lithofacies distributions based on Table 1 lithofacies. Illustrated bold black lines represent stratigraphic boundaries. Pick 1 and pick 2 represent possible base M3 picks that are discussed in section 2.6.1. Outcrop locations are

illustrated on cross sections by vertical lines, representing general locations on the cross section and the exposed mine face elevation. Dotted concave-up lines represent general locations of abandoned-channel fills. Each well-log is labelled by facies association and architectural element above the well-log.

Wells 1 and 2 of E-E' (Figs. 2.6A, 2.9) show acute relationships between IHS bedding and paleoflow dip directions, suggesting association with the downstream translation of the AEVII counter-point-bar deposit.

Architectural Element VII: Counter-Point Bar 3

AEVII is a west-to-east elongated counter-point-bar deposit that transitions from AEVI in the north and erosionally juxtaposes the 20-meter-thick abandoned-channel fill in AEIII to the south. There are no wells that penetrate the interpreted AEVII geobody. However, as stated above, wells 1 and 2 of E-E' (Fig. 2.9) are potentially located on the transition of AEVI and AEVII. These well-log data are extrapolated southward to suggest that AEVII comprises the counter-point-bar deposits immediately downstream of AEVI, forming an eastward translating bar with eastward paleoflow. The IHS bedding dips obliquely away from the erosional contact to the south where thick, erosionally resistant mudstone of AEIII is preserved (Fig. 2.6A). This is similar to description of down-valley translating meander-bend deposits confined by resistant cut bank material in Durkin et al. (2020b). Forced downstream translation has been documented elsewhere when a laterally migrating bar encounters erosionally resistant deposits like the mudstone-dominant abandoned-channel fill observed in AEIII (e.g., Smith et al., 2009; Ghinassi et al., 2016).

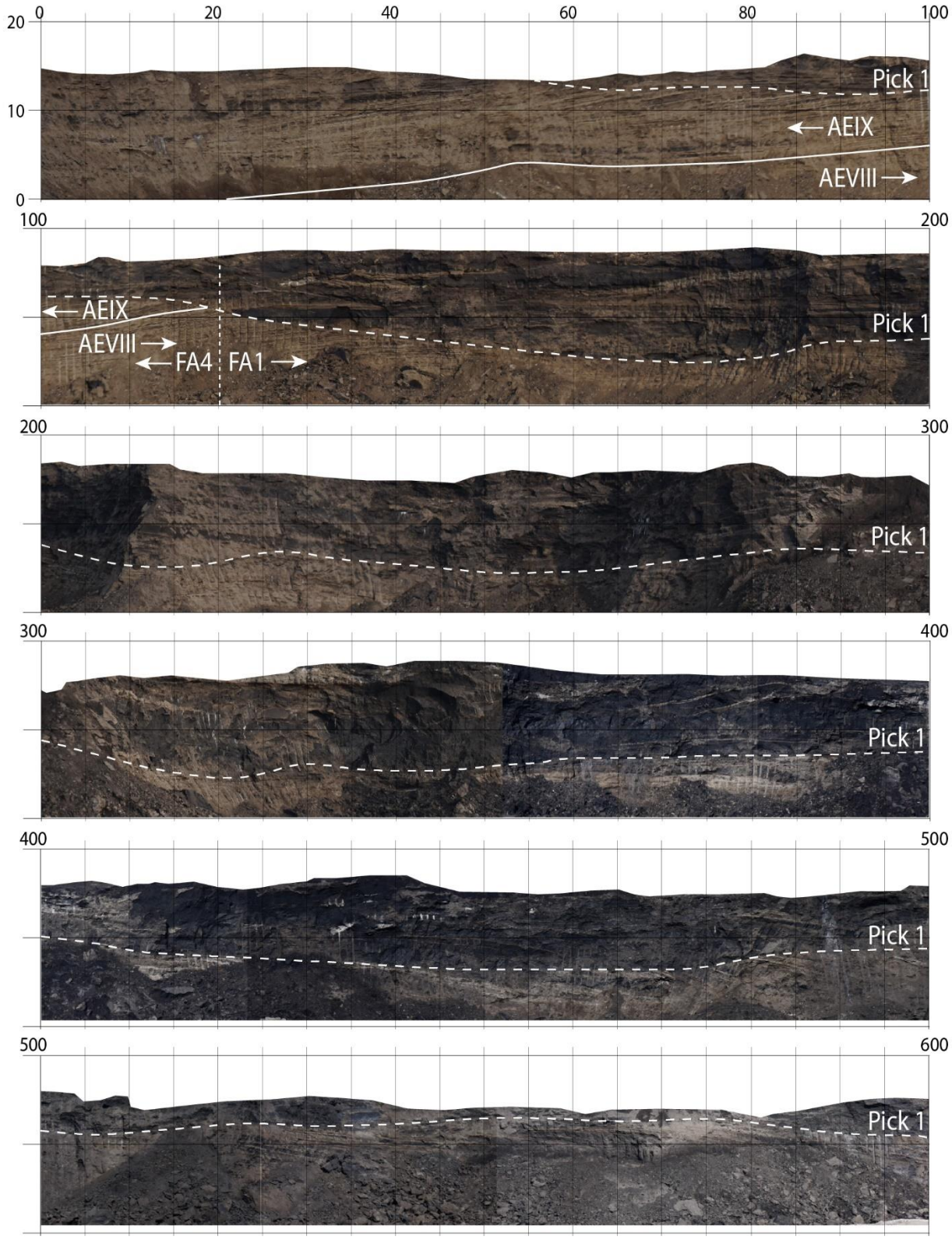
0
20
40
60
80
100
20
10
0
Pick 1
AEIX
AEVIII
100
200
AEIX
AEVIII
FA4
FA1
Pick 1
200
300
Pick 1
300
400
Pick 1
400
500
Pick 1
500
600
Pick 1

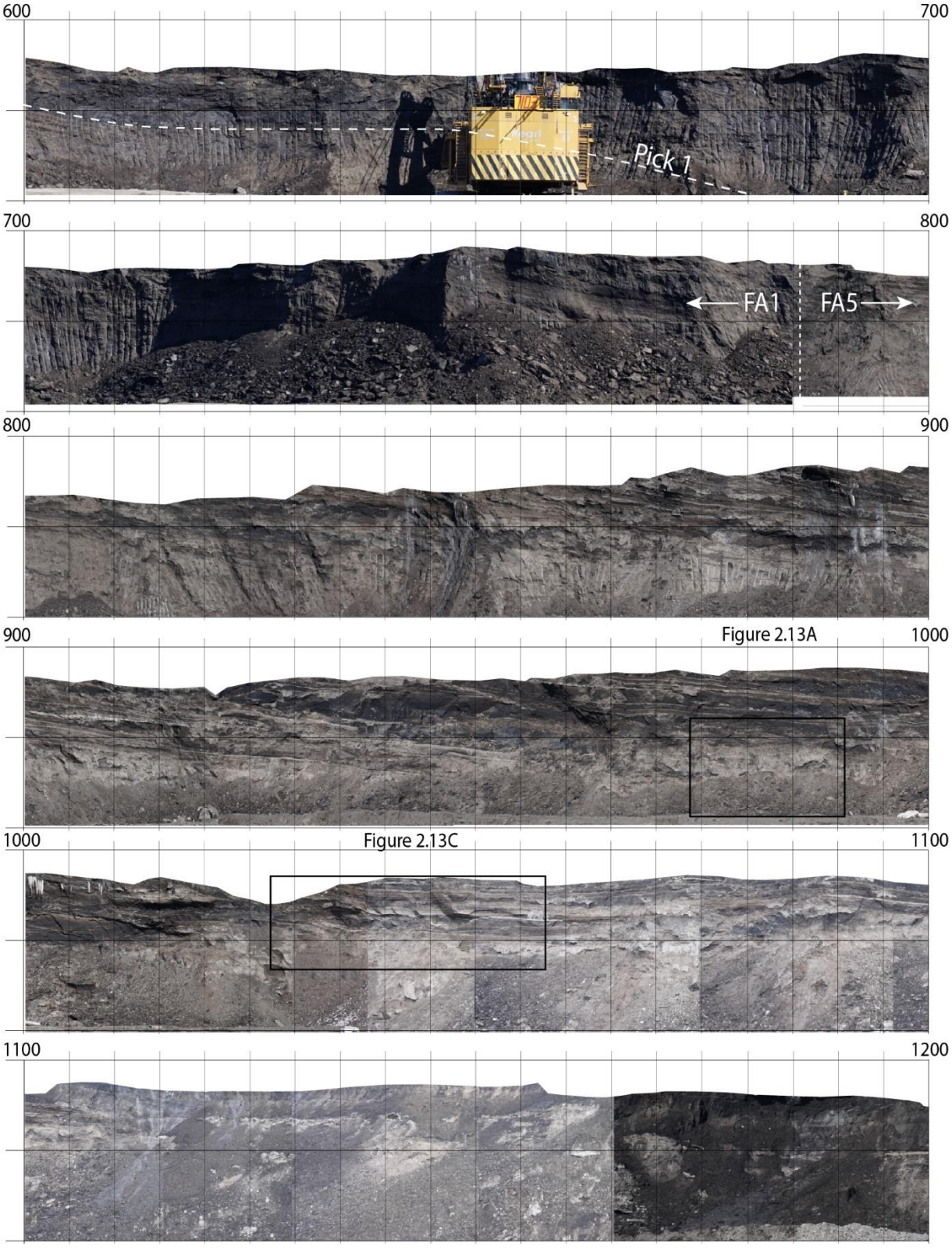
600
700
Pick 1
700
800
FA1
FA5
800
900
900
Figure 2.13A
1000
1000
Figure 2.13C
1100
1100
1200

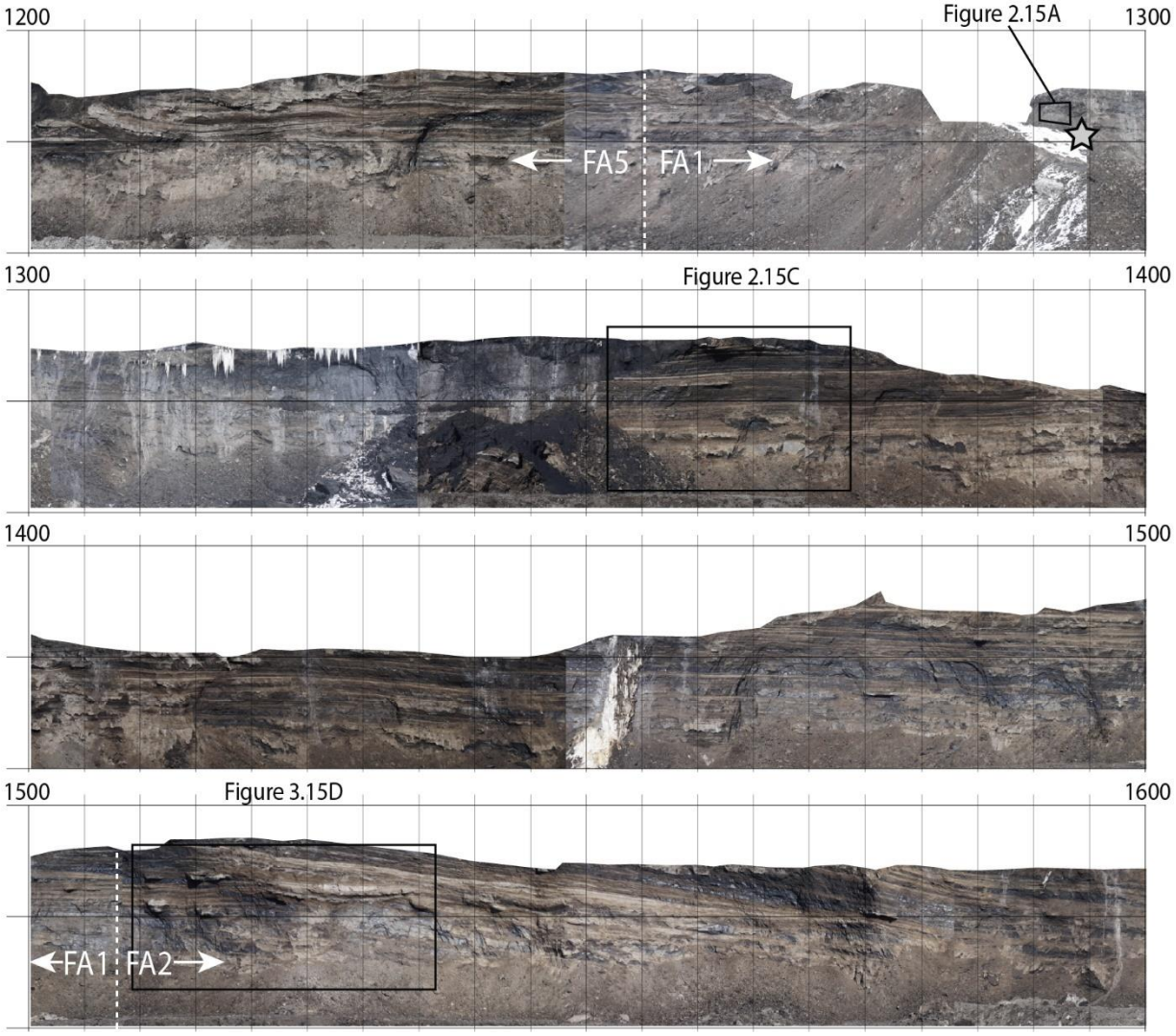

Figure 2. 10 Panoramic photograph of a continuous mine face outcrop in phase 2, named the south-migrating macroforms outcrop panoramic photograph (NECOP). Outcrop location is marked in figures 2.3 and 2.6B. Outcrop scale is derived from shovel teeth marking and LiDAR surveys of the outcrop. Grid scale is in meters. Outcrop base overlies the base of M2.5. Photographs are edited to align the base of outcrop (base M2.5) at 0-meters on the vertical grid-scale. Black squares represent locations of outcrop photographs displayed in figures 2.13A, 2.13C, 2.15A, 2.15C and 2.15D. Mudstone sample collected for Chapter Three is marked by a grey star at the 1296-m-point of the NECOP.

Architectural Element VIII: Point Bar 4

AEVIII is a 1000 x 800 m point-bar deposit in the northeastern portion of the area of interest, and the only architectural element containing FA5 deposits in the study (Fig. 2.6A).

Eastward paleoflow indicators are present in sandstone packages (Fig. 2.9, F-F', G-G'), and IHS bedding suggest southern bar migration (Figs. 2.6A, 2.9). Flow and IHS orientations are relatively consistent throughout AEVIII, indicating low sinuosity in the meander bend. AEVIII transitions to the southwest to AEXI. Down-dip fining is observed from the north-south trending exposure in NECOP (Fig. 2.10, 450 – 1000 m). A downstream fining trend is not consistently observed in AEVIII. Instead, heterolithic deposits are observed throughout the west-east trending exposure in NECOP (Fig. 2.10, 1000 – 1600 m). AEVIII deposits generally host upward fining trends, with the exception of FA5 and some FA1 deposits.

In the northern portion of AEVIII, where FA1 is dominant, upward-coarsening trends are observed. Sandstone-dominant bedsets with depositional planes dipping southward (< 15º), or with concave upward scour surfaces for 10's of meters laterally, locally truncate mudstone-rich IHS deposits 10 – 15 m above the base of M2.5 (Fig. 2.10, NECOP, 120 – 700 m; Figs. 2.11, 2.12). Outcrops show that the sandstone geobodies are continuous for up to 100's of meters laterally and dip orientations of their bedset plane boundaries often appear equivalent to the underlying IHS bedding. When traced laterally and down-dip, the sandstone beds amalgamate with coarse-grained deposits at the base of M2.5 (e.g., Fig. 2.10, NECOP, 120 – 185 m, 430 – 490 m, 585 – 650 m; Figs. 2.11, 2.12). To the south, the FA5 deposits do not adhere to typical upward-fining, nor downstream fining trends.

The FA5 deposits are localized to an approximately 600 x 300 m area on the western-central portion of AEVIII (Fig. 2.6A). Due to pervasive mudstone clasts and mudstone interbedding in FA5, gamma-logs typically display a saw-tooth profile throughout the M2.5 interval (e.g., Figs. 2.5, 2.9, F-F', G-G'). The lower 10 meters are commonly mudstone clast-rich, and outcrop observation shows that mudstone clast breccias can be laterally continuous for

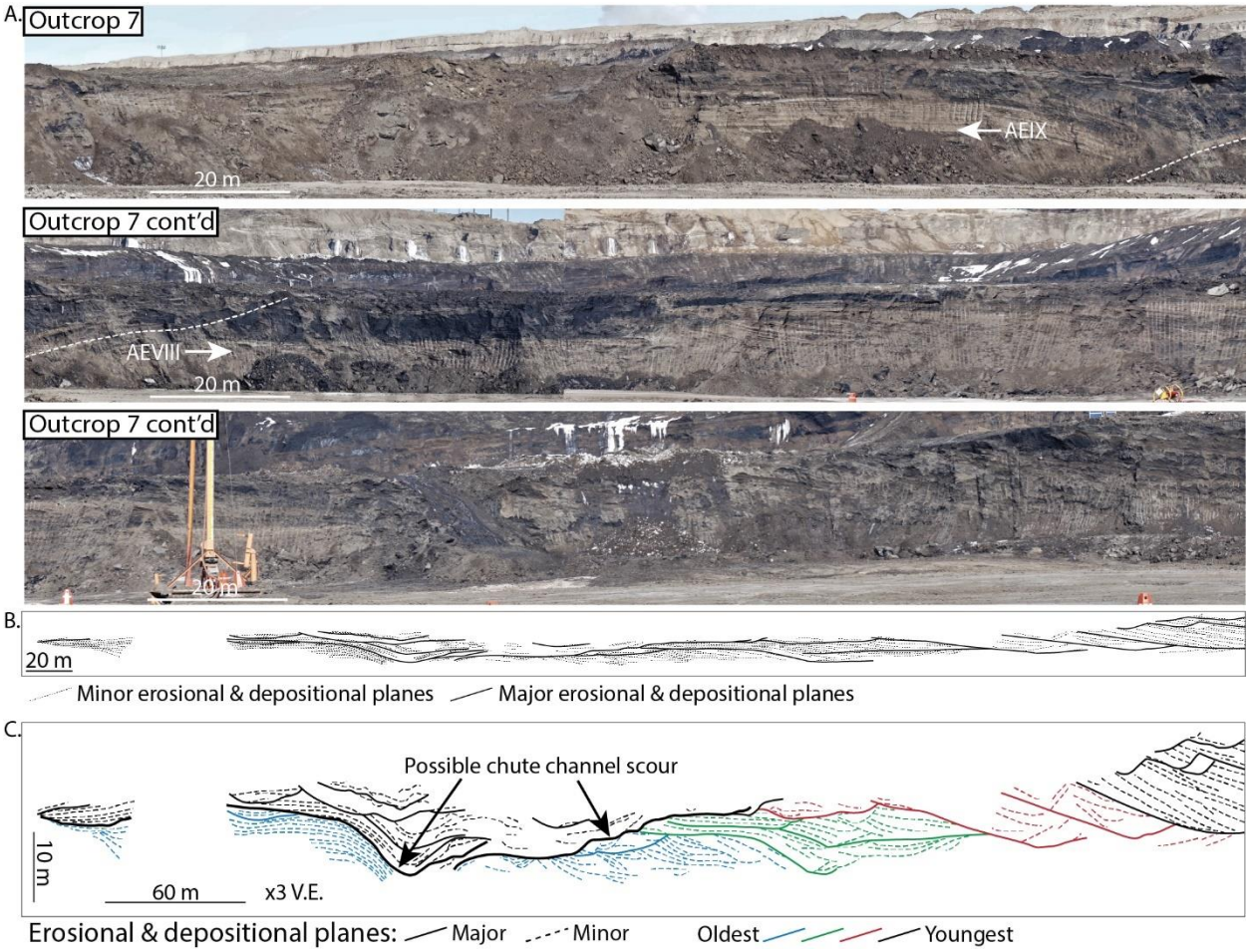

Figure 2. 11 Outcrop 6. Outcrop location is labelled in map-view in figures 2.3 and 2.6B, and in cross section, showing outcrop elevation, in figure 2.9. Outcrop scales are derived from shovel teeth markings. (A) Outcrop photograph of FA1 (B) Traces of major and minor bedding planes and erosional surfaces in outcrop 6. (C) Two-times vertical exaggeration applied to 2.11B. Traces are colour-coded by relative age of successive major erosional stratal packages.

upwards of 200-meters in FA5 (Fig. 2.10, NECOP, 890 – 1110 m; Figs. 2.13, 2.14D, 2.14E, 2.14F). The basal mudstone clast breccias are sand- to boulder-size, elongate, angular and sometimes contain internal structure of mudstone-sandstone interbeds. The pebble- to granule-sized mudstone clasts frequently cluster sub-parallel to one another in stratified, cm-scale foresets and bottomsets in trough cross-bedded structures (Figs. 2.13A, 2.13B, 2.14E), occurring consistently from 930 – 1290 m in NECOP (Fig. 2.10). From 5 – 10 m above the base of M2.5, boulder- to pebble-sized, angular mudstone clasts are observed lining trough-shaped scours and

planar depositional surfaces, often juxtaposed with mudstone-rich IHS bedding (Figs. 2.13C, 2.13D, 2.14F). The average mudstone clast size and proportion decreases toward the eastern edge of FA5. This trend is coupled with increased IHS deposits and bedding continuity towards the east and into FA1 and FA2 deposits (Figs. 2.6A, 2.10, NECOP, 1050 – 1250 m).

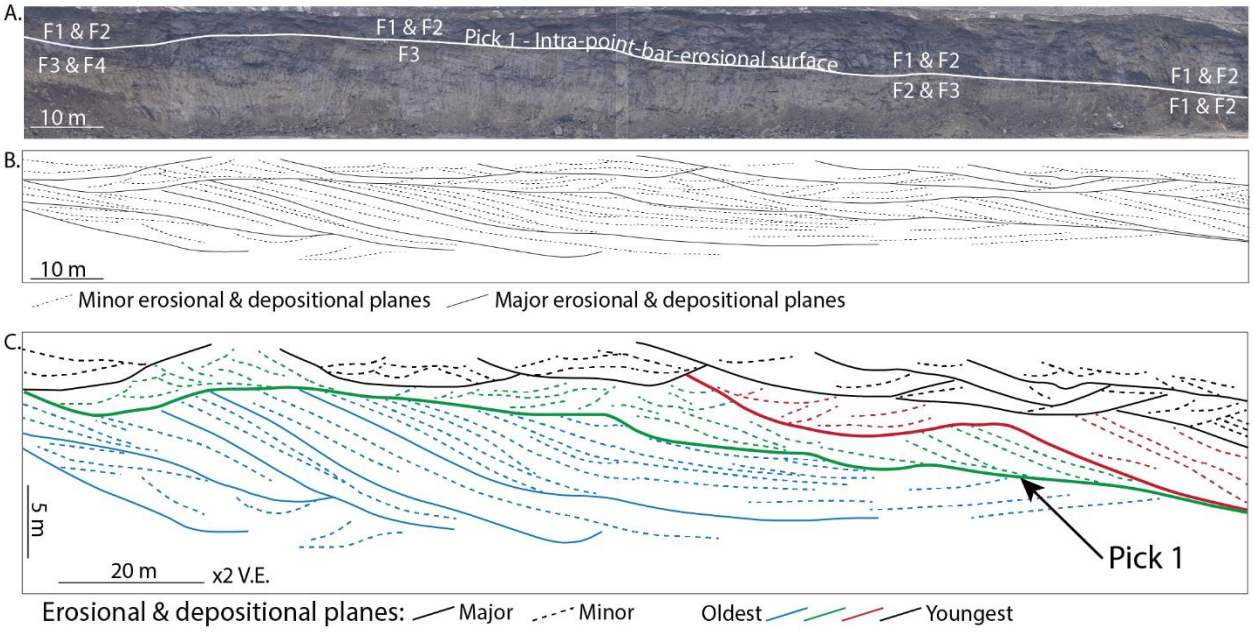

Figure 2. 12 Outcrop 7. Outcrop location is labelled in map-view in figures 2.3 and 2.6B, and in cross section, showing outcrop elevation, in figure 2.9. Outcrop scales are derived from shovel teeth markings. (A) Outcrop photograph of FA2 (bottom) erosionally overlain by FA1 (top). (B) Traces of major and minor bedding planes and erosional surfaces in outcrop 6. (C) Three-times vertical exaggeration applied to 2.12B. Traces are colour-coded by relative age of successive major erosional stratal packages. Bold black line illustrates possible chute channel scour and youngest scour and fill of the outcropping deposits.

The upper 10 – 18 m of FA5 comprise discontinuous IHS bedding and wavy mudstone-sandstone interbeds with interspersed mudstone clast. Although a southward trend in IHS bedding dip direction is observed in outcrop (Fig. 2.10, NECOP, 750 – 1000 m), this is not reflected at the equivalent elevation (10 – 18 m above base M2.5) in most FA5 dip-meter log responses (Fig. 2.9, F-F', G-G'). IHS mudstone interbeds in FA5 are often laterally truncated by local scours or

bedding re-orientation surfaces (Fig. 2.10, NECOP, 1205 – 1215 m, 1230 – 1255 m; Figs. 2.13C, 2.14D). The wavy and inclined mudstone interbeds appear to be lining high-angle depositional planes like trough cross-bed foresets (Figs. 2.5, 2.14F).

Architectural Element IX: Abandoned-Channel Fill 2

AEIX is 180-m wide 1020-m long arcuate-shaped abandoned-channel fill that partially encases AEVIII and erosionally truncates the northeastern borders of AEII and AEI (Fig. 2.6A). In outcrop AEIX is exposed as a 240-m wide and up to 4-m thick mudstone package with a lenticular and concave-up shape (Fig. 2.16A), thinning and pinching out laterally on both sides (Figs. 2.16C, 2.16E). The contact between basal sandstone deposits (F1, F2) and overlying mudstone (F6) is sharp and undulating (Fig. 2.19D); and approximately 8- and 13-m above the base of M2.5 at the lowest and highest points. Above the mudstone body (approximately 11 – 15 m above base M2.5; Fig. 2.9) is mudstone-dominated IHS with pervasive bioturbation (F4, F5; Figs. 2.9, 2.16). The IHS comprises very low-angle bedding that onlaps to the outer cusps of the underlying mudstone body (Figs. 2.16C, 2.16E). Although outcrop in Figure 2.16 initially suggests a cross-sectional slice of the channel, it is not interpreted as such. Instead, the outcrop is aligned sub-parallel with the length of the abandoned channel, as seen in the location of outcrop 9 (Figure 2.6B). Therefore, only the lower and northeastern edge of the abandoned channel is observed here.

The change in hydraulic processes during channel abandonment are captured in outcrop (Fig. 2.16C) where the bottom-channel sand dune bedforms have been preserved and overlain by mudstone, representing a sudden decrease in energy. The IHS overlying this mudstone provides evidence of intermittent periods of subsequent reactivation (Crerar and Arnott, 2007; Labrecque et al., 2011; Brekke et al., 2017; Bellizia et al., 2021), and pervasive bioturbation indicates that

this environment had extended periods of low current speeds and slow sedimentation rates enabling proliferation of burrowing species (Jablonski and Dalrymple, 2016). The concave-up morphology of the mudstone body indicates deposition in a channel-form container (Durkin et al., 2020b), and the onlapping low-angle character of overlying IHS indicates that intermittent pulses of energy cause little to no further migration of the channel form. Abandoned-channel fills with significant proportions of sandstone interbeds are typical when upstream channel avulsion initiates abandonment (Allen, 1965; Toonen et al., 2012), relative to mudstone-rich abandoned-channel fills caused by meander neck cut-offs (e.g., AEIII; Bellizia et al., 2021). Furthermore, the low-curvature of scroll patterns and abandoned-channel fill geometry in AEVIII and AEIX suggests that the meander was of low sinuosity and neck cut-off was not likely (Miall, 1981).

An unconformal relationship is expressed in well-logs between AEIX and deposits of AEI, AEII and AEIII. Well 1 of F-F' (Fig. 2.9) comprises counter-point-bar deposits of AEII with IHS bedding dipping westward, representing sedimentation on the eastern-most outer banks of the paleochannel during AEI and AEII deposition. Well 2 of F-F' shows low-angle IHS (< 8º) dipping south and east, representing the western extent of the paleochannel responsible for AEVIII deposition and AEIX abandonment (Fig. 2.6A). Similar features are present in wells 1 and 2 of G-G' (Fig. 2.9) where the IHS deposits in AEII dip towards the north and basal abandoned-channel fill interbeds in AEIX dip at very low angles (< 5º) towards the southeast (Figs. 2.6A, Fig. 2.9). This unconformal relationship, along with the truncation of the northeastern extent of the abandoned-channel fill in AEIII, suggests that AEI – AEV (i.e., M2) are older deposits that were subsequently eroded and replaced by AEVI – AEIX (i.e., M2.5; Fig. 2.6A).

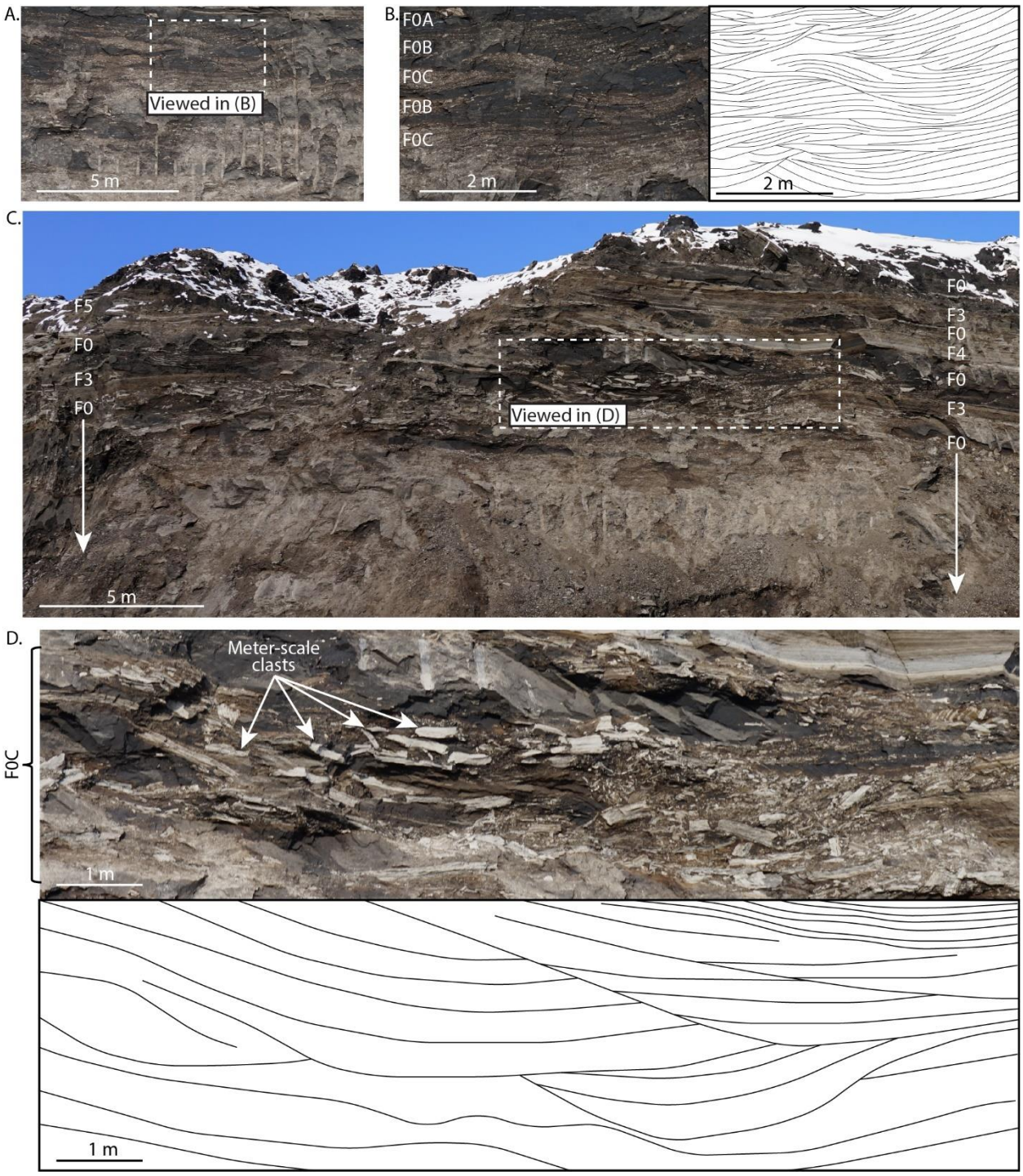

Figure 2. 13 Higher resolution outcrop photographs of selected locations on NECOP that contain mudstone clast breccias. Locations are labelled in Figure 2.10. (A) Outcrop photograph of pebble- to sand-sized mudstone clast breccia in FA5. Dotted white rectangle is viewed in 2.13B. (B) Zoomed in outcrop photograph of 2.13A on the left and traces of bedding planes and erosional surfaces on the right. (C) Outcrop of boulder- to sand-sized mudstone clast breccia in

FA5. Dotted white rectangle is viewed in 2.13D. (D) Zoomed in outcrop photograph of 2.13C on the top and traces of bedding planes and erosional surfaces on the bottom.

2.5.3. Planform Channel Evolution

Planform channel evolution in the area of interest is presented with scroll patterns that represent the temporal-spatial progression of the depositional side of the paleochannel and interpreted locations of the associated abandoned channels (Fig. 2.17). Two chronological phases of deposition are recognized: Phase 1 comprises the older M2 channel-belt deposits (Fig. 2.2) with, on average, northwest bar migration and northeast paleoflow (Fig. 2.6B). Phase 2 partially eroded phase 1 sediment and replaced it with the younger M2.5 channel-belt deposits (Fig. 2.2) with consistent southward bar migration and, on average, eastward paleoflow (Fig. 2.6B). Each phase is divided into 6 stages illustrating the formation of architectural elements I – V in phase 1 (Fig. 2.17A) and architectural elements VI – IX in phase 2 (Fig. 2.17B), which are discussed chronologically below.

Phase 1

The sedimentary characteristics in phase 1 deposits suggest two sets of adjoining point-bar and counter-point-bar deposits (AEI and AEII; AEIV and AEV) temporally separated by the meander-loop cut off and fill (AEIII; Fig. 2.6A). In the southern portion of AEI, depositional surfaces consistently dip toward the west-northwest, representing minimal change in channel orientation through time (Fig. 2.17A, stages 1 – 6). This indicates low channel sinuosity and minimal bed shear that resulted in high flow velocity and coarse-grained deposition in the upstream bar location (FA1; Miall, 1985; Dietrich and Whiting, 1989; Hagstrom et al., 2019). The shift to finer-grained IHS deposits (FA2) northward is linked to increased meander bend

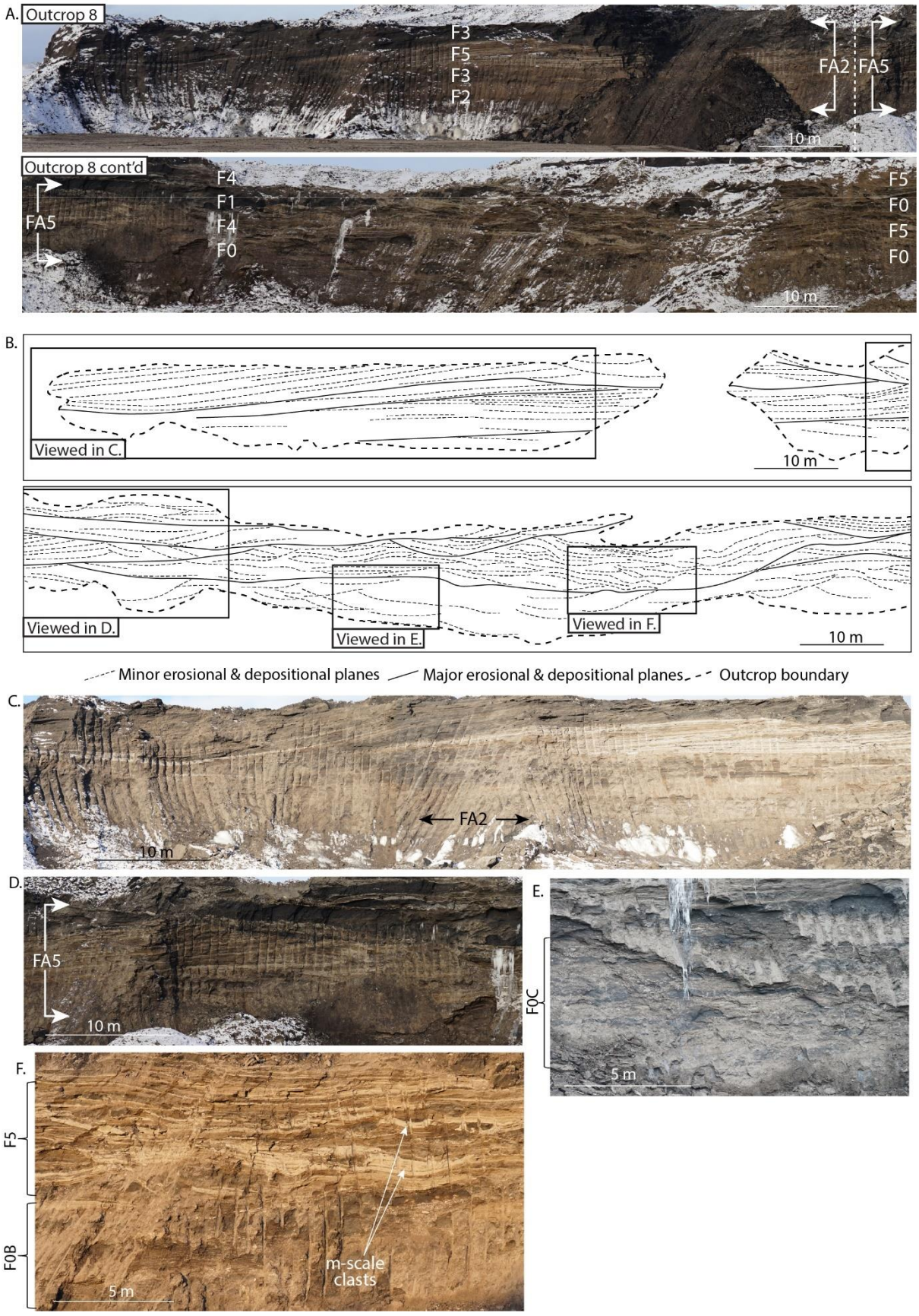
A.
Outcrop 8
F3
F5
F3
F2
FA2
FA5
10 m
Outcrop 8 cont'd
FA5
F4
F1
F4
F0
F5
F0
F5
F0
10 m
B.
Viewed in C.
10 m
Viewed in D.
Viewed in E.
Viewed in F.
10 m
Minor erosional & depositional planes
Major erosional & depositional planes
Outcrop boundary
C.
FA2
10 m
D.
FA5
10 m
E.
F0C
5 m
F.
F5
F0B
m-scale clasts
5 m

Figure 2. 14 Outcrop 8. Outcrop location is labelled in map-view in figures 2.3 and 2.6B, and in cross section, showing outcrop elevation, in figure 2.9. Outcrop scales are derived from shovel teeth markings. (A) Complete outcrop photograph. Locations of photographs in 2.14B – F are labelled by dotted white rectangles. Outcrop deposits comprise FA5 on the right, transitioning southwest to FA2 on the left. (B) Traces of major and minor bedding planes and erosional surfaces in outcrop 8. Locations of photographs in 2.14B – F are labelled by dotted black rectangles. (C) Outcrop photograph of FA2. (D) Outcrop photograph of FA2 (bottom) erosionally overlain by FA5 (top). (E) Outcrop photograph of mudstone clast breccia in FA5. (F) Outcrop photograph of mudstone-lined trough-shaped beds with large mudstone clasts in FA5.

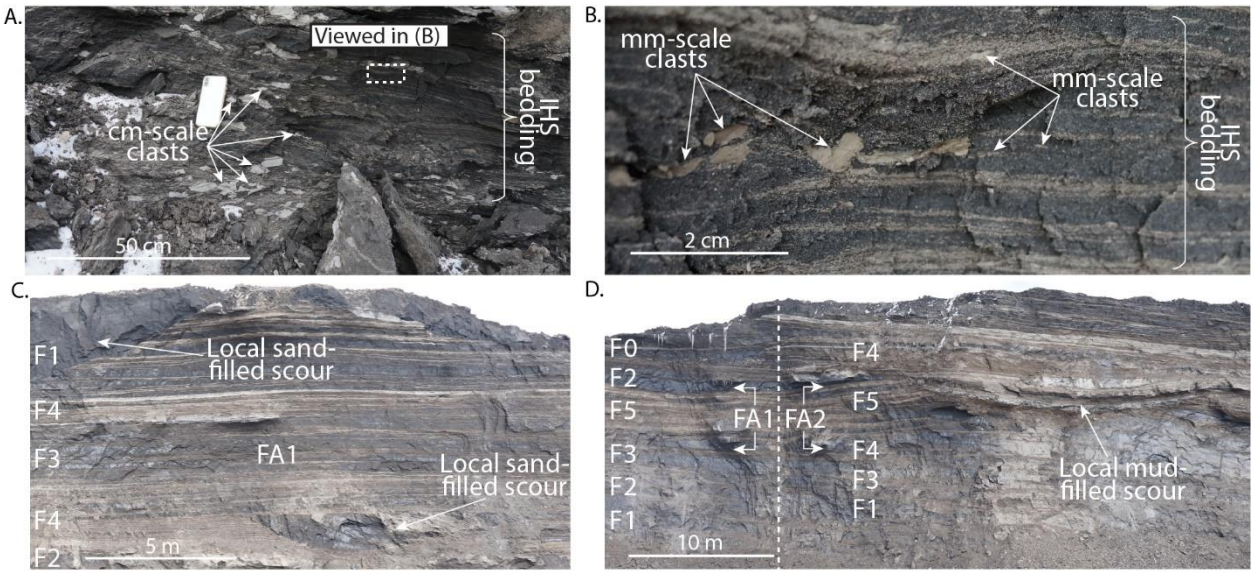

Figure 2. 15 Higher resolution outcrop photographs of selected locations on NECOP that contain FA1 IHS deposits and discrete granule- to sand-sized mudstone clasts. Locations are labelled in Figure 2.10. (A) Outcrop photograph sandstone-mudstone interbeds in IHS deposits, lined with discrete mudstone clasts in FA1. White rectangle is viewed in 2.15B. (B) Zoomed in photograph of 2.15A showing sandstone-mudstone interbeds lined with mudstone clasts down to sand-sized and perhaps less. Mudstone interbeds may comprise mudstone aggregates. (C) Outcrop photograph of semi-continuous, planar IHS bedding in FA1 showing overlying scour and fill (top left). (D) Outcrop photograph of semi-continuous, planar IHS bedding in FA1 showing disconformal surfaces.

curvature around the bend and decreased flow velocity downstream of the bar apex (Wood et al., 1989; Labrecque et al., 2011; Jablonski, 2012; Hagstrom et al., 2019). The depositional surfaces dip westward in the western and southern portion of AEI, and northward in the northern and eastern portion (Fig. 2.6A), documenting an element of lateral point-bar expansion (e.g.,

Ghinassi and Ielpi, 2015; Shan et al., 2018; Hagstrom et al., 2019) during evolution (Fig. 2.17A, stages 1 – 3).

Downstream of AEI is a transition to AEII. Depositional surface dip directions between AEI and AEII wells change from diverging to converging in planform view, marking an inflection point of the meander bend (e.g., Sylvester et al., 2021). Downstream of the inflection point the bar migration style changes to downstream translation (e.g., Ghinassi et al., 2016; Shan et al., 2018; Sylvester et al., 2021). Downstream translation is often observed when further lateral point-bar migration/ expansion is mitigated by erosionally resistant substrate (e.g., mudstone-rich deposits), confining lateral growth but promoting down-valley counter-point-bar growth (Page and Nanson, 1982; Ghinassi et al., 2016). The AEII downstream translation is concurrent with lateral expansion of AEI (Fig. 2.17A, stages 1 – 3).

Increasing northwestward curvature in the AEI point bar culminated in meander neck cut-off, leaving an ox bow lake that in-filled with fine grained sediment in AEIII (Fig. 2.17A, stages 4 – 6). Point-bar rotation is common when elevated channel discharge inundates the point-bar surface and flow is directed across the point bar, shifting the location of maximum erosion on the outer bank downstream (Dietrich and whiting, 1989). This results in episodic channel geometry changes with successive energetic events (Thorne and Lewin, 1979; Shan et al., 2018). It is interpreted that continued downstream shifting of high velocity currents and resulting outer bank erosion caused clockwise and downstream rotation coupled with lateral expansion. This combination typically results in higher channel sinuosity and frequency of meander bend cut-offs (Shan et al., 2018). The moment of neck cut-off (Fig. 2.17A, stages 4 – 5) marks the termination of AEI and AEII deposition and onset of AEIV and AEV.

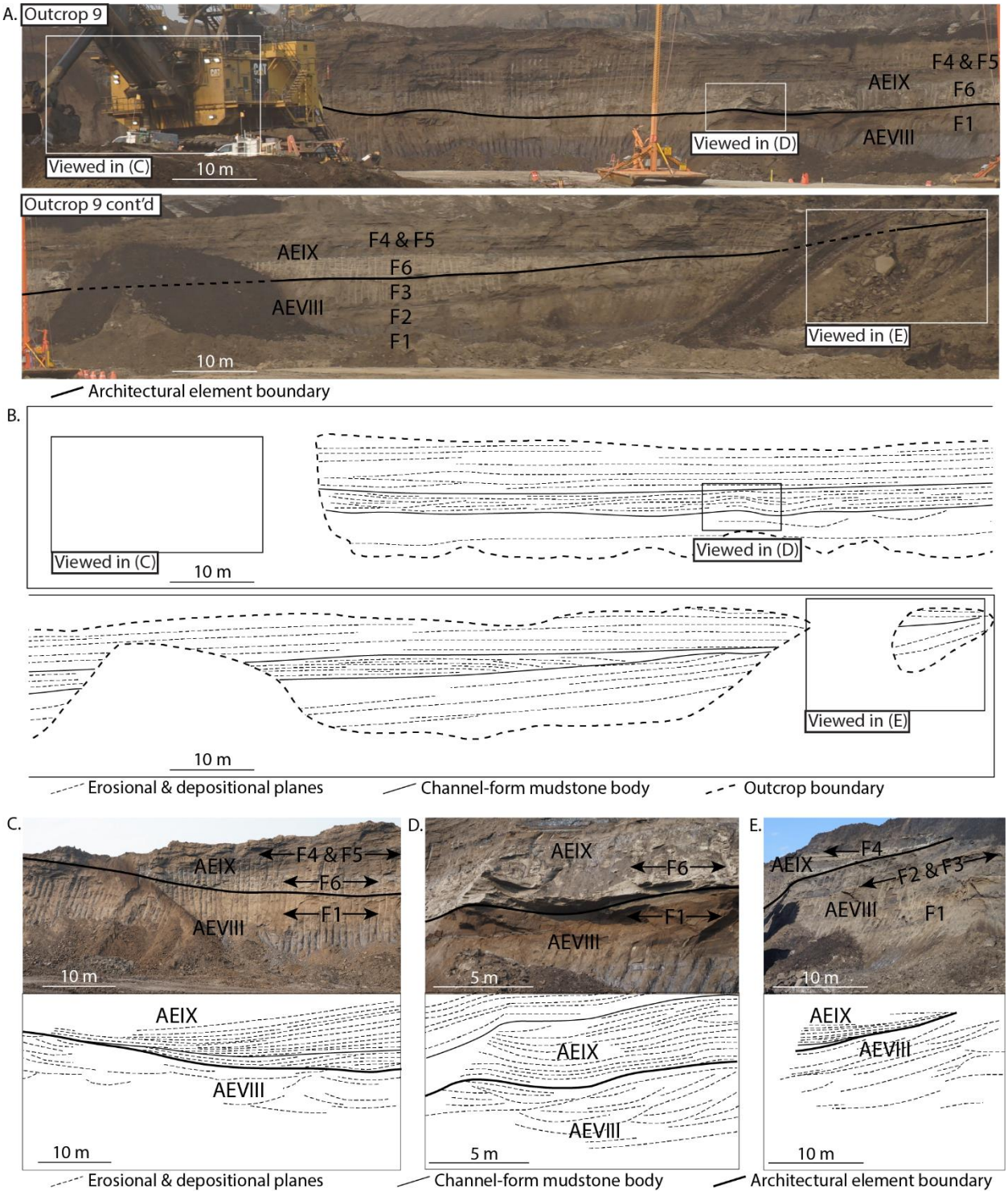

Figure 2. 16 Outcrop 9. Outcrop location is labelled in map-view in figures 2.3 and 2.6B, and in cross-section, showing outcrop elevation, in figure 2.9. Outcrop scales are derived from shovel teeth markings. (A) Complete outcrop photograph. Locations of photographs in 2.16C - E are labelled by dotted white rectangles. (B) Traces of major and minor bedding planes and erosional surfaces in outcrop 9. Channel-from body is traced in bold black line. Locations of photographs in 2.16E – C are labelled by dotted black rectangles. (C) Outcrop photograph of cross-bedding

and IHS deposits at the base in contrast with the channel-from mudstone and overlying flat interbeds that downlap to the mudstone body. Bedding planes and erosional surfaces are traced below. Channel-form body is traced in bold black line. (D) Outcrop photograph cross-bedded sandstone sharply overlain by channel-form mudstone deposits. A trough-shaped contact is observed. Bedding planes and erosional surfaces are traced below. Channel-from body is traced in bold black line. (E) Outcrop photograph of IHS deposits at the base overlain by channel-from mudstone and overlying flat interbeds that downlap to a channel-form container. Bedding planes and erosional surfaces are traced below. Channel-from body is traced in bold black lines.

No observable lithological or structural contact is present between the FA1-FA1 (Fig. 2.6A) and FA2-FA3 (Figs. 2.6A, 2.8E) deposits in point bars of AEI and AEIV. Deposition between the architectural elements is interpreted to be continuous through the meander cut-off transition described above. However, significant change in IHS bedding orientation and associated scroll pattern geometries reflect a drastic change in channel trajectory near the cut-off location during stages 3 to 5 (Fig. 2.17A).

The associated counter-point bar (AEV) comprises diagnostic FA3 features adjacent to abandoned-channel fill deposits of AEIII (Fig. 2.6), suggesting a swift transition from channel cut-off to northwestward bend translation in AEV (Fig. 2.17A, stages 4 – 6). In well 2 in B-B', and wells 4 and 5 in D-D' (Fig. 2.7), IHS bedding with westward dips that converge in planform are terminated approximately 10 – 15 m above base M2. Deposits above are very low-angle, mudstone-rich bedding typical of FA4, that steepen upward with dips towards the east. Sylvester et al. (2019) suggests that sedimentation rates of counter-point-bar deposits can be slower relative to migration velocity of the channel, resulting in counter-point bar deposition in lower topographic elevation relative to the adjoining point bar and surrounding floodplain. The FA4 deposits overlying FA3 in AEV (Fig. 2.7, B-B', D-D') are interpreted to be deposited in a floodplain lake that was left in the wake of the counter-point-bar migration pathway of AEV in stages 4 – 6 (Fig. 2.17A).

Phase 2

Phase 2 comprises a series of bars (elements VI, VII, VIII) that migrated primarily south and east, partially eroding and replacing phase 1, before stalling and gradually abandoning in a position that transects the mid-study area from north to southeast, leaving a mudstone-rich channel fill behind (AEIX; Figs. 2.6A, 2.17B). The onset of phase 2 in the area of interest is interpreted as a southward migrating point bar (AEXIII) with eastward paleoflow, cutting through the northeastern remnants of phase 1 abandoned-channel fill material in AEIII (Fig. 2.17B, stage 1). Cutbank material in phase 2, stage 2 (Fig. 2.17B) comprises up to 20-meter-thick mudstone-rich sediment (Fig. 7, B-B', wells 3 and 4) that is resistant to erosion relative to sandstone-rich deposits. In response, the location of maximum erosion was deflected downstream, encouraging eastward bar translation and minimizing lateral point-bar growth (e.g., Ghinassi et al., 2016; Durkin et al., 2020b; Fig. 2.17B, stages 2, 3). Downstream translation initiates deposition of the adjacent point and counter-point bars (i.e., AEVI and AEVII) inside the area of interest, and removes the initial AEVIII point-bar deposits on the north-northwestern edge of the map in phase 2, stages 1 – 3 (Fig. 2.17B). IHS bedding surfaces in AEVI and AEVII dip obliquely away from the adjacent unconformity (Fig. 2.6A), representing the margin between phase 2 and the abandoned-channel fill in AEIII (e.g., Durkin et al., 2020b).

When the paleochannel bend apex reaches less-resistant cutbank material (Fig. 2.17B, stages 3 and 4) the channels erosional and depositional processes evolve once more. With cutbank material no longer restricting lateral bar growth, preferential southward migration is restored (e.g., Durkin et al., 2020b, their Fig. 12, stages 3 and 4). In AEVIII this results in broad lateral point-bar expansion and deposition (Fig. 2.17B, stages 4 – 6) before upstream channel

avulsion is interpreted, initiating abandoned-channel fill deposition in AEIX (Fig. 2.17B, stage 6).

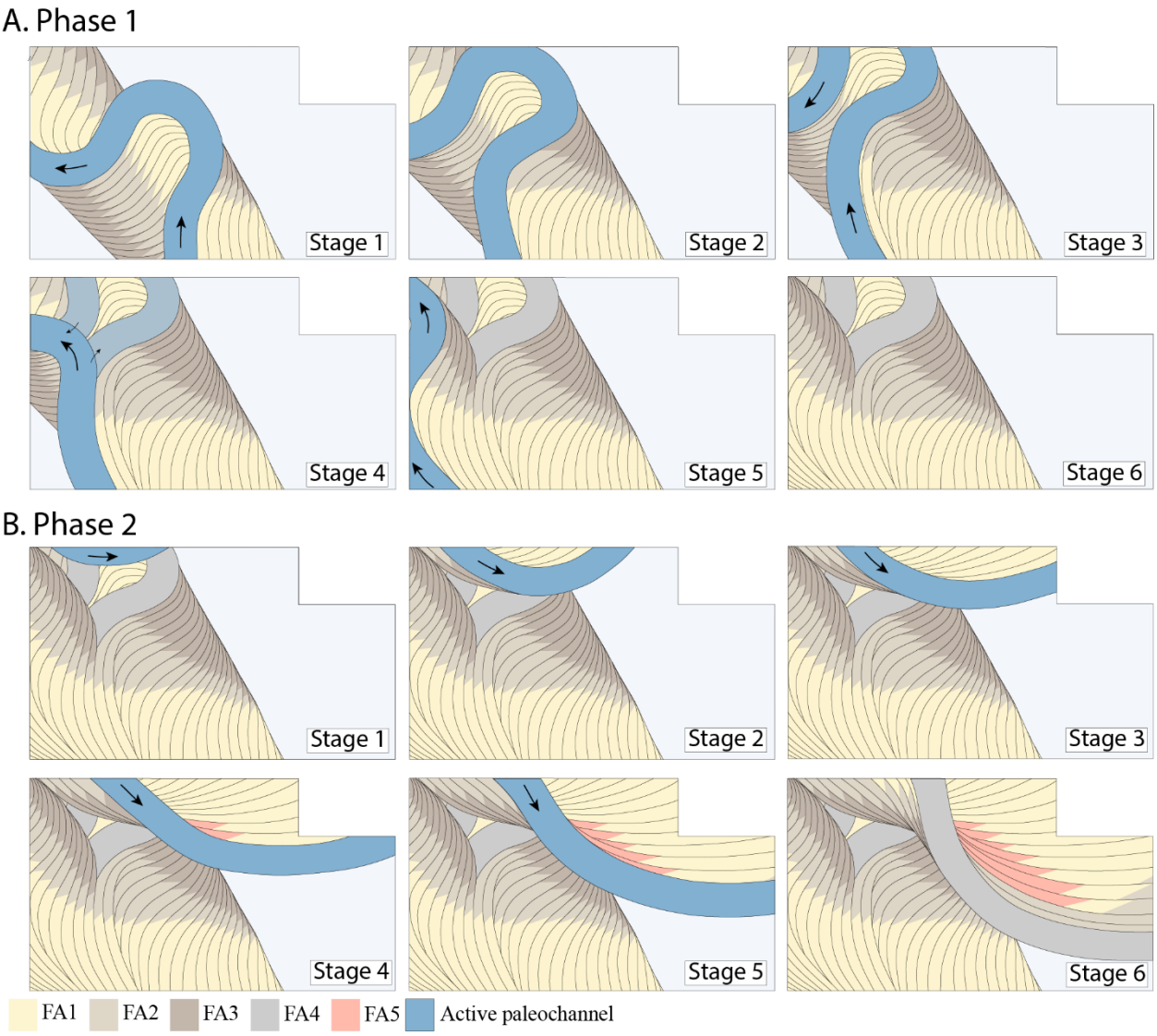

Figure 2. 17 Planform channel evolution in the area of interest. Channel scroll patterns illustrate the paleochannel evolution interpreted to have deposits M2 deposits in phase 1, stages 1 – 6; and M2.5 deposits in phase 2, stages 1 – 6.

2.6. Discussion

2.6.1. Implications for point-bar models

The approach to meander-belt deposit characterization in this study utilizes a rare opportunity to integrate conventional subsurface data with mine-face exposures of those deposits (e.g., Nardin et al., 2013). A direct data-to-outcrop comparison can help to test the validity of theorized and documented point-bar facies trends and refine future modelling and interpretations when analogous subsurface data is analyzed. Documented trends in point-bar grain sizes include upward fining (e.g., Allen, 1965; Nanson, 1980; Bridge et al., 1995), downstream fining from the bend apex (e.g., Leeder and Bridges, 1975; Jackson, 1976; Bridge et al., 1995), and fining with increased channel sinuosity (e.g., Thomas et al., 1987; Durkin et al., 2017). Furthermore, channel morphodynamics have a direct influence on the hydraulic processes of point-bar deposits. For example, point bars often transition from overall lateral expansion to downstream translation (e.g., Daniel, 1971) when the cutbank encounters erosionally resistant substrate (e.g., Burge and Smith, 1999; Smith et al., 2009; Ghinassi et al., 2016), but the resulting counter-point-bar deposits can be difficult to discern from mudstone-rich point-bar IHS or abandoned-channel fills (Durkin et al., 2017; 2020b).

In phase 1 of the area of interest (M2 channel-belt; Figs. 2.2A, 2.6A), examples of the point-bar trends discussed above, and depositional changes in response to channel evolution are evident. Upward fining trends are present in all individual FA1 and FA2 wells and outcrop photographs within AEI (Figs. 2.7, 2.8A, 2.8B), and outcrops, cross sections and planform reconstructions provide evidence of upward-fining, downstream-fining, and fining with increased channel sinuosity (Figs. 2.8A, 2.8B). The increasing proportion of mudstone in IHS is tied with increasing consistency in bedding dip angle and azimuth on the point-bar surface (e.g.,

Brekke et al., 2017; Chen et al., 2022). This results in robust IHS dip-meter data that can be used to reconstruct the curvature of the point-bar accretion surfaces (i.e., scroll patterns) in planform (Fig. 2.6A), illustrating the presence of typical downstream fining around the bend apex (e.g., Labrecque et al., 2011; Hagstrom et al., 2019). AEI channel curvature transitions from west- to northwest-dipping FA1 deposits in the south (e.g., Fig. 2.8A), to north-dipping FA2 deposits in the north (e.g., Fig. 2.8B). An increase in curvature of the meander is also notable by the increasing proximity of west-dipping beds to north-dipping beds towards the northwest (Fig. 2.6A). Channel curvature continues to increase throughout phase 1, stages 1 – 4 (Fig. 2.17) until eventual neck cut-off and channel abandonment in AEIII. Towards the west of AEI and AEIII, however, point-bar trends resume in AEIV through phase 1, stages 4 – 6. (Fig. 2.6A, Fig. 2.17).

The point bar to counter-point bar transitions in AEI to AEII, and AEVI to AEV is recognized by three criteria: i) convex to concave, towards-channel accretion patterns (e.g., Sylvester et al., 2021), ii) downstream grain-size fining across meander inflection point (e.g., Ghinassi et al., 2016; Durkin et al., 2020b; Sylvester et al., 2021), and iii) upward fining in the adjoining point bar is replaced by consistent fine-grained deposition throughout the counter-point-bar interval (e.g., Smith et al., 2009). In traditional borehole-only datasets, mudstone-rich deposits with a lack of a vertical grain size trends may be interpreted as abandoned-channel fills (e.g., Durkin et al., 2017). Without a detailed planform reconstruction that considers accretion surface geometry, curvature, and concavity (i.e., paleochannel position and orientation over time), certain FA3 packages would be difficult to distinguish from FA4 or some FA2, which could result in improper lithofacies projections in model building methods. For example, without integrating the relationships of bedding orientations throughout the study area, AEII (Fig. 2.8C), AEIII (Fig. 2.8D) and AEV (Fig. 2.8E) could be interpreted as a single continuous mudstone-rich

geobody. For improvements in modelling and other predictive geologic qualities, planform reconstruction and paleochannel evolution is critical to properly integrate known geologic trends in channel-belt deposits, and to further contextualize previously undocumented and/ or atypical trends.

Although point bars with typical upward- and downstream-fining trends are regularly observed in modern and ancient examples, peculiar and anomalous features within them often exist. Exceptions to typical models can be troublesome in predictive practices because they may deteriorate interpretational validity and decrease the accuracy of extrapolated data for modelling. Therefore, a solution is to document and define the atypical point-bar trends, ultimately linking them to the related environmental conditions and the processes involved in their formation. AEVIII deposits in phase 2 are characterized by local examples of atypical point-bar trends. They comprise upward coarsening units in the north and FA5 in the southwest portions of AEVIII (Fig. 2.6A). It is notable that the entire AE is not atypical, as the east portion of AEVIII is characterized by upward fining IHS intervals that are typical of downstream point-bar deposits (Fig. 2.15).

2.6.1.1.Upward coarsening deposits

Upward coarsening deposits are present in the north-central portion of AEVIII (Figs. 2.10, NECOP, 120 – 700 m; Figs. 2.11, 2.12) and shown in cross section (Fig. 2.7, A-A', C-C') where "Pick 1" represents the base of the coarse-grained packages described previously (*Section 2.5.2.*: *Architectural Element VIII: Point Bar 4*). In these examples, southward-dipping IHS deposits are truncated and overlain by sandstone packages approximately 5 – 15 m above base M2.5 (Figs. 2.11, 2.12).

The McMurray Formation is often characterized by stacked channel-belt deposits with multiple upward fining intervals (Fig. 2.2A; Hein and Cotterill, 2006; Chen et al., 2022; Peng et al., 2024). With only localized subsurface data the base of the coarsening upward FA1 deposits of AEVIII could be interpreted as the base of M3 as illustrated in "Pick 1" in E-E' (Fig. 2.9), representing the boundary between two genetically unrelated point bars within the same channel-belt, or a separate channel-belt altogether (e.g., Li et al., 2010; Chen et al., 2022). However, lateral exposure in outcrop shows that deposits above and below "Pick 1" belong to the same point bar, as illustrated by the relative age delineations in the sandstone packages shown in Figures 2.11C and 2.12C. Sandstone bedsets dip laterally until amalgamating with basal M2.5 sandstone packages of AEVIII (Fig. 2.10, NECOP, 600 – 700 m; Figs 2.11C, 2.12C). In some cases, IHS bedding is deposited above "Pick 1", forming interfingered sandstone and IHS packages (e.g., Choi et al., 2004; Fig. 2.10, NECOP, 480 – 500 m).

In Figures 2.11 and 2.12 the major erosional surfaces at the base of the coarse-grained packages (Figs. 2.11C, 2.12C) represent intra-point-bar erosional surfaces (e.g., Durkin et al., 2015) during bar re-orientation in AEVIII. Although coarsening upward deposits are not commonly shown in point-bar models, they have been previously documented (e.g., Jackson, 1976; Dietrich and Whiting, 1989; Frothingham and Rhoads, 2003; Willis and Tang, 2010), and interpreted as coarse-grained bedload sediment that is dispersed across the point-bar surface when maximum flow shear shifts towards the inner bank (Ghinassi et al., 2016). This process is interpreted in AEVIII when the location of maximum erosion shifts downstream in phase 2, stages 2 – 4 (Fig. 2.17B), and the adjusted trajectory of downstream erosion was such that point-bar material deposited on the downstream bar (FA2) is subsequently eroded on the inner, upstream bank of the same point bar.

3-D models of channel belt deposits often utilize major stratigraphic boundaries as the framework for lithofacies distributions. It is important to delineate the potential for localized upper intra-point-bar erosional surfaces, as described above, from diachronous channel-belt deposit boundaries. The quality of outcrop plays a significant role in the recognition of these potential errors. Based on outcrop evidence, "Pick 2" (Fig. 2.7) addresses this characterization to delineate M2.5 from M3. From a modelling perspective, the 4 – 6 m difference in "Pick 1" and "Pick 2" would potentially result in incorrect lateral extrapolation of predicted ore volume in the area. Careful investigation of dip-meter readings, including preferred dip orientations above and below localized upper-point-bar scour surfaces, could aid in minimizing erroneous stratigraphic picks.

2.6.1.2.Unorganized IHS and mudstone-clast breccia

In the southwestern portion of AEVIII, mudstone clast breccia and unorganized, discontinuous IHS represent atypical point-bar facies associations (FA5; Fig. 2.6) that are not characterized by upward-fining nor conform to typical downstream-fining trends. Pervasive mudstone within clasts and overlying IHS are, on average, finer-grained than the downstream IHS deposits to the east (FA1 and FA2), resulting in atypical downstream coarsening trends in gamma-log responses (Figs. 2.6, 2.9, F-F', G-G'). Furthermore, IHS in FA5 outcrop does not always comprise laterally continuous or planar bedding (e.g., Fig. 2.10, NECOP, 920 – 1215 m; Figs. 2.5, 2.13, 2.14) that is typified in other point-bar deposits in this study (e.g., AEI, Figs. 2.8A, 2.8B; AEVIII, Figs. 2.11, 2.12, 2.15; Fig. 2.10, NECOP, 1250 – 1600 m) and elsewhere (Mossop and Flach, 1983; Jablonski and Dalrymple, 2016; Chen et al., 2022; Hayes et al., 2023).

The upper intervals of FA5 comprise mudstone interbeds that line compound trough-shaped scours (Figs. 2.5, 2.14F). This is not a well-documented feature in point-bar deposits. In

well-log data, these intervals (Fig. 2.9, F-F', G-G') are interpreted as IHS bedding (F3 – F5) because they appear as interbedded sandstone and mudstone in core and gamma-ray logs and sometimes display organized dipping planes in well-logs. Adjacent wells, however, often comprise different dip-meter character (e.g., Fig. 2.9, F-F', G'G'). Dip-meter showing over-steepened dip angles (> 15°) are likely due to the steep, trough-lined structure of the interbeds observed in outcrop (Figs. 2.5, 2.14F). The presence of mudstone interbeds within compound trough-shaped bedding surfaces is paradoxical, as it indicates both high energy structure via bedload transportation (Miall, 1981; Collinson and Mountney, 2019) with lower energy processes like sediment suspension fallout in quiescent conditions (Thomas et al., 1987; Jablonski and Dalrymple, 2016). The enigmatic FA5 deposits, along with sharp-based upward coarsening deposits in the previous section, are better understood when the context of paleochannel evolution and morphodynamic channel processes are examined using 3-D planform reconstruction of the area of interest.

2.6.2. Planform reconstruction and paleochannel evolution

Reconstructing paleochannel evolution has been utilized to illustrate the variations in depositional processes, thus addressing the complex heterogeneity of most channel-belts. This includes 3-D seismic surveys that capture acoustic impedance contrasts in point-bar IHS and abandoned-channel deposits (Hubbard et al., 2011; Smith et al., 2011; Durkin et al., 2017), investigating outcrops with measurable paleoflow and bedding accretion directions (Durkin et al., 2015; Viseras et al., 2018; Mayo et al., 2023), and borehole data to interpret lithological and structural features (Smith et al., 2009; Shan et al., 2018). These data produce the framework that broadly defines paleochannel positioning over time and can be presented as planform channel-belt reconstruction (e.g., Fig. 2.17). The validity of planform reconstruction of ancient deposits

can be tested and refined using satellite imagery on vast networks of channel belts deposits on the surface of Earth (Smith et al., 2009; Sylvester et al., 2020).

The linkages between modern channel-belt imaging and ancient point bars provides a direct comparison of meander-belt processes and their depositional products (e.g., Durkin et al., 2020b; Yan et al., 2024). Therefore, reconstructing the stages of channel evolution is an objective modelling strategy that can be combined with empirical subsurface data (i.e., borehole data). To investigate the newly documented atypical point-bar deposits of FA5, the environmental context and channel evolution over time are evaluated using the planform reconstruction in Figure 2.17.

Based on concurrence of events in the paleochannel revealed by the planform reconstruction, initial interpretation suggests that the morphodynamic changes during phase 2, stages 2 and 3 contributed to deposition of FA5 in phase 2, stages 4 and 5 (Fig. 2.17B). In stage 2 the active cutbank encounters the abandoned-channel fill of AEIII (Fig. 2.17B), comprising approximately 20-meters of continuous mudstone-rich material (Fig. 2.7, B-B'; Fig. 2.8D). The paleochannel responds by shifting cutbank erosion downstream to the east (Fig. 2.17B, stages 2 – 3), coinciding with initial FA5 sedimentation approximately 300 – 500 m downstream in phase 2, stages 3 (Fig. 2.17B). When the cutbank clears the abandoned-channel fill material in stage 5 (Fig. 2.17B), FA5 deposition is replaced by FA2 shortly before eventual abandonment in stages 5 and 6 (Fig. 2.17B). The FA5 to FA2 transitions is observed in outcrop in Figure 2.14D, E and F (FA5) to Figure 2.14C (FA2). These observations indicate that the mudstone-rich cutbank material and resulting morphodynamic channel adjustments likely had an impact on the atypical FA5 deposits in AEVIII.

The spectrum of mudstone-clast sizes, their deposit structures, and clast-size trends in FA5 contain critical information that help to better characterize the pervasiveness of mudstone

clasts in FA5. In FA5 deposits clasts are sand- to boulder-sized, lining trough cross-bedding foresets and bottomsets (Figs. 2.5, 2.10, NECOP, 890 – 1110 m; Figs. 2.13, 2.14D – 2.14F). Towards the eastern margin and downstream from FA5, mudstone clast sizes transition to sand- to pebble-sized and are observed lining IHS bedding surfaces (Fig. 2.10, NECOP, 1185 – 1295 m; Figs. 15A, 15B). The gradual transition in mudstone clast sizes (i.e., coarse- to fine-grained) and deposit structure (i.e., clasts lining foresets and bottomsets to clasts lining IHS bedding) indicates a range of depositional conditions; spanning from high energy clast deposition in trough cross-bedding in the lower 10 meter interval of the upstream point-bar section (FA5; Figs. 2.13, 2.14), to the downstream, lower energy clast deposition within planar IHS bedding (FA2; Fig. 2.15B). The downstream clast grain-size fining adheres to point-bar trends (e.g., Jackson, 1976; Labrecque et al., 2011; Hagstrom et al., 2018; Bellizia et al., 2021), although documentation of such trends is often focused on sand and silt grains.

In addition to downstream fining trends, lateral channel grain sorting also occurs in meandering river channels (Dietrich and Whiting, 1989). Lateral bedload movement is controlled by cross-stream shear and channel bed topography (Dietrich and whiting, 1989; Ghinassi et al., 2016) where the coarsest grains are more susceptible to gravity and move downslope towards the thalweg, or the zone of highest shear; while smaller grains are preferentially transported laterally, up the point-bar slope in accordance with secondary helical flow that is forced upward from the cutbank/ thalweg to the point-bar surface (Termini and Piraino, 2010; Ghinassi et al., 2016). If mudstone clasts are impacted by hydrodynamic fields as demonstrated in the downstream transition of the mudstone clast breccia properties presented above (e.g., Figs. 2.13A, 2.13B, 2.14E), they should also adhere to both upward and lateral hydraulic sorting trends that impact sand and silt grains near the bar apex.

Outside of the present study, mudstone clast breccia descriptions are often associated with massive structures (e.g., Labrecque et al., 2011; Musial et al., 2012; Horner et al., 2019), which are interpreted as rapid sedimentation with no significant mudstone clast sorting. These generalizations can be attributed to the lack of relevant data for structure recognition in grains larger than sand-sized. Unorganized dip-meter responses, lateral confinement of cored samples, and a lack of laterally continuous and/ or fresh outcrop exposures to properly examine mudstone clast breccia structures limits interpretations. In the present study mudstone clast breccia with trough cross-bedding structure are common and indicate that mudstone clasts (i.e., mudstone aggregates) likely were a portion of the bedload material (e.g., Pavan et al., 2019), perhaps behaving similarly to saltating sand grains in channel-bottom and lower bar dunes (e.g., Coleman and Nikora, 2011; Charru et al., 2013), and similar to sand and silt migration within current ripples on point-bar surfaces (e.g., Plint, 1983; Hagstrom et al., 2018).

The pervasive mudstone clasts in FA5 are interpreted to be eroded remnants of the mudstone-rich channel fill of AEIII, taken from the upstream cutbank and deposited slightly downstream on the point bar surface (Fig. 2.18). The interpreted sequence of events are 1) Erosion of the mudstone-rich cutbank starting in phase 2, stage 1, and continuing until stage 5. Gradual undercutting of the bank supplies the channel with continuous entrainment of small rip-up clasts (Forst, 2019; e.g., Fig. 2.18, T_1, X-X'; T_2, Y-Y'). The entrained fines adhere to secondary helical flow and accumulate on the point bar on the inside of the bend (Forst, 2019; e.g., Fig. 2.18, T_1, Y-Y', Z-Z'; T_2, Z-Z'). 2) Eventually bank undercutting causes bank block collapse, resulting in an avalanche of large mudstone blocks falling into the channel and accumulating at the bank toe where maximum boundary shear stress causes elevated velocity and turbulence (Thorne and Lewin, 1982; Jablonski, 2012; Broughton, 2018; Chen et al., 2022; e.g.,

Fig. 2.18, T_2, X-X'; T_3, Y-Y'). 3) Consequently, the collapsed blocks are reworked and winnowed (Kleinhans, 2010; Forst, 2019), eventually fracturing into mud clasts small enough to be removed from the toe and transported downstream as bedload along the maximum shear path (i.e., along the channel thalweg; Kleinhans, 2010; Hubbard et al., 2011; Labrecque et al., 2011; Broughton, 2018; e.g., Fig. 2.18, T_2, X-X' to Y-Y'; T_3, Y-Y' to Z-Z'; T_4, Z-Z'). Although helical flow is not strong enough to carry coarse sediment across the thalweg (Friedkin, 1945), upon further fracturing, smaller grains (i.e., smaller mud clasts) may overcome gravity to exit the thalweg through entrainment and follow secondary helical currents laterally and up the point-bar surface (Ghinassi et al., 2016; Forst, 2019; Kim et al., 2020; e.g., Fig. 2.18, T_2, Y-Y' to Z-Z'; T_3, Y-Y' to Z-Z'; T_4, Y-Y' to Z-Z'), on inner bank of the point bar (Dietrich and Whiting, 1989). Meanwhile the remaining larger clasts stay in the thalweg, enduring further dissociation due to grain collisions (e.g., McEwan et al., 1999) and high flow shear (Dietrich and Whiting, 1989; Frothingham and Rhoads, 2003; Fig. 2.18, $T_2 - T_4$). The simultaneous downstream transportation, clast dissociation, and lateral grain sorting act in unison to form a continuous source of smaller mudstone clasts that are susceptible to entrainment and lateral transportation via secondary helical flow. Therefore, these processes enable continuous mudstone clast deposition, as observed in the lateral and vertical continuity of mudstone clast pervasion throughout the bottom intervals of FA5, deposited during phase 2, stages 3 – 5 (Fig. 2.17B), on the lower- to mid-point-bar surface of AEVIII (Figs. 2.5, 2.13A, 12.3B, 2.14E, 2.14F, 2.18, T_4, Z-Z').

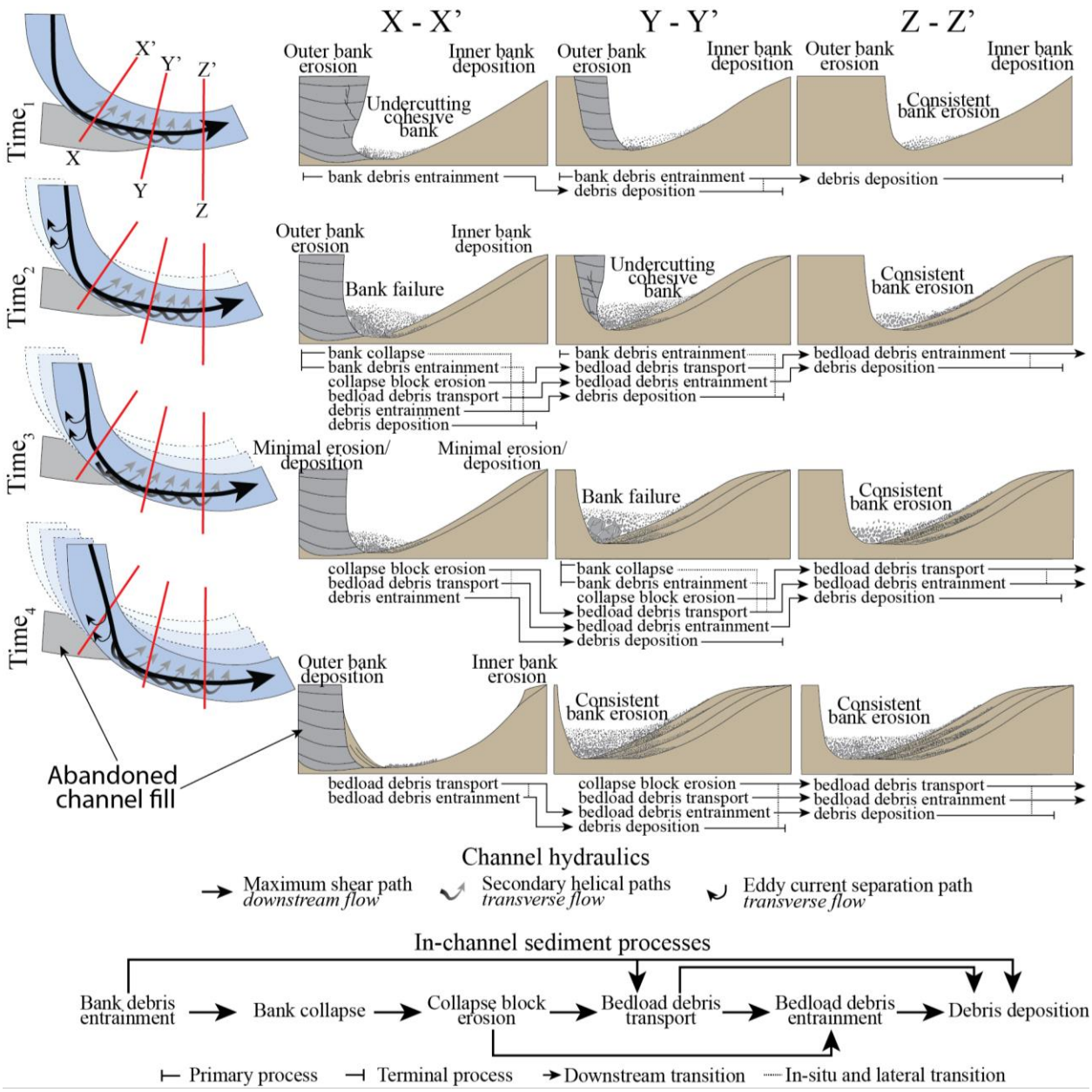

Figure 2. 18 Illustration of depositional processes involved in FA5. Cross sections show downstream processes and deposits from X-X', Y-Y' and Z-Z'. The four rows represent time from T_1 (top) to T_4 (bottom). Six in-channel depositional processes are shown (bank debris entrainment, bank collapse, collapse block erosion, bedload debris transport, bedload debris entrainment, debris deposition) as primary, terminal or transitional processes that evolve laterally or downstream.

The above interpretation addresses the presence of mudstone breccia in FA5, however, the overlying atypical wavy mudstone-sandstone interbeds and large (boulder-sized) mudstone clasts in the mid- to upper-point-bar surface of AEVIII are also enigmatic. The sharp angularity and boulder-size of the mudstone clasts (Figs. 2.5, 2.13C, 2.13D, 2.14F) indicate that they were probably transported a very short distance (Hubbard et al., 2010; Broughton, 2018), in some cases sliding only meters away from their mudstone bedding source on the point-bar surface (e.g., Figs. 2.13C, 2.13D). A result of post-depositional erosion of mudstone-rich IHS. However, mudstone-rich IHS bedding is not common on upstream to central bar deposits (Ghinassi et al., 2016), as observed in AEVIII. In this study it is hypothesized that the lateral mudstone clast sorting mechanisms discussed above extends into sand- and silt-sized mudstone aggregates that travel further up the point-bar surface, contributing to upper-bar IHS (Fig 2.18). The trough-lined mudstone bedding structures in Figure 2.5 and Figure 2.14F indicate that some mudstone-sandstone interbeds in FA5 were deposited in higher energy regimes, and, perhaps, with mudstone aggregates that travelled as bedload material (e.g., Kavan, 2019). The resulting mudstone microstructure, however, is obscured by post-depositional compaction that hides the potential presence of visible mudstone aggregates in homogenous mudstone deposits (Aplin and Macquaker, 2011; Laycock et al., 2017), and further evaluation of mudstone samples would be needed to test this hypothesis.

FA5 has been termed atypical and, with the aid of planform reconstruction, the processes involved in FA5 deposition have been interpreted. The spatial context of planform reconstruction suggests that the processes involved in FA5 deposition may be common in meander-belts. Downstream translation, influenced by the presence of a poorly erodible cutbank material, is a common occurrence in meander-belts within low accommodation settings (Smith et al., 2009;

Ghinassi et al., 2016). The subsequent preservation of FA5, as seen in the area of interest, however, is rare. The cutbank in a downstream translating point bar is directed at the downstream bar, therefore, these deposits are often eroded shortly after deposition unless interrupted by upstream channel avulsion (Jackson, 1976; Willis and Tang, 2010, Ghinassi and Ielpi, 2015). Upstream point-bar deposits comprise the coarsest material in the point bar and either coarsen upwards or show no gradational fining trends (Jackson, 1976; Frothingham and Rhoads, 2003; Willis and Tang, 2010; Ghinassi et al., 2016), as observed in upstream deposits of AEVIII. In response to above-mean discharge, water flows over the point-bar surface and truncates upper-bar deposits, dispersing coarse-grained sediment across the upstream section of the point bar (Bluck, 1971). The sharp-based, upward coarsening deposits observed north of FA5 are evident of this process (Figs. 2.11, 2.12). It is interpreted that FA5 was deposited in high energy conditions on the upstream to central portion of the point bar in AEVIII, and preservation occurred due to upstream avulsion of the paleochannel in phase 2, stage 6 (Fig. 2.17).

2.7. Conclusion

Subsurface data is often utilized to create comprehensive models, interpret sedimentary characteristics (e.g., subsurface flow pathways, aquifers) and characterize ore potential. It is not often that these data sets are complimented by outcropping units from which they penetrate. The integration of dense borehole data with mine-face photography allows for exceptional linkages between conventional 1-D data and outcrop-scale architectural data. To improve understanding ancient meandering river processes, both types of data are utilized to reconstruct channel-belt deposits in 3-D, interpret the meander-belt evolution over time and subsequently establish the linkages between fluvial processes and the resulting deposits.

A framework for planform reconstruction was created by distributing facies associations and, where present, paleoflow indicators and bar accretion directions to each well in the area of interest. The approach resulted in the recognition of nine architectural elements: four point bars, three counter-point bars and two abandoned-channel fills. Based on cross cutting relationships and a major erosional boundary, the area of interest was separated into two distinct depositional phases, each with six stages of meander-belt evolution.

Phase 1 deposits comprised a point bar and counter-point bar that migrated northwest, increasing in curvature until neck cut-off resulted in an abandoned-channel fill. The paleochannel subsequently continued migrating west while depositing a second point bar and counter-point bar set. Deposits in phase one aligned with typical point-bar trends including upward fining, downstream fining and fining with increase channel sinuosity. These trends are observed in both outcrop and borehole data. The results strengthen the validity of these trends and the interpretive capabilities when predictive practices are employed.

Phase 2 comprised southward migrating bedforms, primarily a large point bar with low channel sinuosity. The point bar is characterized by atypical facies and grain-size trends including no upward fining and no fining downstream from the bend apex. The atypical deposits were heterolithic, containing ubiquitous mudstone clasts interspersed with discontinuous IHS and trough cross-bedded sandstone. Furthermore, IHS character in well-log, particularly bedding dip directions, were not consistent between wells and with adjacent point-bar deposits. A notable outcrop observation was that on average, IHS bedding consistently dipped in similar directions of adjacent point-bar deposits. This, however, was not reflected in well logs due to pervasive scour surfaces, discontinuous interbeds and the presence of mudstone-lined trough cross-bedding. Downstream and to the east of the atypical deposits, mudstone clast breccias and clast

sizes decreased, bedding plane continuity increased and the sandstone to mudstone ratio increased.

Atypical deposits challenge interpretations of typical 1-D borehole data and increase potential errors in modelling techniques. To optimize predictive methods, it is critical to document and develop understanding for atypical deposits. The deposits in phase two are characterized by high energy structures (i.e., scour surfaces, trough cross-bedding, discontinuous bedding) with lithologies suggesting drastic energy fluctuations (i.e., large mudstone clasts, sandstone and mudstone beds). The cutbank upstream of atypical deposits in phase two encountered the mudstone-rich abandoned-channel fill of phase 1. The meander bend responded accordingly by migrating downstream, adjacent to the resistant substrate, and promoting counter point-bar deposition. The partial erosion of the abandoned-channel fill is interpreted to supply the mudstone sediment for breccia deposits on the adjacent point bar. This process explains the presence of ubiquitous mudstone clasts in the atypical deposits; however, it does not explain the mudstone bedding distributed in structures normally attributed to higher energy. A possible explanation is expanded upon using the presence of graded mudstone clasts that are organized in foreset and bottomset bedding and decrease in size and abundance downstream. Mudstone clast grain-size sorting suggests that clasts behave in a similar manner to sand-grains, whereas mudstone clasts potentially travel as bedload material and are hydrodynamically sorted. Unlike sand grains, mudstone clasts may continually disaggregate while travelling downstream, away from the original mudstone source. The character of mudstone clasts and their relationship with IHS is further investigated in Chapter 3 using mudstone samples collected downstream from the atypical point-bar deposits herein.

2.8. References

Ahmad, W., Gingras, M.K., (2022). Ichnology and sedimentology of the lower Cretaceous Wabiskaw Member (Clearwater Formation) Alberta, Canada. Marine and Petroleum Geology. 143(2022), 105775.

Allen, J.R.L., (1965). Fining-upwards cycles in alluvial successions. Geological Journal. 4(3), 229-246.

Aplin, A.C., Macquaker, J.H.S., (2011). Mudstone diversity: Origin and implications for source, seal, and reservoir properties in petroleum systems. American Association of Petroleum Geologists Bulletin. 95(12), 2031-2059.

Barton, M.D., (2016). The architecture and variability of valley-fill deposits within the Cretaceous McMurray Formation, Shell Albian Sands Lease, northeast Alberta. Bulletin Canadian Petroleum Geology. 64(2), 166-198.

Bell, J.S., Price, P.R., McLellan, P.J., (1994). In-situ stress in the Western Canada Sedimentary Basin. In Mossop, G. D., Shetsen, I., (eds), Geological atlas of the Western Canada sedimentary basin. Canadian Society of Petroleum Geologists and Alberta Research Council, 439-446.

Bellizia, E., Boaga, J., Fontana, A., D'Alpaos, A., Cassiani, G., Ghinassi, M., (2021). Impact of genesis and abandonment processes of a fluvial meander on geometry and grain-size distribution of the associated point bar (Venetian Plain, Italy). Marine and Petroleum Geology. 127(2021), 104951.

Benyon, C., Leier, A., Leckie, D.A., Webb, A., Hubbard, S.M., Gehrels, G., (2014). Provenance of the Cretaceous Athabasca oil sands, Canada: Implications for continental-scale sediment transport. Journal of Sedimentary Research. 84(2), 136-143.

Bluck, B.J., (1971). Sedimentation in the meandering River Endrick. Scottish Journal of Geology. 7, 93-138.

Brekke, H., MacEachern, J.A., Roenitz, T., Dashtgard, S.E., (2017). The use of microresistivity images logs for facies interpretations: An example in point bar deposits of the McMurray Formation, Alberta, Canada. American Association of Petroleum Geologists Bulletin. 101 (5), 655-682.

Bridge, J. S., Alexander, J., Collier, R. E. L., Gawthorpe, R. L., Jarvis, J., (1995). Ground-penetrating radar and coring used to study the large-scale structure of point bar deposits in three dimensions. Sedimentology. 42, 839-852.

Broughton, P.L., (2015). Syndepositional architecture of the northern Athabasca oil sands deposit, northeastern Alberta. Canadian Journal of Earth Sciences. 52(1), 21-50.

Broughton, P.L., (2018). Mudstone clast breccia in the Cretaceous Athabasca Oil Sands, western Canada: Fluvial debris-flow transitions into traction carpets. The Journal of Geology. 126, 63-97.

Burge, L.M., Smith, D.G., (1999). Confined meandering river eddy accretions: sedimentology, channel geometry and depositional processes. In Smith, N.D., Rogers, J., (Eds), Fluvial Sedimentology VI, International Association of Sedimentologists, Special Publication 28, 113-130.

Bzdziuch, D., (2023). Forecasting shape and length of IHS mudstone beds in the middle McMurray Formation, Fort Hills mine, AB, Canada. Bulletin of Canadian energy geoscience. 70(1), 1-19.

Carrigy, M.A., (1959). Geology of the McMurray Formation, Part 3: General Geology of the McMurray Area. Research Council of Alberta. Geological Division, Edmonton, AB.

Charru, F., Andreotti, B., Claudin, P., (2012). Sand ripples and dunes. Annual Reviews of Fluid Mechanics. 45, 469-493.

Chateau, C.C.F., Dashtgard, S.E., MacEachern, J.A., Hauck, T.E., (2019). Syndepositional carbonate epikarstification and consequence for overlying parasequence architecture in a low-accommodation setting in the McMurray Formation of Alberta, Canada. Marine and Petroleum Geology. 104, 168-179.

Chen, Q., Shchepetkina, A., Melnyk, S., Gingras, M.K., (2022). Integrating facies analysis with dipmeter data to characterize point bars of the Lower Cretaceous McMurray Formation, Christine River, AB, Canada. Marine and Petroleum Geology. 136, 105449.

Choi, K.S., Dalrymple, R.W., Chun, S.S., Kim, S., (2004). Sedimentology of modern, inclined heterolithic stratification (IHS) in the macrotidal Han River delta, Korea. Journal of Sedimentary Research. 74(5), 677-689.

Clift, P.D., Olson, E.D., Lechons, A., Grace Moran, M., Barbato, A., Lorenzo, J.M., (2019). Grain-size variability within a mega-scale point bar system, False River Louisiana. Sedimentology. 66(2), 408-434

Coleman, S.E., Nikora, V.I., (2011). Fluvial dunes: initiation, characterization, flow structure. Earth Surfaces Processes and Landforms. 36, 39-57.

Collinson, J., Mountney, N., (2019). Sedimentary Structures. 4th edition. Dunedin Academic Press, Edingburg.

Crerar, E.E., Arnott, R.W.C., (2007). Facies distribution and stratigraphic architecture of the Lower Cretaceous McMurray Formation, Lewis property, northeastern Alberta. Bulletin Canadian Petroleum Geology. 55(2), 99-124.

Dietrich, W.E., Whiting, P., (1989). Boundary shear stress and sediment transport in river meanders of sand and gravel. *In* Ikeda, S., Parker, G., (eds), River Meandering. Water Resources Monograph 12, American Geophysical Union, U.S.A.

Durkin, P.R., Boyd, R.L., Hubbard, S.M., Shultz, A.W., Blum, M.D., (2017). Three-dimensional reconstruction of meander-belt evolution, Cretaceous McMurray Formation, Alberta foreland basin, Canada. Journal of Sedimentary Research. 87(10), 1075-1099.

Durkin, P.R., Hubbard, S.M., Boyd, R.L., Leckie, D.A., (2015). Stratigraphic expression of intra-point bar erosion and rotation. Journal of Sedimentary Research. 85(10), 1238-1257.

Durkin, P.R., Hubbard, S.M., Smith, D.G., Leckie, D.A., (2018). Predicting heterogeneity in meandering fluvial and tidal-fluvial deposits. In Ghinassi, M., Colombera, L., Mountney, N.P., Reesink, A.J.H., Bateman, M. (eds), Fluvial Meanders and Their Sedimentary Products in the Rock Record. International Association of Sedimentologists, 231-249.

Durkin, P.R., Horner, S.C., Hagstrom, C.A., (2020a). Comment on "Using a modern analogue to interpret depositional position in ancient fluvial-tidal channels: Examples from the McMurray Formation, Canada" by Andrew D. La Croix, Shahin E. Dashtgard, James A. MacEachern, Geoscience Frontiers, Volume 10, Issue 6, Pages 2219-2238. Geoscience Frontiers. 11, 1081-1086.

Durkin, P.R., Hubbard, S.M., Holbrook, J., Weleschuck, Z., Nesbit, P., Hugenholtz, C., Lyons, T. and Smith, D.G., (2020b). Recognizing the product of concave-bank sedimentary processes in fluvial meander belts. Sedimentology, 67, p. 2819-2849,

Flach, P.D., Mossop, G.D., (1985). Depositional environments of Lower Cretaceous McMurray Formation, Athabasca Oil Sands, Alberta. American Association of Petroleum Geologists Bulletin. 69(8), 1195-1207.

Forst, M.P., (2019). Effects of flow dynamics on bank erosion in consecutive meander bends. Doctoral theses at NTNU, 2019: 152.

Friedkin, J., (1945). A Laboratory Study of the Meandering of Alluvial Rivers, Technical Report, May 1945. U.S. Army Corps of Engineers Waterworks Experimental Station: Vicksburg, MI.

Frothingham, K.M., Rhoads, B.L., (2003). Three-dimensional flow structure and channel change in an asymmetrical compound meander loop, Embarras River, Illinois. Earth Surfaces Processes and Landforms. 28, 625-644.

Ghinassi, M., Nemec, W., Aldinucci, M., Nehybra, S., Ozaksoy, V., Fidolini, F., (2014). Plan-form evolution of ancient meandering rivers reconstructed from longitudinal outcrop sections. Sedimentology. 61, 952-977.

Ghinassi, M., Ielpi, A., (2015). Stratal architecture and morphodynamics of downstream-migrating fluvial point bars (Jurassic Scalby Formation, U.K.). Jounral of Sedimentary Research. 85, 1123-1137.

Ghinassi, M., Ielpi, A., Aldinucci, M., Fustic, M., (2016). Downstream-migrating fluvial point bars in the rock record. Sedimentary geology. 334(2016), 66-96.

Hagstrom, C. A., Hubbard, S. M., Horner, S. C., Martin, H. K., Peng, Y., (2023). Comparison of the morphology, facies, and reservoir quality of valley fills in the southern Athabasca Oil Sands Region, Albert, Canada. Association of America petroleum geologist bulletin. 107(4), 553-591.

Hagstrom, C.A., Hubbard, S.M., Leckie, D.A., Durkin, P.R., (2019). The effects of accretion-package geometry on lithofacies distribution in point bar deposits. Journal of Sedimentary Research. 89, 381-398.

Hayes, D.A., Botterill, S.E., Ranger, M.J., Gingras, M.K., (2023). Fluvial character and architecture of an outcrop using sedimentology combined with UAV-based modelling, Cretaceous McMurray Formation, NE Alberta, Canada. Journal of Sedimentary Research. 93, 273-292.

Hein, F.J., Cotterill, D.K., (2006). The Athabasca Oil Sands – A regional geological perspective, Fort McMurray area, Alberta, Canada. Natural Resources Research. 15, 85-102.

Horner, S.C., Hubbard, S.M., Martin, H.K., Hagstrom, C.A., (2019). Reconstructing basin-scale drainage dynamics with regional subsurface mapping and channel-bar scaling, Aptian Western Canada Foreland Basin. Sedimentary Geology. 385 (1), 26-44.

Hubbard S.M., Smith, D.G., Nielsen, H., Leckie, D.A., Fustic, M.A., Spencer, R.J., Bloom, L., (2011). Seismic geomorphology and sedimentology of a tidally influenced river deposit, Lower Cretaceous Athabasca oil sands, Alberta, Canada. American Association of Petroleum Geologists Bulletin, 95 (7), 1123-1145.

Ielpi, A., Ghinassi, M., (2014). Planform architecture, stratigraphy signature and morphodynamics of an exhumed Jurassic meander plain (Scalby Formation, Yorkshire, UK). Sedimentology. 61, 1923-1960.

Jablonski, B.V.J., (2012). Process sedimentology and three-dimensional facies architecture of a fluvially dominated, tidally influenced point bar: middle McMurray Formation, lower Steepbank River area, northeastern Alberta, Canada. MSc Thesis. Queen's University.

Jablonski, B.V.J., Dalrymple, R.W., (2016). Recognition of strong seasonality and climatic cyclicity in an ancient fluvially dominated, tidally influenced point bar: Middle McMurray Formation, Lower Steepbank River, northeastern Alberta, Canada. Sedimentology. 63(3), 552-585.

Jackson, R.G., (1976). Depositional model of point bars in the lower Wabash River. Journal of Sedimentary Petrology. 46(3), 579-594.

Kim, J.S., Seo, I.W., Baek, D., Kang, P.K., (2020). Recirculating flow-induced anomalous transport in meandering open-channel flows. Advances in Water Resources. 141, 103603.

Kleinhans, M.G., (2010). Sorting out river channel patterns. Progress in Physical Geography. 34(3), 287-326.

Labrecque, P.A., Jensen, J.L., Hubbard, S.M., (2011). Cyclicity in Lower Cretaceous point bar deposits with implications for reservoir characterization, Athabasca Oil Sands, Alberta, Canada. Sedimentary Geology. 242(1-4), 18-33.

Lamb, M.P., Leeuw, J.D., Fischer, W.W., Moodie, A.J., Venditti, J.G., Nittrouer, J.A., Haught, D., Parker, G., (2020). Mud in rivers transported as flocculated and suspended bed material. Nature Geoscience. 13, 566-570.

Laycock, D.P., Pederson, P.K., Montgomery, B.C., Spencer, R.J., (2017). Identification, characterization, and statistical analysis of mudstone aggregate clasts, Cretaceous Carlile Formation, Central Alberta, Canada. Marine and Petroleum Geology. 84, 49-63.

Leckie, D. A., Smith, D. G., (1992). Regional setting, evolution, and depositional cycles of the Western Canada Foreland Basin. In Macqueen, R. W., Leckie, D. A., (eds), Foreland Basins and Folded Belts. American association of petroleum geologist. AAPG Memoir 55, 9-46.

Leeder, M.R., Bridges, P.H., (1975). Flow separation in meander bends. Nature. 253(5490), 339-339.

Leopold, L. B., Wolman, M. G., (1960). River Meanders. Bulletin of the geological society of America. 71, 769-794.

Li, W., Bhattacharya, J.P., Campbell, C., (2010). Temporal evolution of fluvial style in a compound incised-valley fill, Ferron “Notom Delta”, Henry Mountains Region, Utah (U.S.A.). Journal of Sedimentary Research. 80(6), 529-549.

Martinius, A.W., Fustic, M., Garner, D.L., Jablonski, B.V.J., Strobl, R.S., MacEachern, J.A., Dashtgard, S.E., (2017). Reservoir characterization and multiscale heterogeneity modelling of inclined heterolithic strata for bitumen-production forecasting, McMurray Formation, Corner, Alberta, Canada. Marine and Petroleum Geology. 82, 336-361.

Mayo, K., Silva, R. L., Durkin, P. R., (2023). Paleoenvironmental reconstruction of Late Cretaceous rivers, Dinosaur Park Formation, Alberta, Canada. Sedimentary geology. 457(2023), 106499.

McEwan, I.K., Jefcoate, B.J., Willetts, B.B., (1999). The grain-fluid interaction as a self-stabilizing mechanism in fluvial bed load transport. Sedimentology. 46, 407-416.

McPhee, D. A., Wightman, D. M., (1991). Timing and the dissolution of Middle Devonian Elk Point Group evaporites — Townships 47 to 103 and ranges 15 W3M to 20 W4M. Bulletin of Canadian petroleum geology. 39(2), 218.

Miall, A.D., (1981). Analysis of Fluvial Depositional Systems. American Association of Petroleum Geologists Continuing Studies 20.

Milne, J.A., (1982). Bed-material size and the riffle-pool sequence. Sedimentology. 29, 267-278.

Mossop, G.D., Flach, P.D., (1983). Deep channel sedimentation in the Lower Cretaceous McMurray Formation, Athabasca Oil Sands, Alberta. Sedimentology. 30(4), 493-509.

Mossop, H.D., Shetsen, I., (1994). Geological atlas of the Western Canada Sedimentary Basin. Canadian Society of Petroleum Geologists and Alberta Research Council.

Musial, G., Reynaud, J.Y., Gingras, M.K., Fenies, H., Labourdette, R., Parize, O., (2012). Subsurface and outcrop characterization of large tidally influenced point bars of the Cretaceous McMurray Formation (Alberta, Canada). Sedimentary geology. 279, 156-172.

Nanson, G.C., (1980). Point bar and floodplain formation of the meander Beatton River, northeastern British Columbia, Canada. Sedimentology. 27, 3-29.

Nardin, T.R., Feldman, H.R., Carter, B.J., (2013). Stratigraphic architecture of a large-scale point bar complex in the McMurray Formation: Syncrude's Mildred Lake Mine, Alberta, Canada, In Hein, F.J., Leckie, D., Larter, S., Suter, J.R., (eds), Heavy-Oil and Oil-Sand Petroleum Systems and Beyond, AAPG Studies in Geology 64, pp. 273-311.

Page, K., Nanson, G., (1982). Concave-bank benches and associated floodplain formation. Earth Surfaces Processes and Landforms. 7(6), 529-543.

Pavan, K., (2019). Microfacies analysis of mudstone in a freshwater to marine transect: Upper Cretaceous Dunvegan and Kaskapau formations, Western Canada Foreland Basin. Electronic Thesis and Dissertation Repository. 6528.

Peng, Y., Durkin, P.R., Martin, H.K., Leckie, D.A., Horner, S.C., Hubbard, S.M., (2024). Early Cretaceous evolution of the McMurray Formation: A review toward a better understanding of the paleo-depositional system. Earth-Science Reviews. 252(2024), 104740.

Plint, A.G., (1983). Sandy fluvial point bar sediments from the Middle Eocene of Dorset, England. *In* Collinson, J.D., Lewin, J. (eds), Modern and Ancient Fluvial Systems. International Association of Sedimentologists. 6, 355-368.

Ranger, M.J., Pemberton, S.G., (1992). The sedimentology and ichnology of the estuarine point bars in the McMurray Formation of the Athabasca Oil Sands deposits, northeastern Alberta, Canada, in Pemberton, S.G., (ed), Applications of Ichnology to Petroleum Exploration: A Core Workshop, Society of Economic Paleontologists and Mineralogists Core Workshop 17, pp. 401-421.

Rinke-Hardekopf, L., Dashtgard, S.E., MacEachern, J.A., Gingras, M.K., (2022). Resolving stratigraphic architecture and constraining ages of paralic strata in a low-accommodation setting, Firebag tributary, McMurray Formation, Canada. The Depositional Record. 8, 754-785.

Shan, J., Lin, Z., Chen, L., Zhang, B., Fang, S., Yan, X., Fang, W., Xie, L., Liu, B., Zhang, L., (2018). Reconstruction of meandering paleo-channels using dense well data, Daqing Oil Field, Songliao Basin, China. Petroleum Science. 15, 722-743.

Smith, D.G., Hubbard, S.M., Leckie, D.A., Fustic, M., (2009). Counter point bar deposits: lithofacies and reservoir significance in the meandering modern Peace River and ancient McMurray Formation, Alberta, Canada. Sedimentology. 56(6), 1655-1669.

Smith, D. G., Hubbard, S.M., Lavigne, J.R., Leckie, D.A., Fustic, M., (2011). Stratigraphy of counter-point bar and eddy-accretion deposits in low-energy meander belt of the Peace-Athabasca Delta, northeastern Alberta, Canada. In Davidson, S.K., Leleu, S., North, C.P., (ed) From River to Rock Record: The preservation of fluvial sediments and their subsequent interpretations. Society for Sedimentary Geology. 97.

Sylvester, Z., Durkin, P., Covault, J.A., (2019). High curvatures drive river meandering. Geology. 47, 563-566.

Sylvester, Z., Durkin, P.R., Hubbard, S.M., Mohrig, D., (2021). Autogenic translation and counter point bar deposition in meandering rivers. The Geological Society of America. 133(11/12), 2439-2456.

Tang, M., Zhang, K., Huang, J., Lu, S., (2019). Facies and the architecture of estuarine tidal bar in the Lower Cretaceous McMurray Formation, central Athabasca Oil Sands, Alberta, Canada. Energies. 12, 1769.

Taylor, G., Crook, K.A.W., Woodyer K.D., (1971). Upstream-dipping foreset cross-stratification; origin and implications for paleoslope analyses. Journal of Sedimentary Research. 41(2), 578-581.

Termini, D., Piraino, M., (2011). Experimental analysis of cross-sectional flow motion in a large amplitude meandering bend. Earth Surface Processes and Landforms. 36, 244-256.

Thomas, R.G., Smith, D.G., Wood, J.M., Visser, J., Calverley-Range, E.A., Koster, E.H., (1987). Inclined heterolithic stratification – Terminology, description, interpretation and significance. Sedimentary Geology. 53(1-32), 123-179.

Thorne, C.R., Lewin, J., (1979). Bank processes, bed material movement, and planform development in a meandering river. *In:* Rhodes, D.D., Williams, G.P. (eds). Adjustment of the Fluvial System. Kendall Hunt, Dubuque, 117 – 137.

Toonen, W.H.J., Kleinhans, M.G., Cohen, K.M., (2012). Sedimentary architecture of abandoned channel fills. Earth Surface Processes and Landforms. 37(4), 459-472.

Viseras, C., Henares, S., Yeste, M.L., Garcia-Garcia, F., (2018). Reconstructing the architecture of ancient meander belt by compiling outcrop and subsurface data: A Triassic example. In Ghinassia, M., Colombera, L., Mountney, N.P., Reesink, A.J.H., (eds), Fluvial meanders and their sedimentary products in the rock record. International Association of Sedimentologists.

Willis, B.J., (1989). Palaeochannel reconstructions from point bar deposits: a three-dimensional perspective. Sedimentology. 36, 757-766.

Willis, B.J., Tang, H., (2010). Three-dimensional connectivity of point-bar deposits. Journal of Sedimentary Research. 80, 440-454.

Wood, J.M., (1989). Alluvial architecture of the Upper Cretaceous Judith River Formation, Dinosaur Provincial Park, Alberta, Canada. Bulletin of Canadian Petroleum Geology. 37(2), 169-181.

Yan, N., Colombera, L., Mountney, N.P. (2024). Sediment preservation and accretion rates of fluvial meander-belt deposits: variations with temporal scale and river size. Geological Society, London, Special Publications, 540(1), SP540-2022.

CHAPTER THREE:

SEM ANALYSIS OF POORLY INDURATED POINT-BAR MUDSTONE MICROSTRUCTURE: IMPLICATIONS FOR MUDSTONE DEPOSITION IN ANCIENT RIVERS

3.1. Introduction

The understanding of the formative processes of mudstones has undergone significant revision in recent decades. Traditional models consider mud deposition as vertical stacking of mud-sized particles that fall out of suspension due to quiescent or non-energetic conditions (Garrels and Mackenzie, 1971; Chamley, 1989; Aplin et al., 1999; Potter, 2005; Macquaker and Bohacs, 2007). However, there is ample evidence that suggests mud particles are often transported and deposited as aggregates, such as intraclasts, flocs, and fecal pellets, in modern marine environments (Pryor, 1975; Kineke and Sternberg, 1995; McAnally et al., 2007; Becker et al., 2013; Nishida et al., 2013; Fall et al., 2021) and have been identified in ancient marine mudstones (Odom, 1967; Pryor and Vanwie, 1971; Alplin and MacQuaker, 2011; Plint et al., 2012; Egenhoff and Fishman, 2013; Plint, 2014; Birgenheier et al., 2017; Knapp et al., 2017; Laycock et al., 2017; Li and Schieber, 2018; Boulesteix et al., 2019). This research has broadened our understanding of the hydrodynamic conditions under which mud is deposited and better integrates a wider array of processes and mechanisms that are often overlooked in mudstone analyses, including electrochemical, biochemical, biophysical and interface dynamics of fine-grained sediment (Bennett et al., 1991).

To investigate mudstone microstructure, studies have used scanning electron microscopy (SEM) and thin section analysis to present evidence of mudstone aggregates (Aplin and Macquaker, 2011; Jiang, 2013; Plint, 2014; Laycock et al., 2017; Pavan, 2019), verifying previous hypotheses that suggested physical properties of single clay mineral platelets are of little importance in mud transportation and deposition (Moon, 1972). Rather, clay platelets exist as components in a hierarchy of fine-grained aggregates in both suspended and deposited mud and mudstone (Bennett et al., 1981; Lee et al., 2012; Soulsby et al., 2013; Plint, 2014; Fall et al.,

2021; Dunne et al., 2024), ranging from electrochemically bonded individual clay particles (i.e., domains; Moon, 1972; Bennett et al., 1991), to mudstone intraclasts comprising smaller clay aggregates, silt- to fine-sand-sized quartz or feldspar grains, organic matter, and a range of other constituents of lesser proportions (Plint, 2014; Laycock et al., 2017). Abundant evidence shows that mudstones occupy a broad suite of discernable lithofacies based on microstructure observations (Nishida et al., 2013; Li and Schieber, 2018; Boulesteix et al., 2019), and the spectrum of depositional conditions they occur in lead some authors to suggest a re-evaluation of many previous marine mudstone interpretations is necessary (Schieber and Southard, 2009; Macquaker et al., 2010b).

While the evolution of understanding marine mudstone is well underway, likewise attention to microstructure observations and their implications in fluvial mudstone deposits has been lacking, with some exceptions (Pavan, 2019; Plint, 2019). Although previous research suggests that salt cations (i.e., saltwater or brackish water) are essential for overcoming repulsive forces between negatively charged clay particles (i.e., cohesion via electrochemical flocculation; White, 1961; Pryor, 1975; Tan et al., 2015; Bergenheier et al., 2017), growing evidence shows that organic matter is also a catalyst for clay aggregation (i.e., adhesion via organic 'glue'; Liss et al., 1996; Shanks, 2002; Potter et al., 2005; Macquaker et al., 2010a; Soulsby et al., 2013; Fall et al., 2021). In addition, laboratory experiments have demonstrated that kaolinite is more susceptible to flocculation in pure deionized water than saline water (Schofield and Samson, 1954; Dunne et al., 2024). The presence of suspended mud aggregates in modern freshwater rivers, floodplains, and lakes has been empirically and theoretically demonstrated (Weilenmann et al., 1989; Droppo and Ongley, 1994; Droppo et al., 1997; Slattery and Burt, 1997; Gerbersdorf et al., 2008; Fox et al., 2014; Lamb et al., 2020; Le et al., 2020; Osborn et al., 2023; Nghiem et

al., 2023; Dunne et al., 2024). These studies provide ample evidence that mud aggregates are a significant fraction of the suspended material in modern river systems, but the linkages between aggregate suspension and bedload transport and deposition are difficult to demonstrate. Flume experiments show that bedload transport of mud aggregates in freshwater does exist (Schieber et al., 2007; Plint, 2019). However, due to the difficulty in preserving microstructure during burial and diagenesis, mudstone aggregates, and the microstructures that would suggest bedload transportation, have yet to be definitively documented from ancient fluvial environments.

The present study investigates the microstructure of point-bar mudstones by analyzing samples from the Lower Cretaceous McMurray Formation at Imperial Oil Ltd.'s Kearl mine, an open-pit oil sands mine in northeastern Alberta (Fig. 3.1). These poorly indurated, shallowly buried mudstones have excellent potential to preserve the original depositional structure of muds deposited in an ancient river. The hypothesis of this research is that much like their marine counterparts, fluvial muds are often comprised of silt- and sand-sized aggregates of clay and minor fine-grained constituents (e.g., quartz, organic material, etc.) that were transported as suspended and bedload material in flowing water. This is investigated by developing a methodology to impregnate poorly indurated mudstone using a low viscosity epoxy resin (LR White), subsequently preparing the sample for SEM investigation, and using SEM imaging to characterize mudstone samples from an outcropping point-bar deposit. This investigation has implications for the paleohydraulic conditions of the mudstone fraction of inclined heterolithic stratification (IHS; Thomas et al., 1987), which has often been attributed to tidal influences including salt-induced clay flocculation and energy fluctuation due to flow reversals (Nouidar and Chellaï, 2001; Sutherland et al., 2015; La Croix et al., 2019).

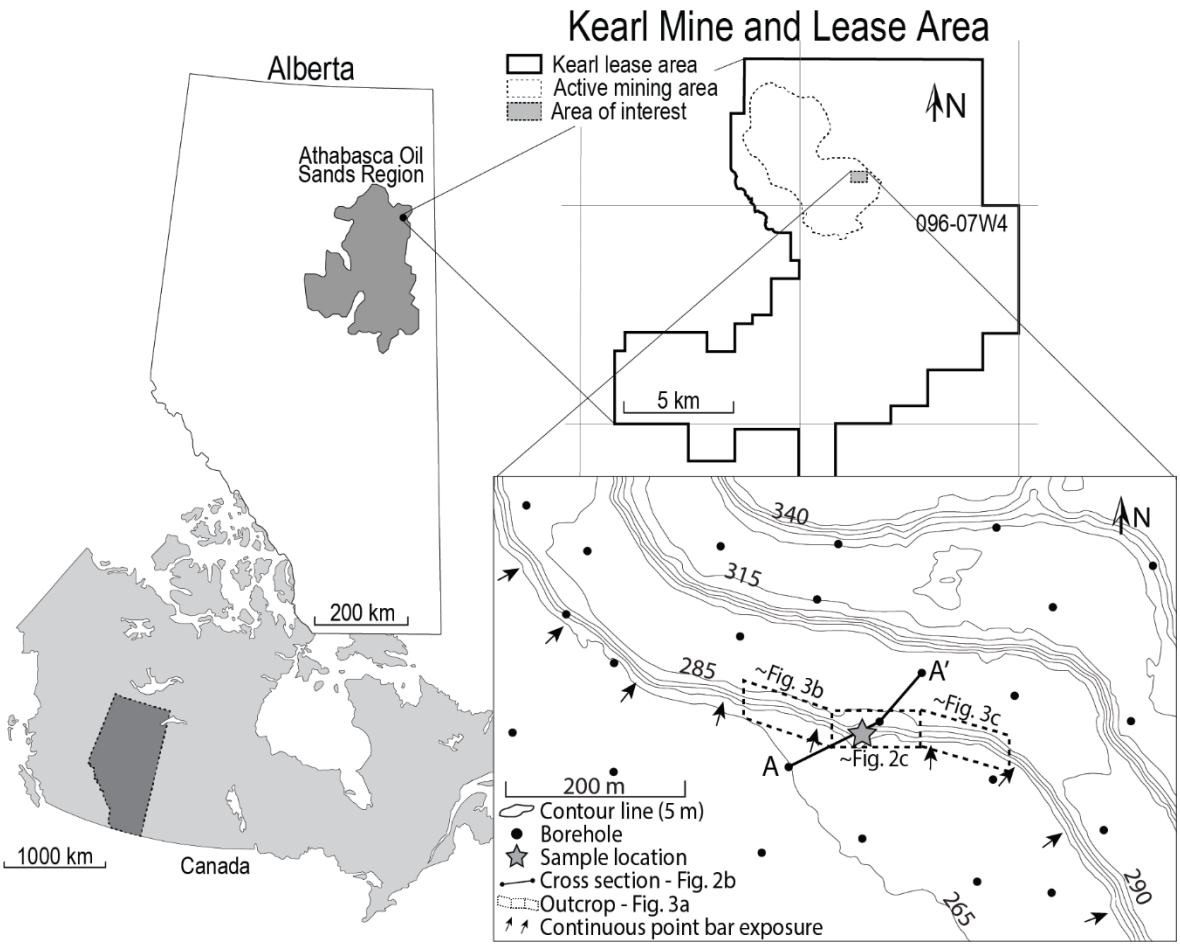

Figure 3. 1 Location of Kearl mine and the area of interest. The area of interest is displayed with a topographic map of the mine.

3.2. Background Geology and Study Area

The Cretaceous McMurray Formation comprises an amalgam of terrestrial deposits (e.g., fluvial, lacustrine, floodplain) and marginal-marine deposits (e.g., shoreface and deltaic; Flach and Mossop, 1985; Hein and Cotterill, 2006; Chateau et al., 2021). The majority of the terrestrial deposits in the McMurray Formation are channel-belts that are vertically stacked (Hein and Cotterill, 2006; Peng et al., 2024), and commonly heterogeneous with upward-fining grain-size profiles typical of point bars in meander-belt deposits (Hein and Cotterill, 2006; Durkin et al., 2017; Martinius et al., 2017). The fine-grained components often represent mudstone-dominated

abandoned-channel fill deposits or mud- and silt-rich interbeds in point-bar IHS. The McMurray Formation outcrops at the surface in northeastern Alberta, where open-pit oil sands mining is utilized for heavy bitumen recovery.

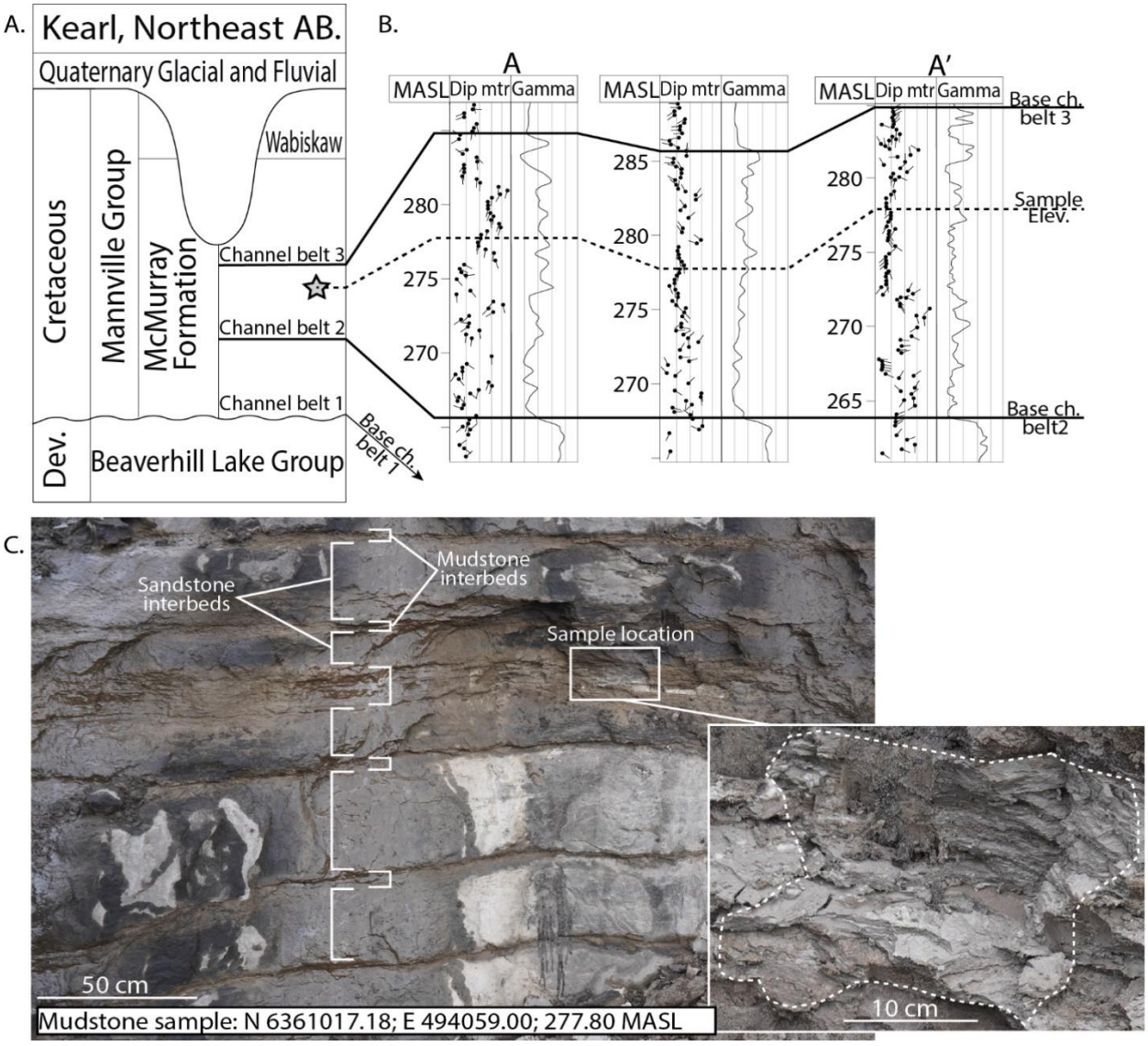

Figure 3. 2 Stratigraphy and sample location in the area of interest. (A) Stratigraphic chart of Kearl mine comprising the Mannville Group (McMurray Formation and Wabiskaw Member) and bounding units. The grey star marks the approximate location of the mudstone sample. (B) Cross section A-A'. Cross section location is labelled in Figure 3.1 and comprises the three closest wells to the mudstone sample location. Well-log datum is the base of channel-belt 2 (*M2.5 in Chapter 2*). Each well log comprises well tracks, from left to right, elevation in meters above sea level (MASL); dip-meter from 0 - 50°; and gamma-ray from 0 – 150 API. (C) Outcrop photograph of sample location showing IHS sandstone and mudstone interbeds. The sample was taken from a thick mudstone interbed.

The area of interest in Kearl mine is an excavated section of the mine that exposes three well-preserved, stacked channel-belt deposits (channel belt 1, 2 and 3; Fig. 3.2). Channel belt 1 is a floodplain dominated valley fill. The top of channel belt 1 is locally exposed in the floor as the base of mining excavation in the study area. It is erosionally overlain by channel belt 2, a 15 – 25 m-thick channel-belt deposit that outcrops in mine-faces in the area of interest (Figs. 3.2C, 3.3) where the mudstone for this study is sampled. Channel-belt 3, an approximately 40-m thick upward-fining deposit, top truncates channel-belt 2 (channel-belt 3; Fig. 3.2A, 3.2B).

Channel-belt 2 contains a point-bar deposit with well documented upward-fining, south-dipping IHS deposits and eastward paleoflow in the area of interest (e.g., *chapter 2*, Fig. 2.6A, architectural element VIII). IHS characterization is based on outcrop (Figs 3.2C, 3.3) and bedding orientation from three nearby well logs (Fig. 3.2B). The point-bar deposit is approximately 700 x 900 m in area with an average thickness of 15 – 20 m. It is characterized by an upward-fining succession typical of a point-bar deposit, including a sandstone-dominated base with large-scale (~1 m) trough cross-bedding transitioning upwards to IHS deposits (Fig. 3.3).

3.3. Methods

3.3.1. Sample Collection

Safe mining practice at Kearl prohibits approaching the mine face. This makes *in-situ* sample collection difficult. An abandoned jump ramp transecting a 17-meter vertical mine face was utilized for safe hand-sample collection, providing means to sample *in-situ* material approximately 10-meters above the base of the paleochannel (Figs. 3.2B, 3.3). The outcrop was recently exposed (circa. 2023) and therefore minimally weathered, enabling identification of the local sedimentological characteristics (Figs. 3.2C, 3.3). Data from three wells, each within 125

meters of the sampled location (one of the wells is within 20 meters) is also provided in a cross section that transects the sample location (Fig. 3.2B).

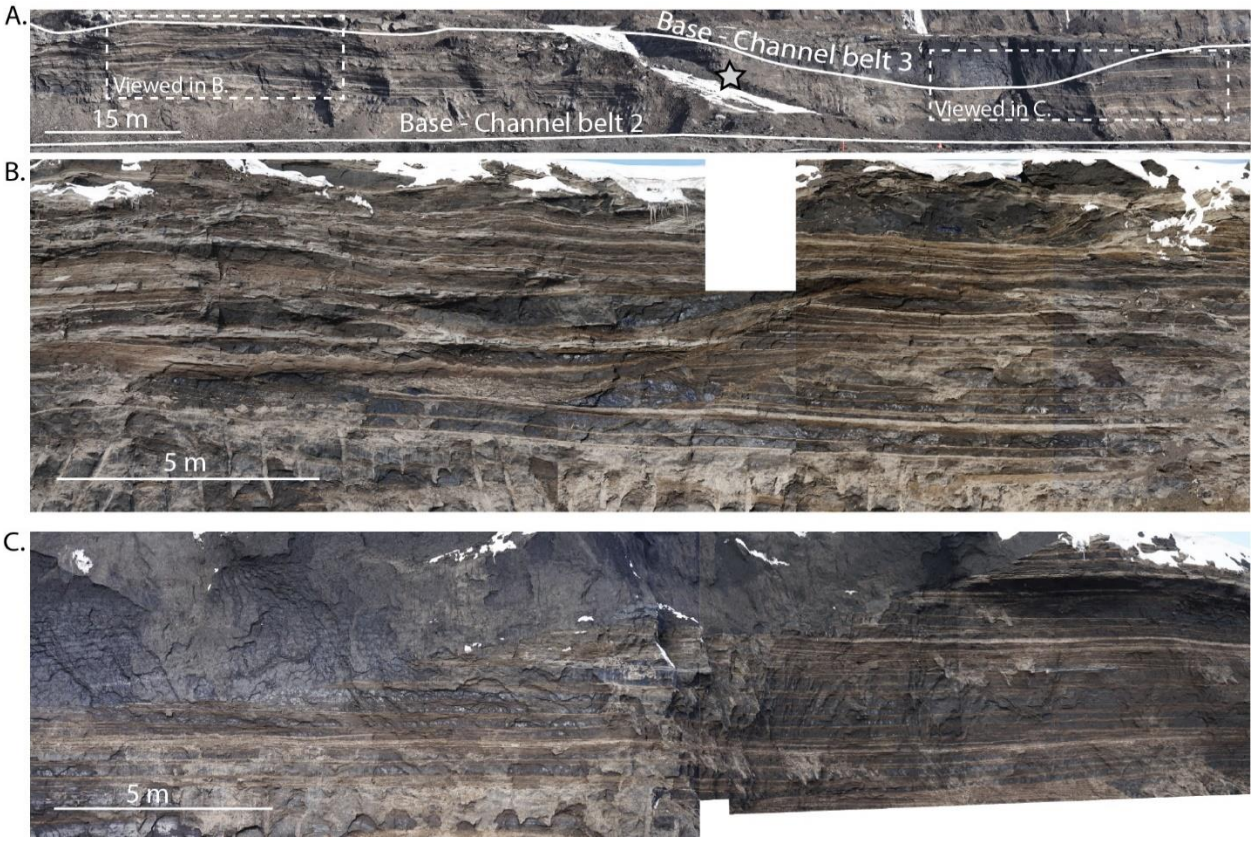

Figure 3. 3 Full mine-face outcrop of the sample location and lateral deposits. Outcrop scale is derived from shovel teeth markings. (A) Wide view of outcrop displaying the jump ramp that granted access to the mudstone sample. Dotted white rectangles represent higher resolution photographs of the outcrop in 3.3B and 3.3C. (B) Outcrop located to the west of the mudstone sample location, comprising IHS interbeds (*Eastern margin of FA5 deposits in Chapter 2*). (C) Outcrop located to the east of the mudstone sample location, comprising IHS interbeds and overlying incision (*FA1 deposits in Chapter 2*).

The sampled mudstone was approximately 13 cm in thickness, 25 cm in length and 15 cm in width (Figure 3.4A). The sample was collected from laterally continuous light-grey mudstone bed, 15-cm-thick, with minor sandstone and siltstone interbeds (Fig. 3.2C), bounded above and below by medium- to coarse-grained trough cross-bedded sandstone. As with most of the surface mineable McMurray Formation, the sample was poorly indurated, easily deformed when water

saturated and prone to crumbling when dry. Therefore, the sample was carefully wrapped with plastic wrap and securely packaged before being delivered to the University of Manitoba for further sample processing.

In the sedimentology laboratory of the Clayton H. Riddell Faculty of Environment, Earth, and Resources in University of Manitoba, the sample was unwrapped and left to dry naturally for 4 months in room-temperature conditions (~19 – 22°C), after which the sample was cut in half parallel to bedding with a hack saw (Figs. 3.4A, 3.4B). The two halves were gradually shaved down with a razor blade to shape two rectangular prisms with straight-edge surfaces parallel and perpendicular to bedding to be certain post-collection handling deformation was removed and to expose the cross-sectional sedimentary properties (Fig. 3.4D). Thin (~2 – 4 mm) chips were carefully cut from the samples with a serrated razor blade (Figs. 3.4D, 3.5A, 3.5B), that fit into a cylindrical glass container ~ 25 mm in diameter (1- to 2-ounce glasses). The sample was placed as flat as possible before beginning the ethanol dehydration and LR White resin impregnation phases.

3.3.2. Sample Dehydration and Resin Impregnation

The mudstone sample impregnation method was modified from techniques used to view smectite expansion microstructure in marine mudstones (Sanchez-Roa et al., 2018; Kim et al., 1995), with the exclusion of their initial rehydration and clay expansion phase. To ensure minimal microstructure modification, dehydration and resin impregnation phases were done without moving nor touching the sample. This was accomplished by using pipettes to add and remove solutions to and from the glass container, with particular attention given to injecting fluids beneath the sample to eliminate potential air bubbles. As recommended, the LR White

resin was thoroughly mixed with accelerant for 30 minutes and stored in a refrigerator at 4°C for 24 hours before initial use.

For the dehydration phase, the sample was immersed into 95% ethanol solution twice for 2 hours, then once more for 4 hours. The epoxy embedding phase was then performed by sequentially immersing the sample in 1:2 and 1:3 parts ethanol (95%) and LR White solution for two hours each (ethanol and LR White solutions were thoroughly mixed with a stir stick before sample immersion), then in pure LR White and left in the refrigerator at 4°C overnight (approximately 12 hours). The next day the sample was immersed in pure LR White twice for 4 hours, then immersed a final time and placed in an oven at 60°C for 24 hours to fully cure. Once removed from the oven, the glass container was carefully broken by squeezing in a bench vice and removed from the resin puck.

This methodology was refined over repeated attempts with 8 separate mud chip samples that produced variable success. Five samples were deemed appropriate for SEM investigation. Of the failed samples, it is noted that samples should not be prepared in plastic containers — LR White will chemically react with plastic during the curing phase, leaving a cloudy contamination in the cured resin puck. It is recommended that mud chips be no thicker than 2 mm for full resin impregnation. Mud sample chips herein were 2 – 4 mm thick, and the thicker mud samples were not penetrated completely by the resin. In relatively homogenous mudstone samples, the resin was able to penetrate approximately 1 mm into the mud, perpendicular to exposed surfaces (Figs. 3.5C – 3.5F). In samples with thin, silt-rich interlaminae, the resin was able to impregnate laminae and adjacent mudstone (Figs. 3.5C, 3.5D).

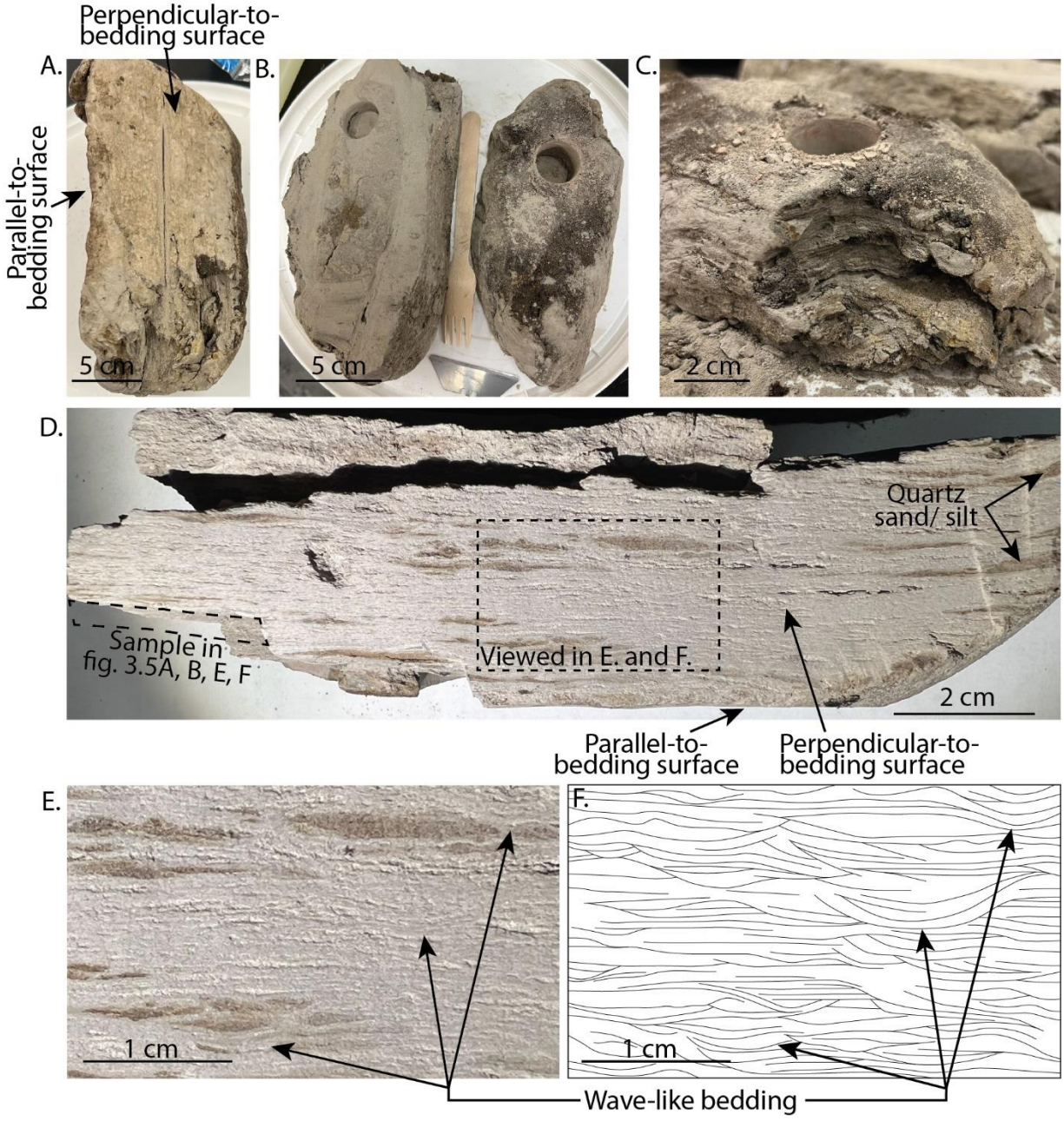

Figure 3. 4 Mudstone sample preparation photographs. (A) Mudstone sample after dehydration. (B) Mudstone sample after being cut in half. (C) An example of a broken surface showing the lithology of the mudstone sample. (D) One of the mudstone sample halves after shaving with a razor to show surfaces parallel and perpendicular to mudstone bedding. (E) Zoomed in location from 3.4D. (F) Zoomed in location from 3.4D with traced bedding showing mm-scale wave-like bedding.

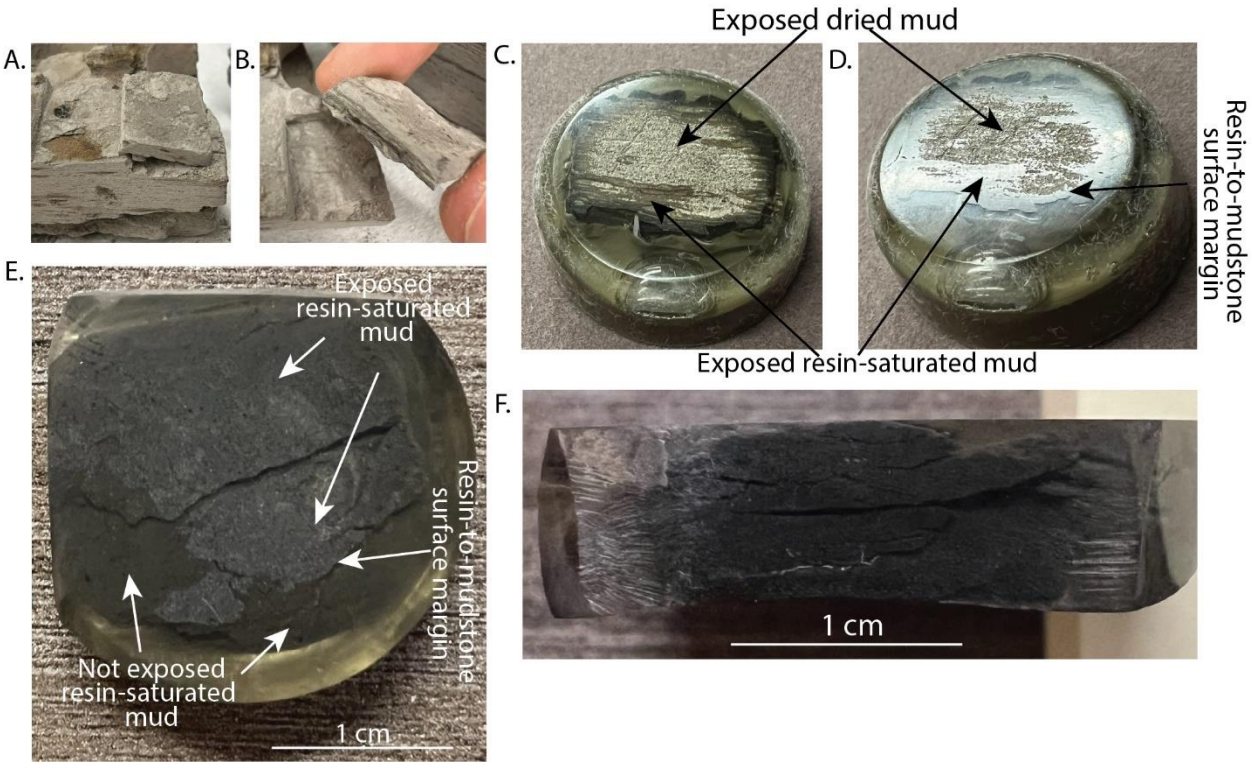

Figure 3. 5 Mudstone sample preparation photographs. (A, B) show a mudstone chip taken from the sample that was used for sample preparation. After completed preparation this mudstone chip is displayed in 3.5E and F. (C) Photograph showing a failed sample after preparation. Dried mudstone is lighter in colour than the epoxy resin-saturated mudstone. (D) Photograph showing the same failed sample. Surface texture of exposed, epoxy resin-saturated mudstone and dried mudstone is observed. (E) Photograph showing successful sample after preparation. Contrast between exposed epoxy resin-saturated mudstone and non-exposed mudstone is observed. Mudstone bedding is parallel to the exposed surface (i.e., horizontal section). (F) Photograph showing successful sample after preparation. Mudstone bedding is perpendicular to the exposed surface (i.e., vertical section). This is the same sample shown in 3.5A, B and E.

3.3.3. Sample Polishing

To ensure maximum microstructure preservation the resin puck was dry-sanded and polished by hand using 400-grit sandpaper until the mudstone is initially exposed. The sandpaper grade was then reduced to 600, 800, 1200 and 2000, until >50% of the mud sample surface has been exposed. The sample is then hand polished with a dry polishing pad with very light pressure. This sanding and polishing method was successfully conducted parallel to bedding in

samples 1 – 5 (e.g., Fig. 3.5E). A vertical section of sample 5 was also successfully prepared perpendicular to bedding (Fig. 3.5F). In cases where dried mudstone (i.e., mudstone not penetrated by resin) was exposed during sanding (e.g., Figs. 3.5C, 3.5D), the resulting mud smear caused destruction of the microstructure and clouded the rest of the surface, rendering it inadequate for SEM investigation.

3.3.4. Scanning Electron Microscopy (SEM)

SEM observations and analytical data were collected to investigate microstructural properties of the mudstone hand sample. Five individual samples were successfully prepared from the hand sample for analysis at the University of Manitoba SEM lab. All five samples were laid flat and viewed perpendicular to bedding where the resin-impregnated mud was exposed. One sample was also placed on edge to view the sample perpendicular to bedding. A focus of image investigation was to observe, if present, µm-scale mudstone aggregates. The compositional similarity between potential aggregates and surrounding matrix material, as well as the aggregate size make these aggregates impossible to view without the aid microscopic analysis (Li and Schieber, 2018). Previous SEM studies that have interpreted similarly-described µm-scale mudstone aggregates were used to compare the images acquired in this research (Jiang et al., 2013; Plint, 2014, Laycock et al., 2017; Li and Schieber, 2018; Pavan, 2019).

3.3.4.1.Backscattered Electron (BSE) Imaging

To observe microstructure in the mudstone samples, BSE imaging was performed using an Inspect S50 electron microscope manufactured by the Field Electron and Ion (FEI) Company (Figs. 3.6A, 3.6C). Samples were viewed without carbon coating in low pressure mode (~ 45 Pa) at approximately 10 mm of working distance. Beam energy was 20 Kv and count time was 20 s.

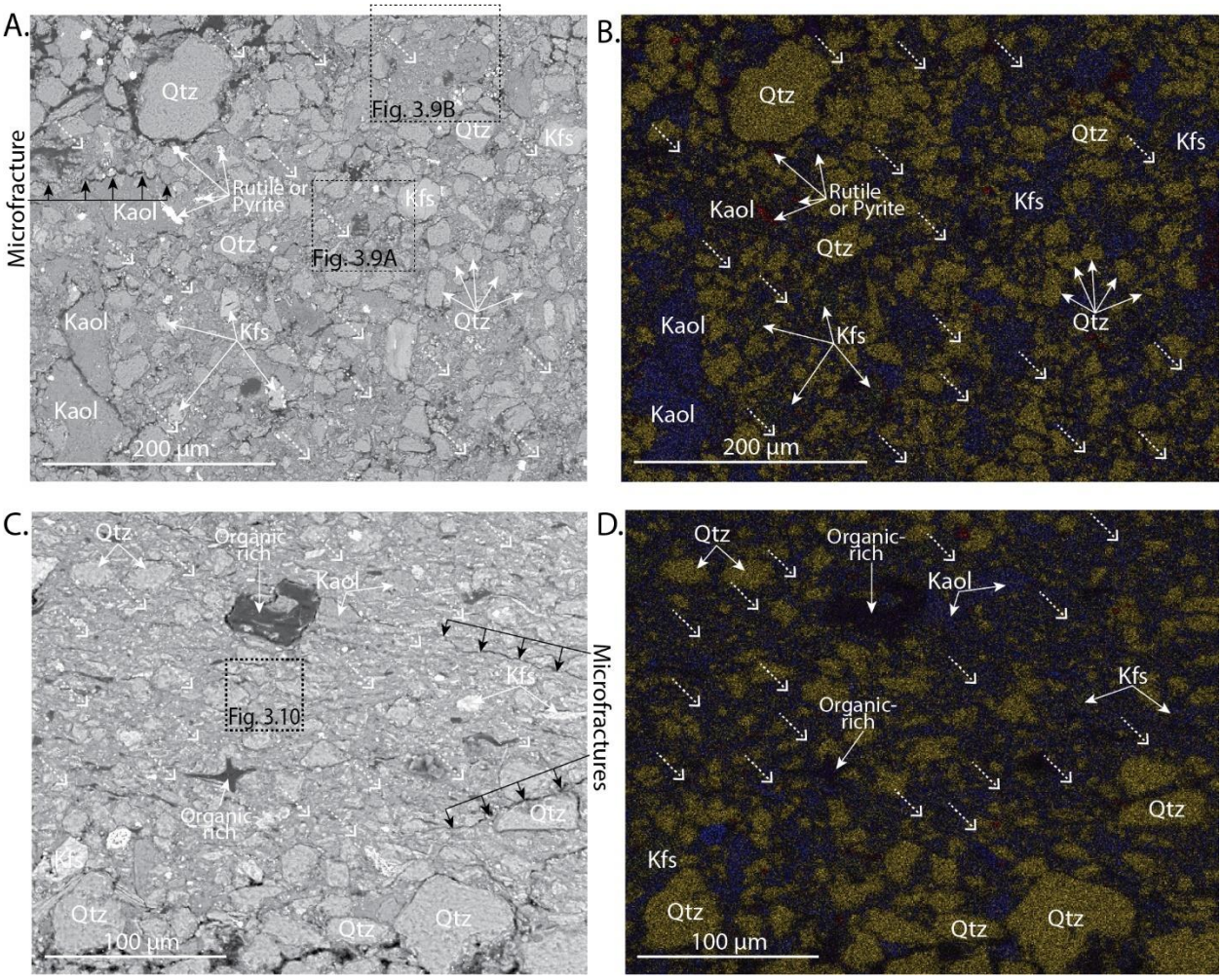

Figure 3. 6 Overall mudstone microstructure in SEM imaging. Diagonal dotted white arrows represent apparent matrix containing illite-clay with minor silt- to clay-sized, non clay minerals. Qtz indicates quartz grains, Kfs indicates feldspar grains, Kaol indicates kaolinite grains. (A) Horizontal section of mudstone sample. Black arrows indicate microfracture planes. Dotted black rectangles show locations of Figures 3.9A and 3.9B. (B) Element map of 3.6A. Yellow is Si, blue is Al, red is Ti and Fe, and purple is C. (C) Vertical section of mudstone sample. Black arrows indicate microfracture planes. Dotted black rectangles show locations of Figures 3.9A and 3.9B. (D) Element map of 3.6C. Yellow is Si, blue is Al, red is Ti and Fe, and purple is C.

3.3.4.2.Energy Dispersive Spectroscopy (EDS)

Elemental distribution and proportions were analyzed with EDS for mineral identification using an Octane Pro silicon drift detector (SSD) and software, manufactured by EDAX, Inc. Elemental mapping was utilized in selected areas of interest to measure element distributions in

the sample (Figs. 3.6B, 3.6D). Elements mapped in this study were Si, Al, K, C, Ti and Fe. Element maps were used for differentiating clay from non-clay minerals (e.g., quartz, feldspar, etc.). Spot scanning techniques were utilized to identify individual grain mineralogy.

3.4. Results & Analysis

3.4.1. Hand Sample Description

The hand sample is a light-grey silty mudstone (Fig. 3.4). Clay-rich areas are grey and appear massive to weakly horizontally laminated with lighter and darker grey interlaminae. Some localized mm-scale wave-form bedding was also observed (Figs. 3.4E, 3.4F). Wispy, discontinuous interlaminae of silt- and sand-sized quartz are present, comprising < 10% of the sample (Fig. 3.4D). Quartz grains are brown from bitumen coating. Some mm-scale nodules and black carbon-rich clumps were encountered during the shaving process. Small (~mm), elliptical sand-filled burrows are rare.

3.4.2. SEM Investigation

3.4.2.1.Mineralogy

Element mapping shows element composition and abundances of the horizontal and vertical sections (Figs. 3.6B, 3.6D). Si-rich areas represent quartz and occupy approximately 30 – 40% of the sample. Al-rich areas represent K-feldspar and large kaolinite crystals comprising approximately 10 % of the sample. Sub-equal Al and Si areas are clay minerals and occupy 35 – 45% of the sample. Fe and Ti indicate minor pyrite and rutile grains typically occupying <5% of the sample. C represents either carbon-rich detrital material (i.e. organic detritus), bitumen, or pore space that has infilled with epoxy resin, cumulatively occupying approximately 10% of the

sample material. Clay minerals are dominantly illite with minor kaolinite and mica minerals. Less than 1% of the rock comprises unidentified clay minerals.

3.4.2.2.Texture

BSE images of a horizontal and vertical section are presented in Figure 3.6A and 3.6C, respectively. Mudstone sample sections contain grains ranging from < 1 – 200 µm with framework mineral grains easily discernable from matrix material. No apparent depositional fabric is observed in horizontal sections (Fig. 3.6A), but in vertical sections there is weak sub-horizontal grain orientation and fracture planes (Fig. 3.6C). Apparent pore space (infilled with organic material), or microfractures are observed as dark grey cracks (Figs. 3.6A, 3.6C). These microfractures appear randomly disperse along framework grain boundaries or between compositionally equivalent matrix material in horizontal sections. In vertical sections they weakly align dipping approximately 20° above and below horizontal (Fig. 3.6C). Bioturbation is not apparent in SEM imaging, although a single kaolinite grain with a 10-µm-wide meandering tube-form infilled with quartz was observed (Figs. 3.7A, 3.7B).

Framework grains mainly consist of silt- to fine sand-sized quartz, feldspar and kaolinite that range from sub-rounded to sub-angular. Quartz grains are commonly equant and lighter-grey than kaolinite but darker than feldspar on average (Figs. 3.6A, 3.6C). Quartz grains are up to 150 µm large and average approximately 30 – 70 µm. Some large quartz grains contain finer quartz along grain margins, and have a rough, shallow pockmarked surface texture (Figs. 3.6A, 3.6C). Feldspar grains are up to 200 µm large and more angular relative to quartz. The tabular or elongate habit of feldspar is often observed and influences grain alignment in vertical sections. Evidence of feldspar alteration to kaolinite is present with large tabular kaolinite pseudomorphs and examples of interfingering feldspar-kaolinite margins within individual crystals (Fig. 3.7C).

Minor framework grains comprise pyrite and rutile, observed as white spots in BSE imaging, and organic material observed as dark grey to black (Figs. 3.6A, 3.6C).

The matrix material is clay-rich with minor clay- to silt-sized grains of quartz, pyrite, rutile and organic material. Clay minerals make up approximately 80 – 90% of the clay-sized material. Kaolinite clay, as stated above, is often relatively large pseudomorphic grains with tightly packed and organized mineral alignments. Illite is the most dominant clay mineral present in the matrix material. In high magnification individual illite grains are weakly observed, aligning together in parallel clusters (Figs. 3.7D, 3.7E). Preferred illite alignment is observed as parallel layering, often near microfractures or framework grain boundaries (e.g., Figs. 3.8A, 3.9A). The parallel layering occasionally encompasses localized μm-scale clusters of compounded clay within the matrix material (Figs. 3.8, 3.9). Vertical sections show sub-horizontal illite alignment that is also influenced by larger adjacent grains (Fig. 3.10). Both horizontal and vertical sections show evidence of weakly defined mosaic-forms within the illite matrix that are consistent with previous mudstone aggregate identifications (Plint, 2014; Laycock et al., 2017). Within the mosaic-form components (i.e., potential aggregates), further magnification shows discrete zones of illite-grain mineral alignments in smaller clusters (Figs. 3.8C, 3.11B).

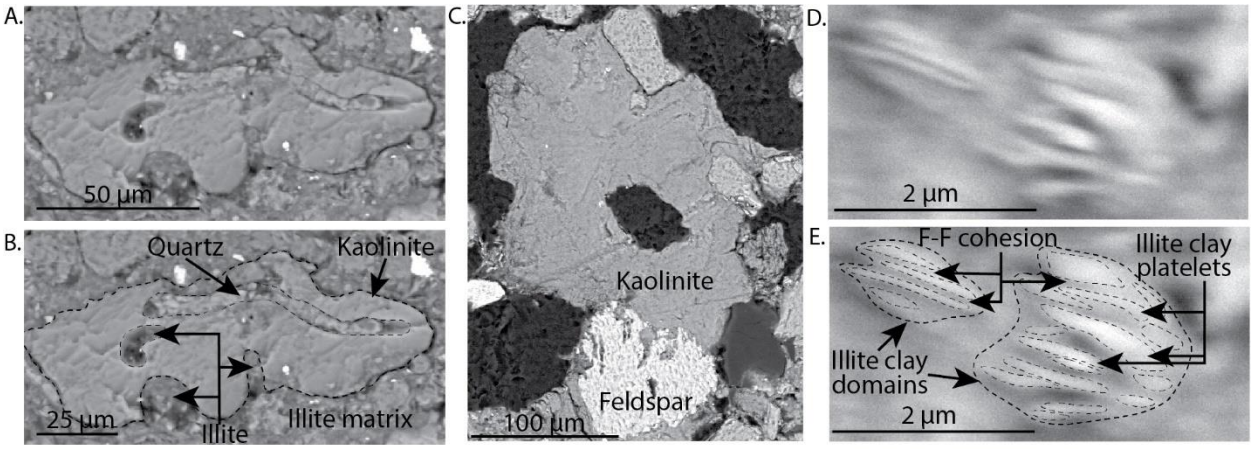

Figure 3. 7 SEM examples of textural preservation in mudstone samples. (A) Kaolinite grain with tube-like structures filled with quartz and illite. (B) Labelled image of 3.7A. (C) Feldspar grain (light grey) that is partially altered to kaolinite (darker-grey). (D) Image of illite platelets arranged in book-case stacks. (E) Labelled image of (D).

3.4.2.3.Mudstone Aggregates

Mudstone aggregates have been observed in various forms in previous studies including fecal pellets (Pryor, 1975; Macquaker et al., 2010b; Li and Schieber, 2018), shale lithics (Plint, 2014; Laycock et al., 2017; Jiang, 2013; Pavan, 2019) and intraclastic aggregates (Plint, 2014; Laycock et al., 2017). The present research focuses on recognition of intraclastic aggregates, defined as aggregates of clay minerals with dispersed non-clay fine silt grains and organic material (Plint, 2014). They are often irregularly shaped in horizontal view and flattened or elongate in vertical sections (e.g., mud rip-up clasts in Li and Schieber, 2018). Deposited mudstone aggregates are inherently difficult to observe due to post depositional compaction and the low compositional contrast between aggregates (Li and Schieber, 2018). Therefore, evidence of aggregate boundaries is an important recognition criterion.

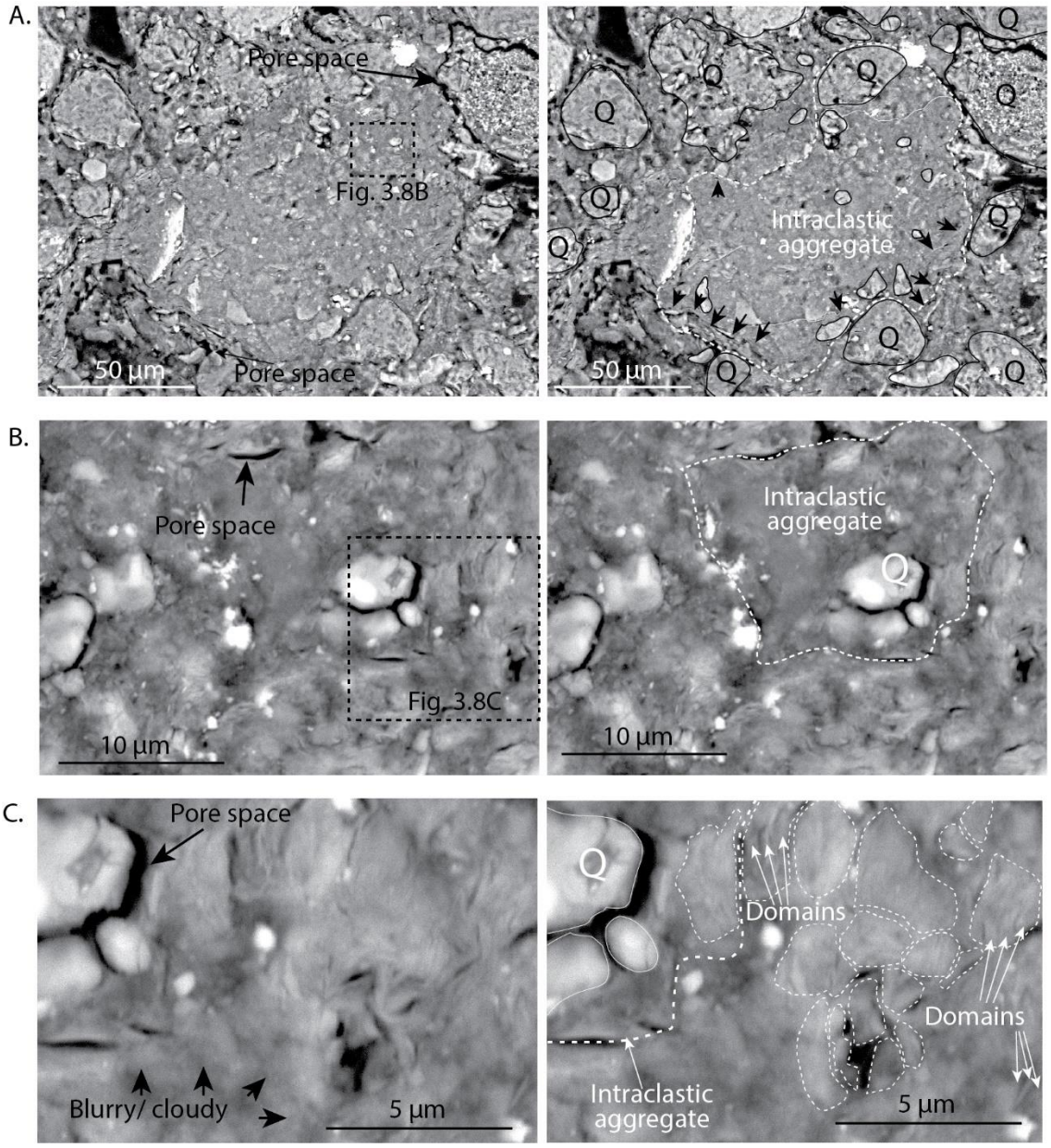

Figure 3. 8 SEM image of potential mudstone aggregate in horizontal section. Q indicates quartz grains. Left image in (A) is potential mudstone aggregate with arrows indicating potential pore space or microfractures. Dotted black rectangle represents the location of Figure 3.8B. Right image in (A) illustrates mudstone aggregate margin (white dotted line), quartz-grain margins (solid black lines) and black arrows represent illite mineral alignment at margins of the mudstone aggregate. Left image in (B) is a zoomed in section of the mudstone aggregate in 3.8A. Dotted black rectangle represents the location of the zoomed in image in 3.8C. Right image in (B) illustrates smaller mudstone aggregate margin (white dotted line). Left image in (C) is a zoomed in section of 3.8B. Right image in (C) illustrates mudstone aggregate margin (bold white dotted line) and domains (thin white dotted lines).

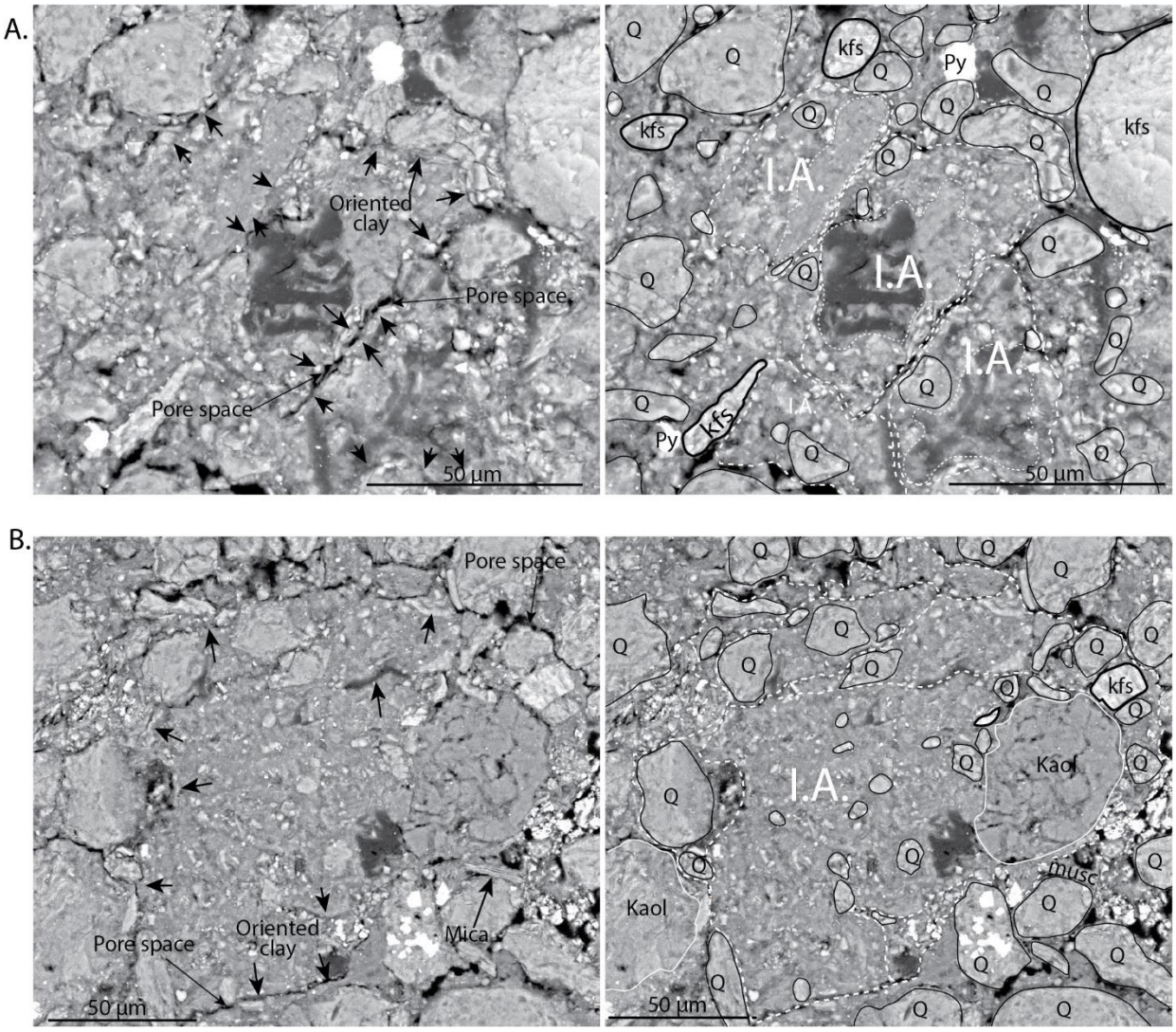

Figure 3. 9 SEM image of potential mudstone aggregate in horizontal section. Q indicates quartz grains, kfs indicates feldspar grains, Py indicates pyrite grains, Kaol indicates kaolinite grains, I.A. indicates intraclastic aggregates. Left images in (A) and (B) are potential mudstone aggregate with arrows indicating illite mineral alignment to aggregate margins. Right images in (A) and (B) illustrates mudstone aggregate margin (white dotted line), quartz and feldspar grain margins (solid black lines) and kaolinite grain margins (solid white lines). Locations of (A) and (B) are shown in Figure 3.6A.

The intraclastic aggregates observed in this study contain an illite clay-dominated matrix (> 90%) with and minor silt- to clay-sized non-clay mineral constituents of quartz, k-feldspar, rutile, pyrite, organic material (Figs. 3.8 – 3.11). The aggregate boundaries are commonly defined by localized illite mineral alignment parallel to aggregate margins, adjacent framework

grain boundaries, and carbon-rich areas (dark-coloured) that are likely pore space and/ or microfractures. Intraclastic aggregates are up to 150 µm large and often irregular-shaped but equant in horizontal sections (Figs 3.8A, 3.9A, 3.9B), and elongate 15 µm thick, 150 µm long shapes that bend around larger adjacent framework grains in vertical sections (Fig. 3.10). Some intraclastic aggregates contain a dark-grey coloured illite-dominant core with an increasing proportion of non-clay mineral constituents towards the aggregate margins (Fig. 3.9). Within illite-dominant zones of intraclastic aggregates, local strong parallel alignments of clay sheets are observed, representing smaller illite aggregates.

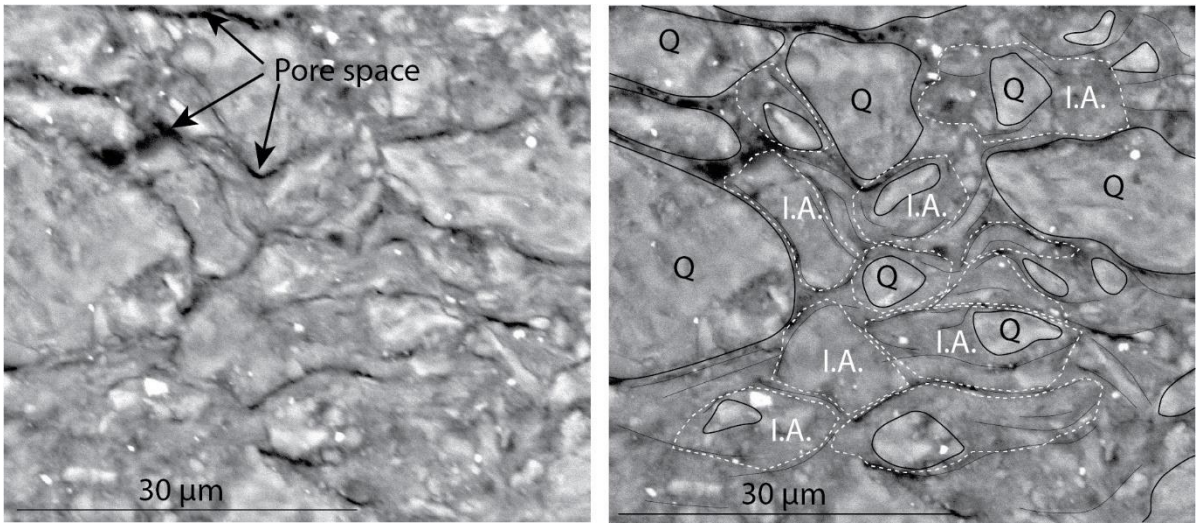

Figure 3. 10 Left image shows SEM image of potential mudstone aggregates in vertical section. Right image is an annotated image of the same potential mudstone aggregates in vertical section. Solid black lines represent quartz (Q) grains, dotted white lines represent intraclastic aggregates (I.A.). Image location is shown in Figure 3.6C.

The smaller-sized illite aggregates (<1 – 8 µm) are unimodal in composition, containing illite platelets with alignment resembling a 'bookcase' or 'stair-stepped' structure (Figs. 3.8C, 3.11B), and appear to be a large portion of the constituent material in intraclastic aggregates (Figs. 3.8B, 3.11A). The packets of parallel illite platelets are consistent with in observations and descriptions of face-to-face cohesion of clay particles called domains (Moon, 1972; Bennett et

al., 1981; Plint, 2014). The margins of domains are poorly defined with weak appearance of pore space around their boundaries (Figs. 3.8C). These observations were somewhat rare because high magnification of illite-rich material commonly reveals a blurry or cloudy texture (Figs. 3.8C, 3.11B). The blurry appearance may be a result of the weak vacuum or textural abrasion during the sanding and polishing process. Another explanation could be that these areas represent micro-pore space within clay-rich material that is infilled with epoxy resin that is subsequently damaged by the electron beam during observation.

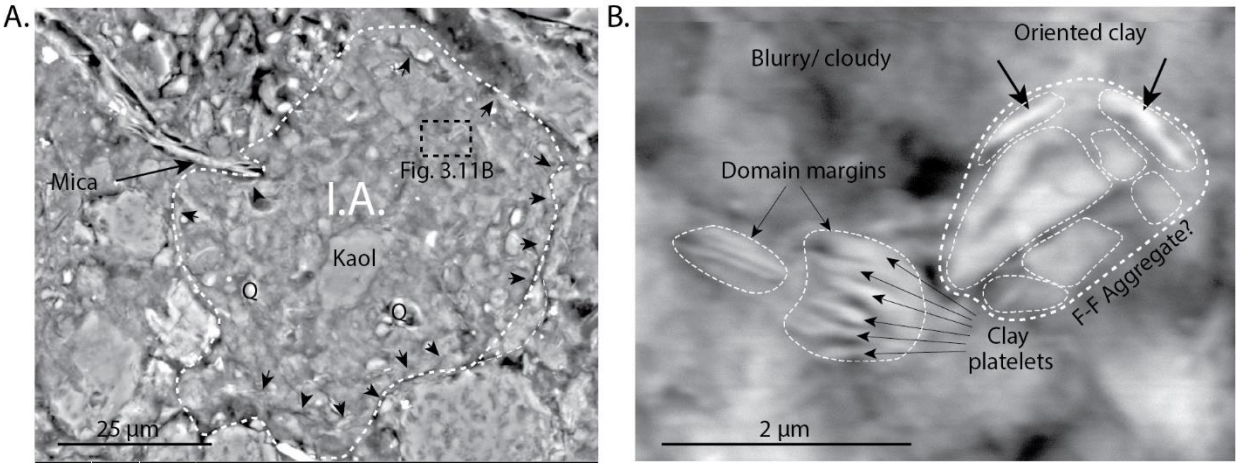

Figure 3. 11 SEM image of potential mudstone aggregate in horizontal section. (A) Intraclastic aggregate with illite-dominant composition. Kaol indicates kaolinite grain, I.A. indicates intraclastic aggregate. White dotted line represents intraclastic aggregate margin, black arrows represent illite mineral parallel alignment to aggregate margin, black dotted rectangle is viewed in (B). Magnified image of the intraclastic aggregate microstructure. Thin black dotted lines represent domain margins, thicker black dotted lines represent an aggregate of domains. Image outside of illustrated aggregate and domains appear blurry or cloudy.

3.5. Discussion

3.5.1. Methods for mudstone microstructure investigation

The growing documentation and understanding of clay aggregation elucidates the importance of microstructure investigation when characterizing fine-grained deposits.

Unfortunately, this has proven difficult with ancient mudstone, as post-depositional processes like compaction, structural deformation, biogenic and diagenetic alterations often destroy original microstructures (Aplin and Macquaker 2011; Laycock et al., 2017). Even in well-preserved mudstone, field and hand samples can appear homogenous (Macquaker and Adams, 2003), causing difficulty in viewing potential aggregate boundaries. Furthermore, rock sampling and preparatory techniques for microscopic investigation can alter or destroy original microstructure in poorly indurated mudstone samples. To overcome such obstacles this study developed a preparatory method to penetrate poorly indurated mudstone pore space with epoxy resin in order to observe the microstructure using SEM analysis. In essence, hardening of the epoxy resin was utilized to imitate natural cementation, therefore maximizing preservation of the microstructure. The sample location selected was an excellent source for ancient mudstone SEM investigation because it was: 1) buried at a shallow depth and not exposed to significant pressure and temperature changes over time, 2) existed on a passive intracratonic location, exhibiting only minor tilting of regional strata deformation, and 3) exposed to near-surface and subaerial conditions just 4 months before being sampled, preventing extensive weathering processes (e.g., freeze-thaw cycles, oxidation, etc.).

A similar attempt to observe poorly lithified mudstone from the Mississippi Delta was conducted by Bennett et al. (1981), with some success. Their method enabled the observation of microstructure in clay (e.g., clay aggregates), however, physical procedures to expose the sampled viewing surface was conducted before epoxy resin impregnation. The study describes trimming and cutting the mud samples to the necessary viewing size and shape before epoxy resin application, exposing the delicate clay features to mechanical disturbances. In the present study, the mudstone was impregnated with epoxy resin, filling the pore space with competent

material, then the viewing surface was exposed via gentle sanding and polishing without water. This technique minimized potential microstructure disturbance and provided the possibility to observe cross-sections of clay aggregates, if present. A cross-section provides more robust evidence of mudstone aggregates, and quantitative data of their sedimentary texture. It is of note that the epoxy resin used in Bennett et al. (1981) had a viscosity of 60 centipoise (cPs; SPURR epoxy resin), whereas the epoxy resin in this study had a viscosity of 8 cPs (LR White).

3.5.1.2. Microstructure preservation

The main objective of this method was to preserve delicate microstructures, and several examples indicate that this technique was successful. Epoxy resin impregnation is visible based on colour and texture on the surface of samples that have been sanded and polished sufficiently to expose the mudstone (Figs. 3.5C, 3.5D, 3.5E). When epoxy resin-saturated mudstone is exposed, it is dark grey and smooth, while the dried, non-impregnated mudstone is light grey and rough (Figs. 3.5C, 3.5D). The partial impregnation caused the dried mudstone to roll and clump together during sanding and polishing, while epoxy resin-saturated clay grains were held in their original position.

Evidence of microstructural preservation is also observed in SEM imaging. A 10-µm-wide, 90-µm-long, slightly undulating tunnel infilled by quartz was observed within a very-fine-sand-sized kaolinite grain (Figs. 3.7A, 3.7B). Illite-filled tunnels are also evident in the same grain. These structures indicate potential bioerosion and a presence of microbial production after deposition (Lamb et al., 2020). The preservation of micron-scale borings indicates minimal disturbance of the delicate features within the sample. Delicate features are also observed in the feldspar to kaolinite alteration in Figure 3.7C. There is sharp contrast between the hard feldspar (white) and soft kaolinite (grey), indicating relatively equal surface topography between

contrasting compositions and minimal differential surface abrasion during the sanding and polishing process, likely the result of epoxy resin impregnation increasing the kaolinite hardness to sub-equivalent values of hardness in the feldspar. Lastly, the highly magnified images (> 8000 magnification) in Figures 3.7D and 3.7E show clay platelet morphology within the illite domains. These clay particles have likely been held in place due to epoxy resin impregnation of surrounding pore spaces, and the similar appearance of the domain microstructure with previous research (Moon, 1972; Bennett et al., 1981; Plint, 2014) and the oblate clay platelet morphology (Bennet et al., 1981; Potter et al., 2005) indicates significant preservation of original microstructure.

Notably, some textural properties are observed that could be a result of sample disturbance during sanding and polishing. The shallow pockmark texture on the surface of quartz and K-feldspar grains and the presence of smaller quartz grains lining the margins of larger ones potentially indicates abrasion markings and minor grain shattering, respectively. In SEM studies of similar lithologies, quartz grains are smoother, and less fracturing is evident along quartz grain boundaries (e.g., Figures 7 – 10 in Plint, 2014; Figure 5 in Laycock et al., 2017). However, these examples used a high vacuum seal for SEM imaging and the shale samples were not as poorly indurated as the mudstone in this study.

With evidence suggesting that the preparatory method used in this study was relatively successful, it is important to note that the mudstone sample was more consistent with the competency of modern mud deposits than ancient mudstone or shale that is well indurated. The hand sample was highly deformable when saturated, much like a piece of wet clay recovered from a riverbank. The preparatory methodology, therefore, may be attempted on modern mud deposits with similar success. Since the availability of ancient fluvial mudstone that could be

utilized for SEM investigation is limited in the rock record due to post-depositional alteration and deformation, perhaps modern fluvial mud investigations could satisfy the recognition criteria for the evidence of, or lack there of, mudstone aggregate deposition in fluvial environments.

3.5.2. Mudstone Aggregates – Previous Work and Comparisons

Oceanography, limnology, and hydraulic research documents suspended flocculated clay particles, or aggregates, in most aqueous environments (Eisma et al., 1986; Droppo and Ongley, 1994; Nguyen et al., 2022; Dunne et al., 2024). Such environments include marine deltas (Fox et al., 2004; Dunne et al., 2024), estuaries (Eisma, 1986; Syvitski et al., 1995; Wintwerp, 2001; van Leussen, 2011; Soulsby et al., 2013; Fall et al., 2021), and other shallow- (i.e., nearshore; Shanks, 2002; Lee et al., 2012) and deep-marine settings (i.e., offshore; Quigg et al., 2020). Similar clay aggregates are also observed in terrestrial environments like floodplains (Lamb et al., 2020), lacustrine (Welienmann et al., 1989) and fluvial settings (Walling and Moorehead, 1989; Droppo et al., 1997; Slattery and Burt, 1997; Bungartz and Wanner, 2004; Nghiem et al., 2023; Osborne et al., 2023; Abolfazli et al., 2024). Furthermore, many of the above studies document that suspended sediment comprises mud aggregates in much higher proportions than individual clay particles, with some reporting > 97% of suspended sediment volume occurring as mud aggregates in freshwater rivers (Droppo and Ongley, 1994; Le et al., 2020).

A common observation in both suspended clay sediment and within deposited mudstone is the presence of mudstone aggregate hierarchies based on aggregate size. The smallest form of mudstone aggregates are parallel stacks of individual clay platelets called domains (i.e., primary particles; Moon, 1972; Bennett et al., 1981). Domains were first recognized by Moon (1972), replacing the preceding model that identified individual clay platelets as the lowest order of

aggregate constituents, or primary particles, that aggregates can be naturally broken down to. Plint (2014) refined work from Bennett et al. (1981), delineating aggregate hierarchies in marine mudstones into three orders comprising first-order domains, second-order face-to-face (F-F) aggregates, and third-order intraclastic aggregates. Table 3.1 presents numerous studies, including the present study, that documents similar hierarchies in both suspended clay and deposited mudstone aggregates. Each sequential order comprises two or more aggregates of the lower order.

Observations presented in figures 8 and 9 in Plint (2014) are comparable to results herein, where < 1 – 8 μm clay packets, or domains (Figs. 3.7C, 3.7D, 3.8C; 3.11B), make up the constituents of larger, higher order intraclastic aggregates (Figs. 3.8A, 3.11A). Although intraclastic aggregate margins are interpretive, certain microtextural traits have been recognized for defining aggregate margins.

Aggregate margins are interpreted in this study by pore space infilled by bitumen, epoxy resin, or both. Pore space was possibly exaggerated during the drying phase of sample preparation. Since the bonds between the largest mudstone aggregates (i.e., highest order aggregates) are weakest and will fracture first when introduced to stresses (Eisma et al., 1986; Jarvis et al., 2005; Partheniades, 2009; Tan et al., 2015), it is assumed that micro-fracturing occurs along margins of the highest-order aggregates during the sample drying phase (e.g., Figs. 3.8 – 3.10).

Table 3. 1 Mud and mudstone research, aggregate hierarchies and comparisons.

Studies	Hierarchy Level								Sample type - *Sample location*	Environment
	Primary Constituent		2nd Order		3rd Order		4th Order			
	Nomenclature	*Size (µm)*	*Nomenclature*	*Size (µm)*	*Nomenclature*	*Size (µm)*	*Nomenclature*	*Size (µm)*		
Dunne et al., 2024	Clay particle/ organic material	~ 1.0	hyper-stable aggregate	~10	Semi-stable aggregate	~ 100.0	-	-	Suspended - *Mississippi Delta*	Deltaic
Fox et al., 2004	Clay particle	-	Floc	266.0	-	-	-	-	Suspended - *Po River Delta*	Deltaic
Fall et al., 2021	Primary particle	-	Flocculi	-	Microfloc	35.0 - 50.0	Macrofloc	130.0 - 200.0	Suspended - *York River*	Estuarine
Soulsby et al., 2013	Primary particle	-	Microfloc	< 160.0	Macrofloc	> 160.0	-	-	Suspended - *Several European estuaries*	Estuarine
van Leussen, 2011	NA	-	Microfloc	~ 5.0 - 40.0	Macrofloc	200.0 - 700.0	-	-	Suspended - *Ems Estuary*	Estuarine
Eisma, 1986	NA	-	Microfloc	< 125.0	Macrofloc	<4000.0	-	-	Suspended - *Ems Estuary*	Estuarine
Syvitski et al., 1995	Component particle	3.0 - 13.0	Floc	415.0 - 1320.0	-	-	-	-	Suspended - *Halifax Inlet*	Estuarine
Lee et al., 2012	Primary particle	0.25 - 2.5	Flocculi	10.0 - 20.0	Microfloc	50.0 - 200.0	Macrofloc	> 200.0	Suspended - *North Sea / Belgian coast*	Nearshore
Weilenmann et al., 1989	Particle	-	Aggregate	4.5 - 30.0	-	-	-	-	Suspended - *Lake Zurich & Smepach*	Lacustrine
Osborn et al., 2023	Primary particle	5.0 - 10.0	Floc	75.0 - 200.0	-	-	-	-	Suspended - *Mississippi River*	Fluvial
Abolfazli et al., 2024	Primary particle	13.0	Floc	80.0 - 220.0	-	-	-	-	Suspended - *Mississippi River*	Fluvial
Slattery and Burt, 1997	Primary particle	-	Aggregate	13.1 - 50.3	-	-	-	-	Suspended - *Corwold Hills streams, U.K.*	Fluvial
Droppo and Ongley, 1994	Primary particle	1.0 - 2.6	Aggregate	2.2 - 138.1	-	-	-	-	Suspended - *Creeks and rivers; ON, CA*	Fluvial
Laycock et al., 2017	Constituent grain	15.0 - 22.0	Aggregate	14.0 - 611.0	-	-	-	-	Mudstone - *Carlile Formation*	Offshore
Plint, 2014	Domain	0.5 - 1.0	F-F aggreggate	2.0 - 5.0	Intraclastic aggregate	5.0 - >20.0	-	-	Shale - *Dunvegan Formation*	Deltaic
Bennett et al., 1981	Domain	-	Flocs or chains	-	-	-	-	-	Mud - *Mississippi Delta*	Deltaic
Present study	-	< 8.0	-	< 150.0	-	-	-	-	Mudstone - *McMurray Formation*	*Fluvial*

Some studies included measurements of non-clay primary constituents - e.g. phytoplankton detritus, non-clay minerals, biogenic material, etc.; Fluvial deposits were freshwater.

Aggregates of hierarchies higher than domains (i.e., F-F aggregates, intraclastic aggregates; Plint, 2014) are often lined by parallel orientations of clay minerals. There are two types of mineral orientations observed. The first being angular, elongate mica grains aligning on the outside of the aggregate margins, suggesting a detrital process of sediment aggregation (Fig. 3.9B; Jiang et al., 2013). The second is illite grain alignment on the inner perimeter of aggregate margins (Figs. 3.8A, 3.9A, 3.9B, 3.11A), showing a decrease in mineral alignment, or lack of alignment, towards the aggregate center (e.g., Fig. 3.9A). Plint (2014) attributes marginal grain alignment to the presence of a sticky substance, possibly bacterial or algal mucous, acting as a binding agent within and on the surface of the aggregates causing clay particles to adhere during turbulence and grain collisions in the water column (i.e., bioflocculation). Jiang (2013) notes that detrital clay particles commonly adhere in a parallel orientation to larger clay aggregate margins due to the presence of organic content and adds that authigenic clay growth often aligns perpendicularly to the boundary of larger grains, which is not observed herein.

There is a building body of evidence concerning the biological component of clay aggregation (i.e., bioflocculation) in freshwater fluvial settings (Droppo and Ongley, 1994; Carlough et al., 1996; Liss et al., 1996; Gerbersdorf et al., 2008; Fox et al., 2014). Since bioflocculation does not rely on salt ions for electrochemical adhesion by overcoming repulsive forces between clay particles (Bennett et al., 1991), the inorganic constituents would not have excluded non-clay grains. In this study, non-clay constituents are observed near the margins of larger aggregates in Figure 3.9A, where fine (< 5 μm) quartz, pyrite and rutile grains are increasingly present towards the aggregate boundaries. A potential formative process for these aggregates could be the ‘snowball-like’ effect described in Pryor and Van Wei (1971), where the genesis of sand-sized mudstone aggregates is explained by rolling bedload material accumulating

debris while travelling, though a binding agent is not described therein. Bedload clay aggregate transport has been demonstrated in laboratory settings (Schieber et al., 2007; Schieber and Southard, 2009) and interpreted in marine mudstone investigations (Macquaker et al., 2010b; Li and Schieber, 2018), but has yet to be decisively recognized in ancient fluvial deposits.

3.5.3. Implications for Fluvial Mudstone Deposition

The heterogeneity of fluvial deposits is well-known, comprising an amalgam of siliciclastic grain-sizes that are variably sorted by channel energy (Jordan and Pryor, 1992). However, with the growing evidence of pervasive mudstone microstructure observations, fine grained deposits may be more intricate than previously interpreted. Suspended aggregate sizes in a fluvial environment are primarily governed by shear turbulence through a hydrodynamic cycle of simultaneous aggregate destruction and construction (Partheniades, 2009; Abolfazli et al., 2024). Turbulence limits the maximum aggregate size by breaking the weaker bonds between large aggregates while also promoting collision and cohesion between smaller aggregates due to increased sediment mixing (Eisma et al., 1986; Winterwerp and van Kesteren, 2004; Partheniades, 2009; Pavan, 2019). The continuous cycle of aggregation and destruction ensures that suspended aggregates are likely always present in aquatic environments. This elucidates a key complexity in fluvial mudstone sedimentology that is not yet understood—mud aggregates in aquatic environments are sorted hydrodynamically not only by erosion-deposition cycles, but also by aggregate size fluctuations concurrent with transportation.

In stagnant environments like abandoned channels, clay and silt are the dominant sedimentary deposit (Toonen et al., 2012; Bellizia et al., 2021). However, on the opposite side of the energy spectrum, channels may erode and transport these mudstone deposits, subsequently

depositing mudstone clast breccias downstream (Labrecque et al., 2011; Broughton, 2018; Chen et al., 2022). Mudstone clast investigations are often limited to macro mudstone clasts, or mudstone clasts that are evident in outcrop, core or hand sample (i.e., > 0.5 cm). Furthermore, evidence of hydrodynamic sorting of clasts in breccia deposits is not often observed and appear massive in structure, restricting mudstone clast breccia deposition to be interpreted as rapid and chaotic (e.g., Labrecque et al., 2011; Musial et al., 2012; Horner et al., 2019). Although massive structures may be present in some examples, mudstone clast breccias can also comprise distinct structure. Figure 3.12 shows freshly excavated mine-faces with 10's of meters in lateral exposure of point-bar deposits located within the same channel-belt as the mudstone sample in this study. Outcrops show that mudstone clasts, from dm- mm-scale sizes, do adhere to hydrodynamic conditions by lining foresets and bottomsets of trough cross-bedded deposits. This suggests that mudstone aggregates, or mudstone clasts, of various sizes were deposited in hydrodynamically equivalent conditions of coarse sand grains. Furthermore, Figure 3.12 shows that mudstone beds can also line foresets and bottomsets of trough cross-bedded sandstone. As mentioned above, bedded mudstone and mudstone clasts often represent deposition on opposite ends of the energy spectrum. While this can be true, and fluctuating energy conditions may explain these juxtaposed mudstone deposits, it is noteworthy to consider that the μm-scale intraclastic aggregates interpreted in Figures 3.8 – 3.11 occur in a mudstone interbed of IHS deposits (Figs. 3.2, 3.3). If this interpretation of intraclastic aggregates is correct, a greater range of potential energetic conditions conducive to mudstone clast (i.e., mudstone intraclastic aggregate) deposits may be needed. This study postulates that mudstone aggregates occur from the dm- to mm-scale (e.g., Fig. 3.12), as well as the sub-mm-scale, possibly appearing as mudstone beds when investigating without microscopic aid (e.g., Figs. 3.8 – 3.11). Therefore, fluvial mudstone beds may not

necessarily be limited in deposition to extremely low or stagnant energy conditions as previously considered (e.g., Potter et al., 2005), but also as bedload material in higher energy conditions (Pavan, 2019; Plint, 2019).

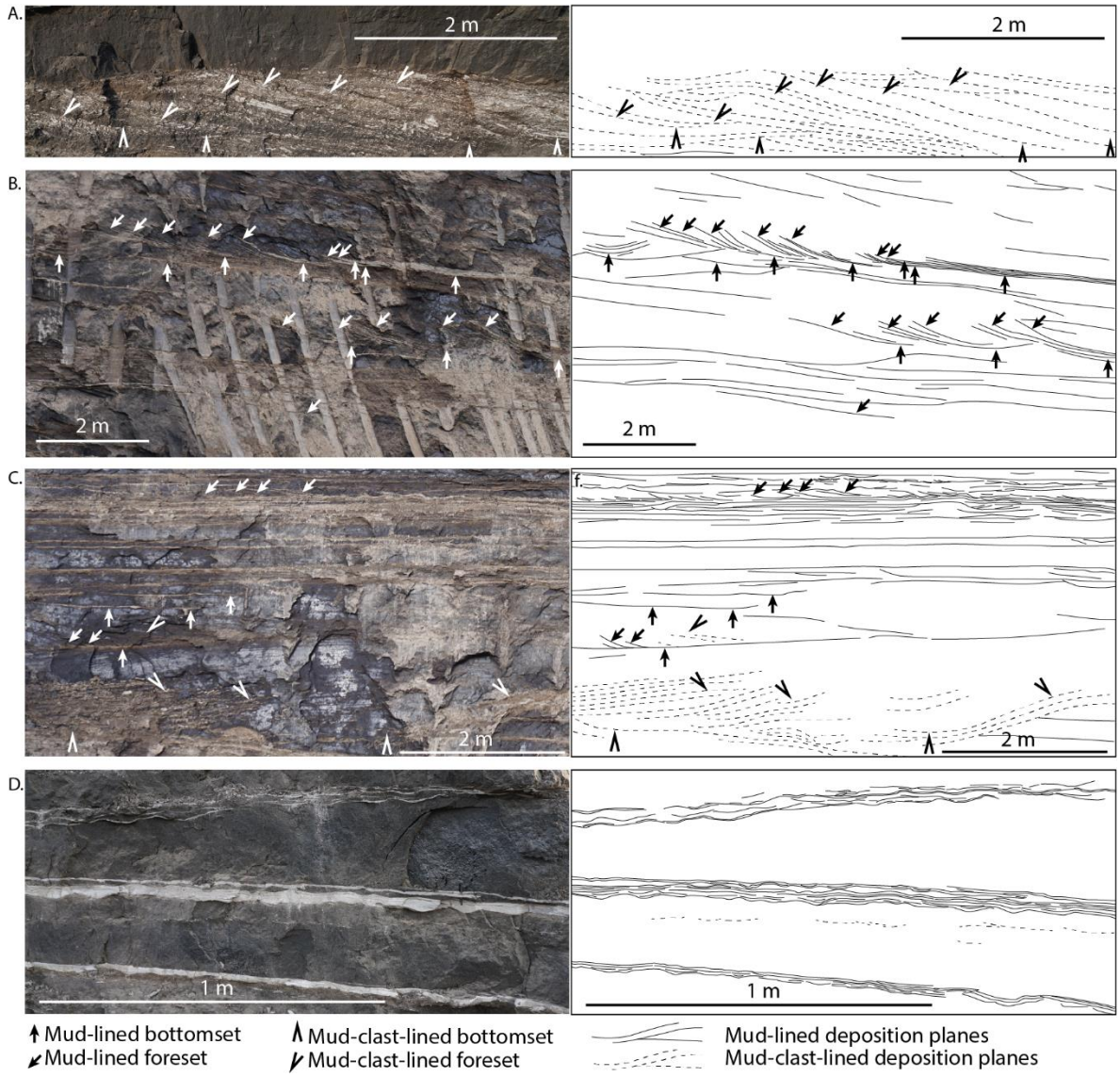

Figure 3. 12 Various mine face outcrop photographs displaying mudstone deposits interbedded with sandstone. (A) Boulder- to sand-sized mudstone clasts aligning to trough cross-bedding foresets and bottomsets. (B) Mudstone laminae and layers aligning with trough cross-bedding foresets and bottomsets. Some mudstone clasts are observed as well. (C) Mudstone laminae and layers aligning with trough cross-bedding foresets and bottomsets and ripples. Some mudstone clasts are observed as well. (D) Mudstone layers and laminae interbedded with and overlying sandstone ripples. Each image shows traced bedding planes lined by mudstone (solid black lines) or mudstone clasts (dotted black line) on the right.

3.6. Conclusion

Mudstone aggregates are observed in suspension in all aquatic environments (Droppo et al., 1997; Nguyen et al., 2022; Dunne et al., 2024), and therefore, deposition of those aggregates in subaqueous sedimentary deposits should follow. In microstructural investigation of marine mudstone, aggregates have been recognized using SEM imaging (e.g., Aplin and Macquaker, 2011; Plint, 2014; Laycock et al., 2017). Marine shales are often well-cemented, adequately preserving microstructure when sampled and treated for analysis. The contribution of fluvial mudstone microstructure observation has proven difficult, however, as samples are often poorly indurated or too significantly deformed in the deep rock record.

Here, a consistent method is developed to sample these less indurated fluvial mudstones by epoxy-resin saturation methods. A mudstone sample from the Cretaceous McMurray Formation was successfully treated for SEM investigation. The mudstone was soft and deformable upon acquisition, but after an experimental epoxy-resin impregnation method was conducted the sample was artificially cemented, and results suggest that microstructure preservation was relatively successful. The original condition of the mudstone suggests that perhaps similar treatment to modern mud deposits could produce similar results.

Upon investigation, the mudstone microstructure evidence was compared to findings in marine mudstone SEM analyses, and similarities are observed. Criteria defining enigmatic mudstone aggregate boundaries are present, including apparent pore-space or microfractures and mineral grain alignment to aggregate margins. Furthermore, apparent mudstone aggregates contained similar hierarchical characteristics in size and texture to previous studies (e.g., Bennett et al., 1981; Plint, 2014). Small aggregates (< 8.0 μm) were observed as neat stacks of clay

individual clay platelets that are similar to domains (Bennett et al., 1981), which make up to primary, lowest order of aggregates in the hierarchy. Larger aggregates (< 150.0 – 8.0 μm) comprise clusters of domains, non-clay detrital constituents (i.e., silt-sized quartz, feldspar, pyrite, rutile and carbonaceous debris), and illite clay with unrecognizable microstructures commonly referred to as intraclastic aggregates (e.g., Plint, 2014).

The initial findings herein have potential implications for the presence of mudstone aggregates in fluvial deposits and could refine the depositional conditions of fluvial mudstones. Particularly, the mudstone component of IHS deposits have often been attributed to mudstone draping in quiescent water conditions during seasonal or tidal energy fluctuations. Mudstone aggregates, however, travel as bedload in flume experiments (e.g., Schieber et al., 2007), suggesting that fluvial mudstone aggregates, if present, are deposited in a larger field of flow conditions than previously interpreted. The small sample size herein, however, leaves room for speculation in this interpretation. Although the growing abundance of research concerning suspended fluvial mud aggregates and marine mudstone investigations are broadening our understanding of the complexities in mudstone deposition, continued work with focus on fluvial mudstone microstructure is needed.

3.7. References

Abolfazli, E., Osborn, R., Dunne, K.B.J., Nittrouer, J.A., Strom, K., (2024). Flocculation characteristics of suspended Mississippi River mud under variable turbulence, water and salt sources, and salinity: a laboratory study. Frontier in Earth Science. 12, 1268992.

Aplin, A.C., Macquaker, J.H.S., (2011). Mudstone diversity: Origin and implications for source, seal, and reservoir properties in petroleum systems. American Association of Petroleum Geologists Bulletin. 95(12), 2031-2059.

Aplin, A. C., Macquaker, J.H.S., Fleet, A.J., (1999). Muds and mudstones: Physical and fluid flow properties. Geological Society (London) Special Publication.

Becker, M., Schrottke, K., Bartholoma, A., Ernstsen, V., Winter, C., Hebbeln, D., (2013). Formation and entrainment of fluid mud layers in troughs of subtidal dunes in an estuarine turbidity zone. Journal of Geophysical Research. 118(4), 2175-2187.

Bellizia, E., Boaga, J., Fontana, A., D'Alpaos, A., Cassiani, G., Ghinassi, M., (2021). Impact of gensis and abandonment processes of a fluvial meander on geometry and grain-size distribution of the associated point bar (Venetian Plain, Italy). Marine and petroleum geology. 127(2021), 104951.

Bennett, R.H., Bryant, W.R., Hulbert, M.H., (1991). Microstructure of fine-grained sediments, Springer, New York.

Bennett, R.H., Bryant, W.R., Keller, G.H., (1981). Clay fabric of selected submarine sediments: fundamental properties and models. Journal of Sedimentary Petrology. 51(1), 217-232.

Birgenheier, L.P., Horton, B., McCauley, A.D., Johnson, C.L., Kennedy, A., (2017). A depositional model for offshore deposits of the lower Blue Gate Member, Manco Shale, Uinta Basin, Utah, USA. Sedimentology. 64, 1402-1438.

Boulesteix, K., Poyatos-More, M., Flint, S.S., Taylor, K.G., Hodgson, D.M., Hasiotis, S.T., (2019). Transport and deposition of mud in deep-water environments: Processes and stratigraphic implications. Sedimentology. 66, 2894-2925.

Broughton, P.L., (2018). Mudstone clast breccia in the Cretaceous Athabasca Oil Sands, western Canada: Fluvial debris-flows transitions into traction carpets. The Journal of Geology. 126(1), 63-97.

Bungartz, H., Wanner, S.C., (2004). Significance of particle interaction to the modelling of cohesive sediment transport in rivers. Hydrological Processes. 18, 1685-1702.

Carlough, L.A., (1994). Origins, structure, trophic significance of amorphous seston in a blackwater river. Freshwater Biology. 31, 227-237.

Carrigy, M.A., (1959). Geology of the McMurray Formation, part 3: general geology of the McMurray area. Research Council of Alberta. Geological Division, Edmonton, AB.

Chamley, H., (1989). Clay sedimentology. Berlin, Germany, Springer-Verlag.

Droppo, I.G., Ongley, E.D., (1994). Flocculation of suspended sediment in rivers of southeastern Canada. Water Research. 28(8), 1799-1809.

Droppo, I.G., Leppard, G.G., Flannigan, D.T., Liss, S.N., (1997). The freshwater floc: a functional relationship of water and organic and inorganic floc constituents affecting suspended sediment properties. Water Air and Soil Pollution. 99, 43-54.

Dunne, K.B.J., Nittrouer, J.A., Abolfazli, E., Osborn, R., Strom, K.B., (2024). Hydrodynamically-driven deposition of mud in river systems. Geophysical Research Letters. 51, e2023GL107174.

Durkin, P.R., Boyd, R.L., Hubbard, S.M., Shultz, A.W., Blum, M.D., (2017). Three-dimensional reconstruction o meander-belt evolution, Cretaceous McMurray Formation, Alberta foreland basin, Canada. Journal of Sedimentary Research. 87(10), 1075 – 1099.

Egenhoff, S.O., Fishman, N.S., (2013). Traces in the dark—Sedimentary processes and facies gradients in the upper shale member of the Upper Devonian-Lower Mississippian Bakken Formation, Williston Basin, North Dakota, U.S.A. Journal of Sedimentary Research. 83, 803-824.

Eisma, D., (1986). Flocculation and de-flocculation of suspended matter in estuaries. Netherland Journal of Sea Research. 20(2/3), 183-199.

Fall, K.A., Friedrichs, C.T., Massey, G.M., Bowers, D.G., Smith, S.J., (2021). The importance of organic content to fractal floc properties in estuarine surface waters: Insights from video, LISST, and pump sampling. Journal of Geophysical Research: Oceans. 126, e2020JC016787.

Flach, P.D., Mossop, G.D., (1985). Depositional environments of Lower Cretaceous McMurray Formation, Athabasca Oil Sands, Alberta. American Association of Petroleum Geologists Bulletin. 69(8), 1195-1207.

Fox, J.M., Hill, P.S., Milligan, T.G., Boldrin, A., (2004). Flocculation and sedimentation on the Po River Delta. Marine Geology. 203, 95-107.

Fox, J., Ford, W., Strom, K., Villarini, G., Meehan, M., (2014). Benthic control upon the morphology of transported fine sediments in a low-gradient stream. Hydrological Processes. 28, 3776-3788.

Garrels, R.M., Mackenzie, F.T., (1971). Evolution of sedimentary rocks: New York, Norton, XVI, 397.

Gerbersdorf, S.U., Jancke, T., Westrich, B., Paterson, D.M., (2008). Microbial stabilization of riverine sediments by extracellular polymeric substances. Geobiology. 6, 57-69.

Hein, F.J., Cotterill, D.K., (2006). The Athabasca Oil Sands – A regional geological perspective, Fort McMurray area, Alberta, Canada. Natural Resources Research. 15, 85-102.

Jarvis, P., Jefferson, B., Gregory, J., Parsons, S.A., (2005). A review of floc strength and breakage. Water Research. 39, 3121-3137.

Jiang, P., (2013). Pore morphometrics and thermal evolution of organic-matter microporosity, Colorado Group, Western Canada Foreland Basin. Electronic Thesis and Dissertation Repository. 1820.

Jordan, D.W., Pryor, W.A., (1992). Hierarchical levels of heterogeneity in a Mississippi River meander belt and application to reservoir systems: Geologic note 1. American Association of Petroleum Geologists Bulletin. 76(10), 1601-1624.

Kim, J., Peacor, D.R., Tessier, D., Elsass, F., (1995). A technique for maintaining texture and permanent expansion of smectite interlayers for TEM observations. Clays and Clay Minerals. 43(1), 51-57.

Kineke, G.C., Sternberg, R.W., (1995). Distribution of fluid muds on the Amazon continental shelf. Marine Geology. 125, 193-233.

Knapp, L.J., McMillan, J.M., Harris, N.B., (2017). A depositional model for organic-rich Duvernay Formation mudstones. Sedimentary Research. 347, 160-182.

La Croix, A.D., Dashtgard, S.E., MacEachern, J.A., (2019). Using a modern analogue to interpret depositional position in ancient fluvial-tidal channels: Example from the McMurray Formation, Canada. Geoscience Frontiers. 10(6), 2219-2238.

Lamb, M.P., Leeuw, J.D., Fischer, W.W., Moodie, A.J., Venditti, J.G., Nittrouer, J.A., Haught, D., Parker, G., (2020). Mud in rivers transported as flocculated and suspended bed material. Nature Geoscience. 13, 566-570.

Laycock, D.P., Pederson, P.K., Montgomery, B.C., Spencer, R.J., (2017). Identification, characterization, and statistical analysis of mudstone aggregate clasts, Cretaceous Carlile Formation, Central Alberta, Canada. Marine and Petroleum Geology. 84, 49-63.

Le, H., Gratiot, N., Santini, W., Ribolzi, O., Tran, D., Meriaux, X., Deleersnijder, E., Soares-Frazao, S., (2020). Suspended sediment properties in the Lower Mekong River, from fluvial to estuarine environments. Estuarine, Coastal and Shelf Science. 233, 106522.

Lee, B.J., Fettweis, M., Toorman, E., Molz, F.J., (2012). Multimodality of a particle size distribution of cohesive suspended particulate matters in a coastal zone. Journal of Geophysical Research. 117, C03014.

Leeder, M.R., (2009). Sedimentology and sedimentary basins: from turbulence to tectonics. John Wiley & Sons.

van Leussen, W., (2011). Macroflocs, fine-grained sediments transports, and their longitudinal variations in the Ems Estuary. Ocean Dynamics. 61, 387-401.

Li, Z., Schieber, J., (2018). Composite particles in mudstones: Examples from the Late Cretaceous Tunuk Shale Member of the Mancos Shale Formation. Journal of Sedimentary Research. 88, 1319-1344.

Liss, S.N., Droppo, I.G., Flannigan, D.T., Leppard, G.G., (1996). Floc architecture in wastewater and natural riverine systems. Environmental Science and Technology. 30(2), 680-686.

Macquaker, J.H.S., Bentley, S.J., Bohacs, K.M., (2010a). Wave-enhanced sediment-gravity flows and mud dispersal across continental shelves: Reappraising sediment transport processes operating ancient mudstone successions. Geology. 38(10), 947-950.

Macquaker, J.H.S., Bohacs, K.M., (2007). On the accumulation of mud. Science, 318, 1734-1735.

Macquaker, J.H.S., Keller, M.A., Davies, S.J., (2010b). Algal blooms and "marine snow": Mechanisms that enhance preservation of organic carbon in ancient fine-grained sediments. Journal of Sedimentary Research. 80, 934-942.

Martinius, A.W., Fustic, M., Garner, D.L., Jablonski, B.V.J., Strobl., R.S., MacEachern, J.A., Dashtgard, S.E., (2017). Reservoir characterization and multiscale heterogeneity modelling of inclined heterolithic strata for bitumen-production forecasting, McMurray Formation, Corner, Alberta, Canada. Marine and Petroleum Geology. 82, 336-361.

McAnally, W.H., Friedrichs, C., Hamilton, D., Hayter, E., Shrestha, P., Rodriguez, H., Sheremet, A., Teeter, A., (2007). Management of fluid mud in estuaries, bays, and lakes. I: Present state of understanding on character and behavior. Journal of Hydraulic Engineering. 133(1), 9-22.

Moon, C.F., (1972). The microstructure of clay sediments. Earth-Science Reviews. 8, 303-321.

Nghiem, J.A., Fischer, W.W., Li, G.K., Lamb, M.P., (2023). A mechanistic model for mud flocculation in freshwater rivers. Journal of Geophysical Research: Earth Surface. 127, e2021JF006392.

Nguyen, Q.H., Fettweis, M., Spencer, K.L., Byung, J.L., (2022). Flocculation with heterogenous composition in water environments: A review. Water Research. 213, 118147.

Nishida, N., Ito, M., Inoue, A., Takizawa, S., (2013). Clay fabric fluid-mud deposits from laboratory and field observations: Potential application to the stratigraphic record. Marine Geology. 337, 1-8.

Nouidar, M. & Chellaï, E.H., (2001). Facies and sequence stratigraphy of an estuarine incised-valley fill: Lower Aptian Bouzergoun Formation, Agadir Basin, Morocco. Cretaceous Research. 22, 93-104.

Odom, I.E., (1967). Clay fabric and its relation to structural properties in mid-continent Pennsylvanian sediments. Journal of Sedimentary Petrology. 37(2), 610-623.

Osborn, R., Dunne, K.B.J., Ashley, T., Nittrouer, J.A., Strom, K., (2023). The flocculation state of mud in the lowermost freshwater reaches of the Mississippi River: Spatial distribution of sizes, seasonal changes, and their impact on vertical concentration profiles. Journal of Geophysical Research: Earth Surface. 128, e2022JF006975.

Partheniades, E., (2009). Cohesive Sediments in Open Channels. 1st edition. Elsevier Inc., Burlington.

Pavan, K., (2019). Microfacies analysis of mudstone in a freshwater to marine transect: Upper Cretaceous Dunvegan and Kaskapau formations, Western Canada Foreland Basin. Electronic Thesis and Dissertation Repository. 6528.

Peng, Y., Durkin, P.R., Martin, H.K., Leckie, D.A., Horner, S.C., Hubbard, S.M., (2024). Early Cretaceous evolution of the McMurray Formation: A review toward a better understanding of the paleo-depositional system. Earth-Science Reviews. 252, 104740.

Plint, G.A., (2014). Mud dispersal across a Cretaceous prodelta: Storm-generated, wave-enhanced sediment gravity flows inferred from mudstone microtexture and microfacies. Sedimentology. 61, 609-647.

Plint, G.A., Macquaker, J.H.S., Varban, B.L., (2012). Bedload transport of mud across a wide, storm-influenced ramp: Cenomanian-Turkonian Kaskapau Formation, Western Canada Foreland Basin. Journal of Sedimentary Research. 82, 801-822.

Potter, P.E., Maynard, J.B., Depetris, P.J., 2005. Mud and Mudstones. Springer Berlin, Heidelberg, Germany.

Pryor, W.A., Vanwie, W.A., (1971). The “sawdust sand”—An Eocene sediment of floccule origin. Journal of Sedimentary Petrology. 41(3), 763-769.

Pryor, W.A., (1975). Biogenic sedimentation and alteration of argillaceous sediments in shallow marine environments. Geological Society of American Bulletin. 86, 1244-1254.

Sanchez-Roa, C., Bauluz, B., Nieto, F., Abad, I., Jimenez-Millan, J., Faulkner, D., (2018). Micro- and nano-scale study of deformation induced mineral transformations in Mg-phyllosilicate-rich fault gouges from Galera Fault Zone (Betic Cordillera, SE Spain). American Mineralogist, 103, 1604-1621.

Schieber, J., Southard, J., Kevin, T., (2007). Accretion of mudstone beds from migrating floccule ripples. Science. 318(5857), 1760-1763.

Schieber, J., Southard, J.B., (2009). Bedload transport of mud by floccule ripples—Direct observation of ripple migration processes and their implications. Geology. 37(6), 483-486.

Schofield, R.K., Samson, H.R., (1954). Flocculation of kaolinite due to the attraction of oppositely charged crystal faces. Discussion of the Faraday Society. 18, 135-145.

Shanks, A.L., (2002). The abundance, vertical flux, and still-water and apparent sinking rate of marine snow in a shallow coastal water column. Continental Shelf Research. 22, 2045-2064.

Slattery, M.C., Burt, T.P., (1997). Particle size characteristics of suspended sediment in hillslope runoff and stream flow. Earth Surfaces Processes and Landforms. 22, 705-719.

Soulsby, R.L., Manning, A.J., Spearman, J., Whitehouse, R.J.S., (2013). Settling velocity and mass settling flux of flocculated estuarine sediments. Marine Geology. 339, 1-12.

Sutherland, B.R., Barett. K.J., Gingras, M.K., (2015). Clay settling in fresh and salt water. Environmental and Fluid Mechanics. 15, 147-160.

Syvitski, J.P.M., Asprey, K.W., Leblanc, K.W.G., (1995). In-situ characteristics of particles settling within a deep-water estuary. Deep-Sea Research. 11(42), 223-256.

Tan, X., Hu, L., Reed, A.H., (2015). Flocculation and particle size analysis of expansive clay sediments affected by biological, chemical, and hydrodynamic factors. Ocean Dynamics. 64, 143-157.

Toonen, W.H.J., Kleinhans, M.G., Cohen, K.M., (2012). Sedimentary architecture of abandoned channel fills. Earth Surface Processes and Landforms. 37(4), 459-472.

Walling, D.E., Moorehead, P.W., (1989). The particle size characteristics of fluvial suspended sediment: an overview. Hydrobiologia. 176/177, 125-149.

Weilenmann, U., O'Melia, C.R., Stumm, W., (1989). Particle transport in lakes: Models and measurements. Limnology and Oceanography. 34(1), 1-18.

White, W.A., (1961). Colloid phenomena in sedimentation of argillaceous rocks. Journal of Sedimentary Petrology. 31(4), 560-570.

Winterwerp, J.C., (2002). On the flocculation and settling velocity of estuarine mud. Continental Shelf Research. 22, 1339-1360.

CHAPTER FOUR:

CONCLUSION

4.1. Summary of Research Findings

Understanding the processes involved in fluvial sedimentary environments is essential for optimizing modelling and predictive subsurface evaluations and interpretations. Knowledge gaps are evident, however, highlighted by localized modelling errors that often exist despite high resolution subsurface datasets. In order to contribute to the current understanding in fluvial sedimentology, the underlying process-to-product relationships are investigated from the scale of channel-belt and its architectural elements in chapter two, to the micron-scale in chapter three.

In chapter two, Kearl subsurface data (i.e., well-logs and core photographs) were combined with extensive outcrop investigation in the form of mine-face photography. Mine faces proved to be an excellent source of data because of their large-scale, vertical and lateral continuity, and they are not subjected to visual degradations from weathering. In addition, they are successively exposed in 2-D slices of the subsurface as mining progresses. The mine-face photographs are used to establish important linkages between traditional subsurface data and the sediments that data is derived from. The combination of outcrop and borehole data resulted in a comprehensive planform reconstruction of the paleoenvironment in the area of interest. Subsequently, a planview evaluation allowed for spatiotemporal interpretations of paleochannel morphodynamics and the resulting sedimentary record. The results produced an applicable reservoir-scale framework that can be utilized for evaluating subsurface architectural elements and facies distributions. The research focused on the presence of atypical point-bar deposits that did not fine upwards nor downstream, as typified by general point-bar models (e.g., Allen, 1965; Willis and Tang, 2010). The exceptional outcrop and subsurface data near the atypical deposits were integrated with an evaluation of paleochannel 3-D morphodynamics to aid in interpreting the newly documented atypical point-bar trend.

Atypical deposits comprised interbedded units of IHS, mudstone clast breccia, and trough cross-bedded sandstone lined with mudstone interbedding. The basal deposits were commonly densely dispersed mudstone clasts, and outcrop availability enabled the observation of mudstone clast sorting, grading and imbrication within trough cross-bedding units. These deposits are located near and downstream from the bend-apex, a location that normally features sandstone-dominated, upward and downstream fining deposition (e.g., Hagstrom et al., 2019).

During the atypical deposition, planform reconstruction maps indicate that the upstream cutbank began scouring into thick and erosionally resistant mudstone, resulting in a morphodynamic change in fluvial style from lateral expansion to downstream translation (e.g., Durkin et al., 2020; Sylvester et al., 2021). The consistently dense dissemination of mudstone clasts and their angular shapes likely indicate a short travel distance from a nearby mudstone-rich source (Broughton, 2018). Furthermore, mudstone clasts adhering to trough cross-bedding structures suggest they likely travelled as bedload material in tandem with sand particles. It is interpreted that the mudstone clasts in the atypical deposits were sourced from the upstream cutbank. With the presence of mudstone clast sizes ranging from boulder- to sand-sized in the atypical deposits, it is postulated that a further dissociation of mudstone clasts could have been present during deposition, though visual recognition at that scale becomes difficult (i.e., sub-sand-silt mudstone clasts, or mudstone aggregates). The presence of sub-sand-sized mudstone clasts here could help in addressing the presence of mudstone lining trough-shaped bedding in the atypical deposits; however, insufficient evidence was available for confirmation. It is evident, though, that the utility of planform reconstruction can be applied to greatly improve subsurface forecasting in meander-belt deposits, particularly when atypical deposits are encountered.

Chapter three comprises a method for and results from SEM microstructural investigation of a mudstone sample collected downstream from the atypical deposits in chapter two. The sampled mudstone was taken from the mudstone-component of IHS deposits. The research investigates whether sub-sand-sized mudstone clasts are present in fluvial deposits, and if so, do they typically appear as mudstone bedding (e.g., the mudstone component of IHS) in core and outcrop? In chapter two it is noted that mudstone clast size and abundance decreased from west to east, or downstream, towards the mudstone sample location for chapter three. An SEM investigation for sub-sand-sized mudstone aggregates in chapter three is then supplementary to a downstream-fining clast-size interpretation, with potential to link a gradational transition from mudstone clast breccia to IHS where the mudstone component is comprised of sub-sand-sized mudstone clasts (i.e., mudstone aggregates). With the growing evidence that mud travels as aggregates rather than individual particles (Droppo et al., 1997; Nguyen et al., 2022; Dunne et al., 2024), the research in chapter three is aimed to document the presence, or lack of, aggregates in the mudstone sample.

To conduct this investigation the mudstone sample was prepared for SEM imaging. Chapter three discusses the methodology that was developed to successfully treat the mudstone poorly-indurated mudstone for SEM analysis. Results show that microstructures appeared to have been preserved through the sampling and methodology processes herein.

SEM results indicate similarities in potential mudstone aggregate criteria developed from previous research conducted on marine mudstone, including the likely presence of domains (e.g., Bennett et al., 1981) and intraclastic aggregates (e.g., Plint, 2014). Domains are observed with a book-case style aggregation of flat clay particles, while intraclastic aggregates are recognized by the presence of aggregate margins. The margins are interpreted by evidence of pore space or

microfracturing, and clay mineral alignment to the apparent aggregate margins (e.g., Jiang, 2013; Plint, 2014; Laycock et al., 2017). It is notable, however, that the results are of less confidence than the images they are compared to because they have relatively poorer image resolution. Lower SEM image quality is attributed to the poorly-indurated condition of the mudstone sample and the sanding and polishing technique that was used on the exposed surface, possibly damaging the delicate texture of the mudstone, and the use of a low vacuum seal in the SEM.

In conclusion, the results from chapter two and three inform current fluvial meander-belt models by introducing atypical mudstone-rich deposit trends and strengthening well known point-bar trends elsewhere in the area of interest. In addition, evidence is presented that suggests mudstone clasts and, perhaps, sub-sand-sized mudstone aggregates, are deposited in energy regimes hydrodynamically equivalent to sand grains. Without the aid of microstructural analysis, however, sub-sand-sized mudstone aggregates are difficult, if not impossible, to view. The presence of mudstone aggregates in fluvial deposits is important because, if true, a wider range of physical conditions need to be considered for mudstone bedding, particularly within IHS mudstone interbeds, and elsewhere in fluvial environments.

4.2. Future Work

The utility of planform reconstruction is displayed in chapter two. Future studies with similar data sets could integrate the methods that were adopted to investigate the atypical deposits observed at Kearl. The atypical deposits were first recognized by on-site geologists focusing on areas in the mine with significant modelling errors (i.e., discrepancies in ore volume between modelled and mined material). By building a 3-D framework through planform reconstruction and then targeting the localized features that appear atypical, knowledge gaps in

fluvial sedimentology may be bridged by diagnosing the processes that would have taken place during deposition.

The final interpretation of atypical point-bar deposits resulting from mudstone-rich cutbank erosion in chapter two was based comprehensive evidence and interpretation, but a larger sample size is needed to verify the regularity of this trend. Laboratory models by Friedkin (1945) showed that cutbank material was transported and deposited on the downstream point bar on the *same side* of the cutbank, but processes may differ in nature. Since there are adequate criteria for recognizing counter-point bars using modern imaging and ancient rock data sets, and counter-point bars commonly suggest the presence of erosionally resistant cutbank material; investigating point-bar lithologies downstream from counter-point-bar deposits could potentially verify the atypical deposit trends documented in chapter two.

Counter-point-bar deposits are of particular importance in understanding subsurface permeability of meander-belt deposits because they comprise mudstone-rich sediments similar to abandoned-channel fills. In chapter 2, AEV is a counter-point bar that was initiated once the upstream meander bend was cut-off. Satellite image analyses by Sylvester et al. (2021) captures this process, documenting rapid downstream translation away from the cut-off. They note that counter-point bars occupy lower surface elevations, probably a result of lower deposition rates along the concave bank relative to rapid channel migration. In cross sections B-B', well 2; and D-D', wells 4 and 5; evidence of counter-point-bar deposition overlain by channel fill deposition is evident in dip-meter. FA3 IHS bedding dips in accordance with the nearby interpreted counter-point bar in the bottom-half of the interval but is then overlain by FA4 deposits of a different dip direction, suggesting the remaining upper portion of the interval is sediment filling accommodation on the floodplain (i.e., floodplain lake or swamp), more similar to an

abandoned-channel fill. The resulting planform shape of abandoned-channel fill deposit distribution would then be irregular, comprising the typical horse-shoe shape with an elongate body branching from the cut-off location, in the downstream direction. These criteria could be applied for the recognition of meander neck cut-off locations and mudstone-rich subsurface deposits that have abandoned-channel fills adjacent to counter-point bars, in similar styles observed in Sylvester (2021) and herein.

Further research is recommended to improve confidence in the presence of mudstone aggregates in fluvial deposits. As stated in chapter three—The sampled mudstone was poorly-indurated, more similar in competency to modern muds than ancient shales. The methodology in chapter three, therefore, may present successful results if attempted with adequately compacted modern muds. The ability to sample modern muds would drastically change the availability of potential samples for microstructure investigations of fluvial muds. Furthermore, due to time shortages in the present study the mudstone samples were not carbon coated and SEM imaging was conducted using a low vacuum seal. It may be beneficial in future attempts to use carbon coating and a high vacuum seal to produce sharper images.

4.3. References

Allen, J. R. L., (1965). Fining-upwards cycles in alluvial successions. Geological journal. 4(3), 229-246.

Bennett, R.H., Bryant, W.R., Keller, G.H., (1981). Clay fabric of selected submarine sediments: fundamental properties and models. Journal of Sedimentary Petrology. 51(1), 217-232.

Broughton, P.L., (2018). Mudstone clast breccia in the Cretaceous Athabasca Oil Sands, western Canada: Fluvial debris-flow transitions into traction carpets. The Journal of Geology. 126, 63-97.

Durkin, P.R, Hubbard, S.M., Holbrook, J., Weleschuk, Z., Nesbit, P., Hugenholtz, C., Lyons, T., Smith, D.G., (2020). Recognizing the product of concave-bank sedimentary processes in fluvial meander-belt strata. Sedimentology. 67, 2819-2849.

Friedkin, J., (1945). A Laboratory Study of the Meandering of Alluvial Rivers, Technical Report, May 1945. U.S. Army Corps of Engineers Waterworks Experimental Station: Vicksburg, MI.

Hagstrom, C.A., Hubbard, S.M., Leckie, D.A., Durkin, P.R., (2019). The effects of accretion-package geometry on lithofacies distribution in point bar deposits. Journal of Sedimentary Research. 89, 381-398.

Jiang, P., (2013). Pore morphometrics and thermal evolution of organic-matter microporosity, Colorado Group, Western Canada Foreland Basin. Electronic Thesis and Dissertation Repository. 1820.

Laycock, D.P., Pederson, P.K., Montgomery, B.C., Spencer, R.J., (2017). Identification, characterization, and statistical analysis of mudstone aggregate clasts, Cretaceous Carlile Formation, Central Alberta, Canada. Marine and Petroleum Geology. 84, 49-63.

Plint, G.A., (2014). Mud dispersal across a Cretaceous prodelta: Storm-generated, wave-enhanced sediment gravity flows inferred from mudstone microtexture and microfacies. Sedimentology. 61, 609-647.

Sylvester, Z., Durkin, P.R., Hubbard, S.M., Mohrig, D., (2021). Autogenic translation and counter point bar deposition in meandering rivers. The Geological Society of America. 133(11/12), 2439-2456.

Willis, B.J., Tang, H., (2010). Three-dimensional connectivity of point bar deposits. Journal of Sedimentary Research. 80, 440-454.

APPENDIX

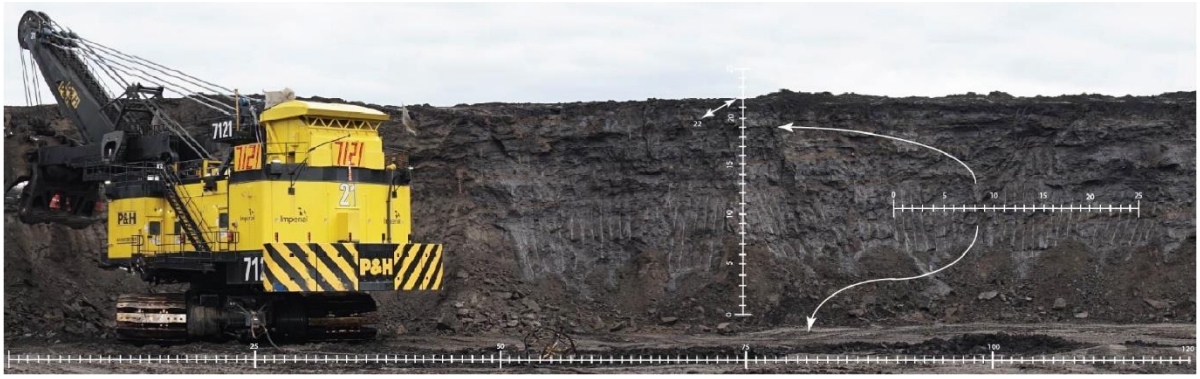

i) Scaling methodology used in outcrop photographs. Shovel-teeth spacing was measured and used to apply an accurate scale to the outcrops.

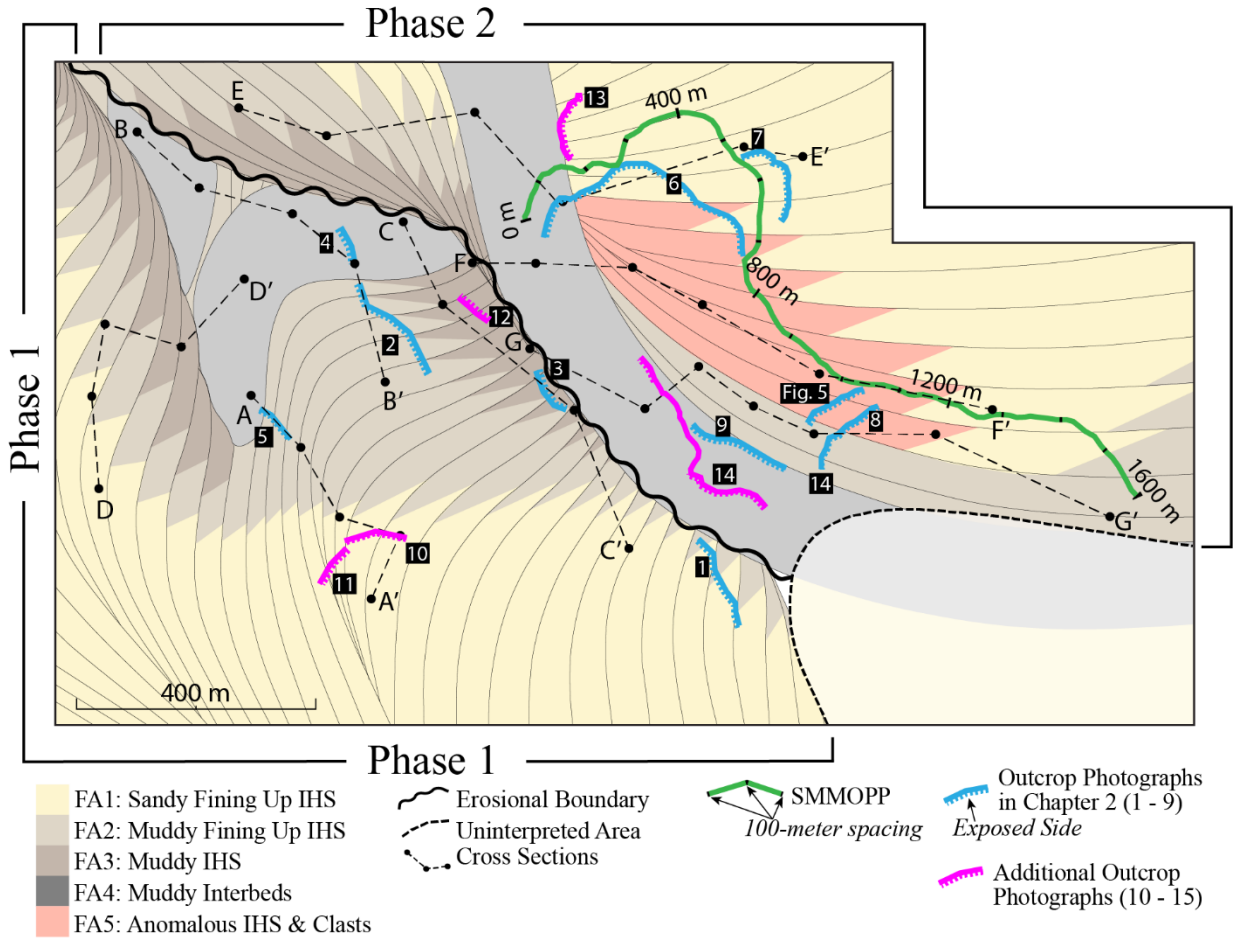

ii) Map of the area of interest in Chapter 2. This version of the map shows additional outcrop photograph locations (pink lines).

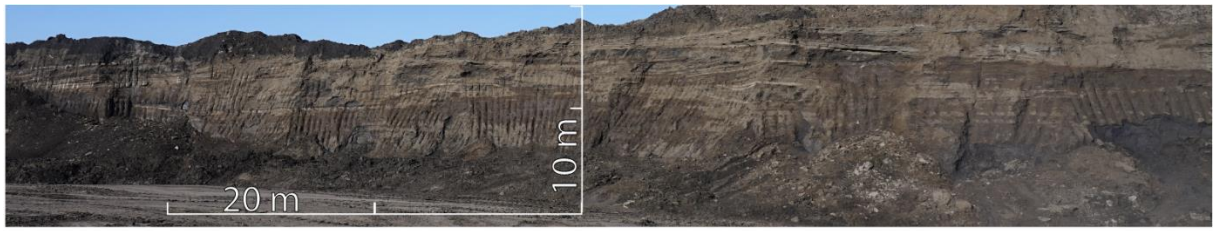

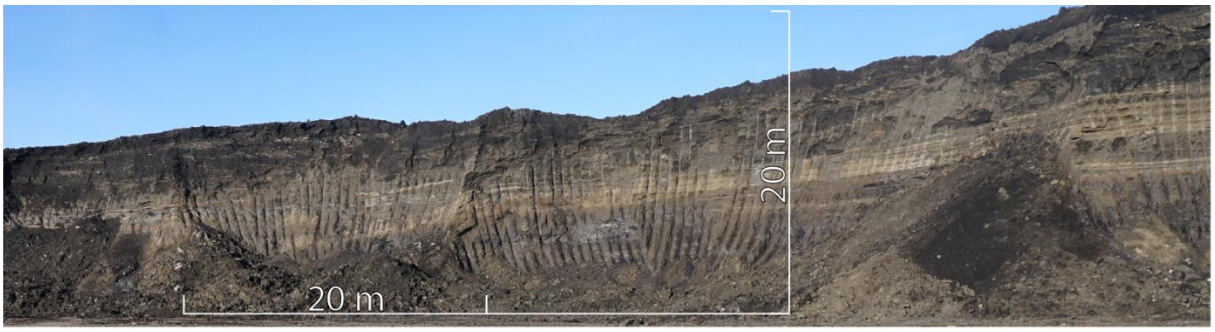

iii) Outcrop 10 and 11. Both outcrops are sand-dominated IHS (FA1) in AEI, showing mud interbeds and bedding truncation that indicates point bar surface re-working.

iv) Outcrop 12. Counter point bar deposit located ~ 15 m above the base of M2, showing erosion of overlying M3 (black sandstone) in the top of outcrop.

v) Outcrop 13. IHS and clasts in AEVIII showing upward coarsening trend.

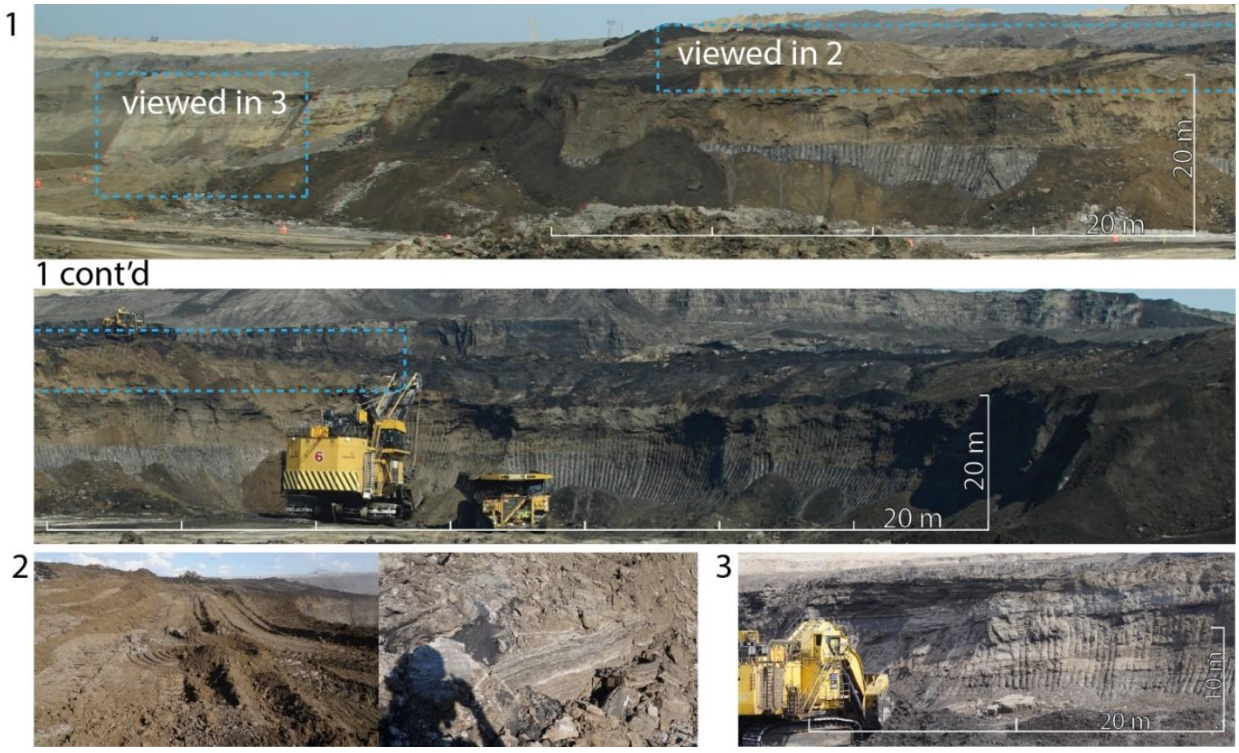

vi) Outcrop 14. Mudstone and heterolithic deposits from AEIX, abandoned-channel fill. 1) Shows a wide-angle view of the outcrop and areas where (2) and (3) are zoomed in to. Bottom of outcrop is sandstone dominated, overlain by the mudstone-rich material on the upper bench. 2) Image on the right shows the mudstone-rich floor on the upper bench that has been pushed around by a dozer. Image on the left is a sample of the mudstone-rich sediment that was picked up by the dozer. 3) Zoomed in view of the far outcrop on the left of (1). This outcrop shows a ~ 4 – 5 m-thick mudstone geobody that comprises roughly the same geometry as the mudstone geobody observed in Figure 2.16A.

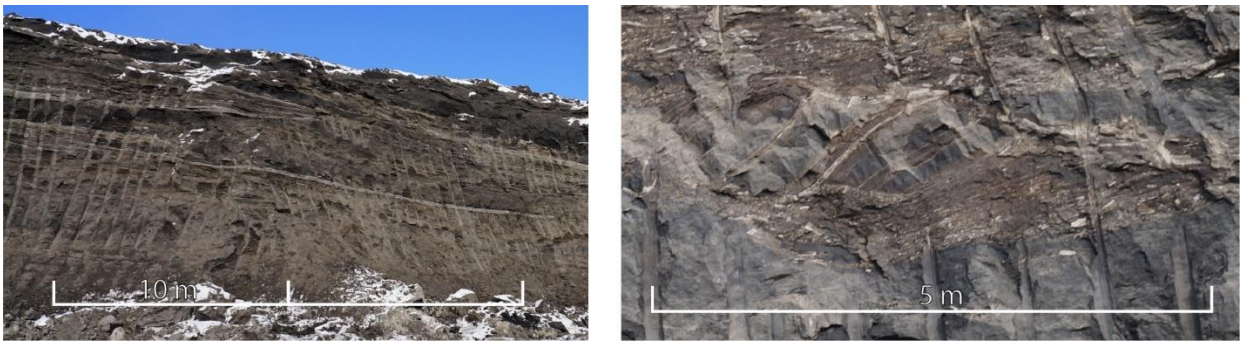

vii) Higher resolution photos from the NECOP, 905 – 920, 962 – 965 (Figure 2.10). Image on the left shows point bar IHS bed truncation and potential reorientation. Image on the right shows a very large (> 3 m) clast with internal IHS bedding.

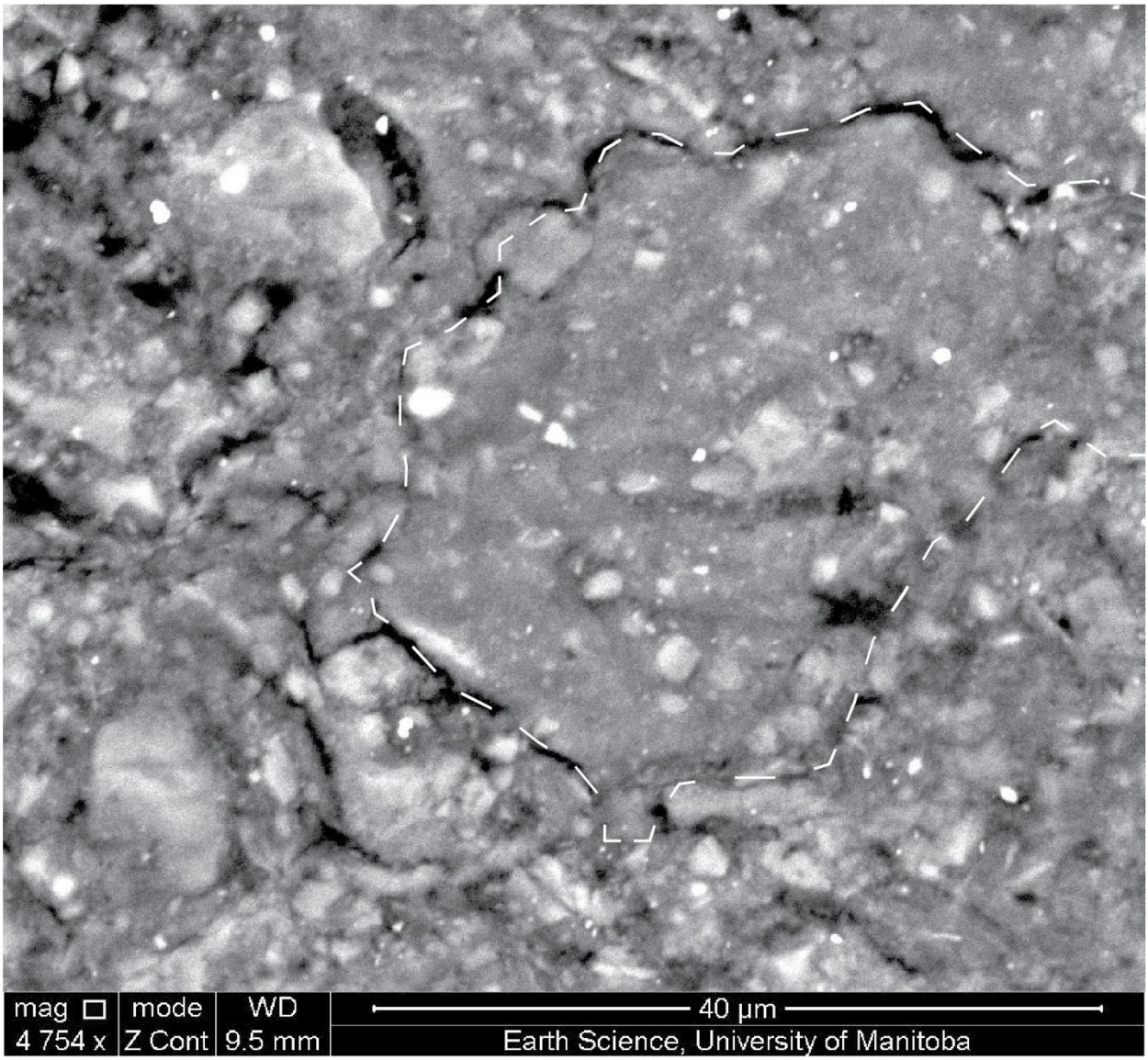

viii) Potential sample mudstone aggregate in horizontal section using SEM imaging from chapter 3. Boundary is traced by apparent pore space/ microfracture. Aggregate comprises illite matrix (grey), and clay-sized quartz (light grey).

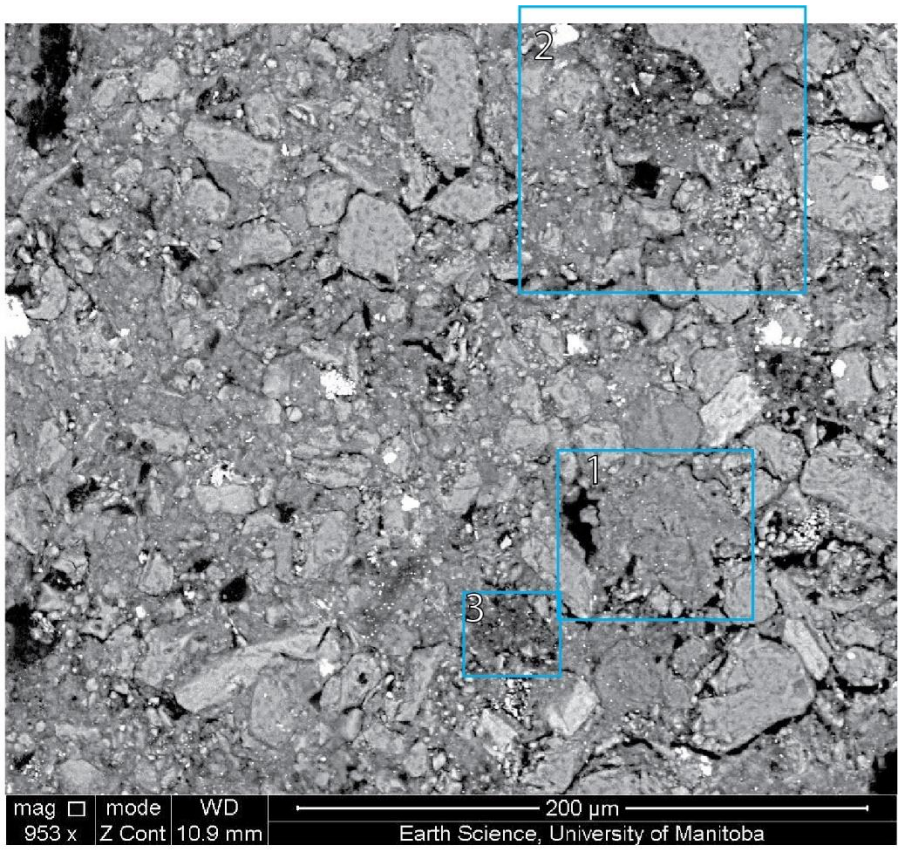
2
1
3
mag □ | mode | WD | 200 µm
953 x | Z Cont | 10.9 mm | Earth Science, University of Manitoba

1

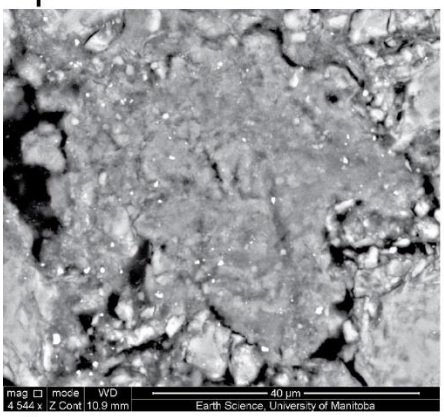
mag □ | mode | WD | 40 µm
4 542 x | Z Cont | 10.9 mm | Earth Science, University of Manitoba

2

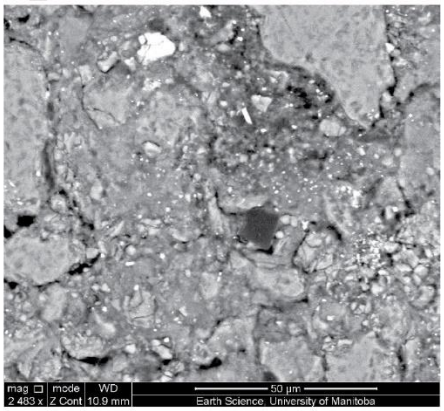
mag □ | mode | WD | 50 µm
2 483 x | Z Cont | 10.9 mm | Earth Science, University of Manitoba

3

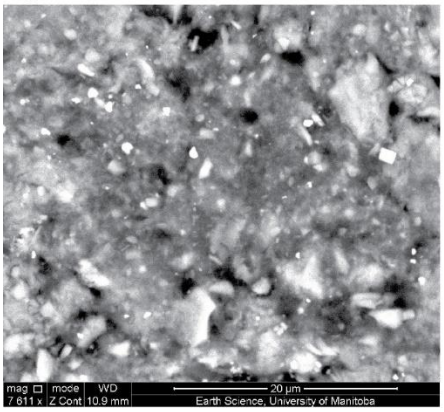
mag □ | mode | WD | 20 µm
7 611 x | Z Cont | 10.9 mm | Earth Science, University of Manitoba

ix) Potential sample mudstone aggregate examples in horizontal section using SEM images from chapter 3. 1, 2, and 3 image location are zoomed in from the top image, illustrated by blue rectangles. Images show aggregate boundaries by darker boundaries that likely represent apparent pore space or microfracturing. Illite-rich matrix (grey) and minor silt- to clay-sized quartz, feldspar and pyrite constituent grains (lighter grey).

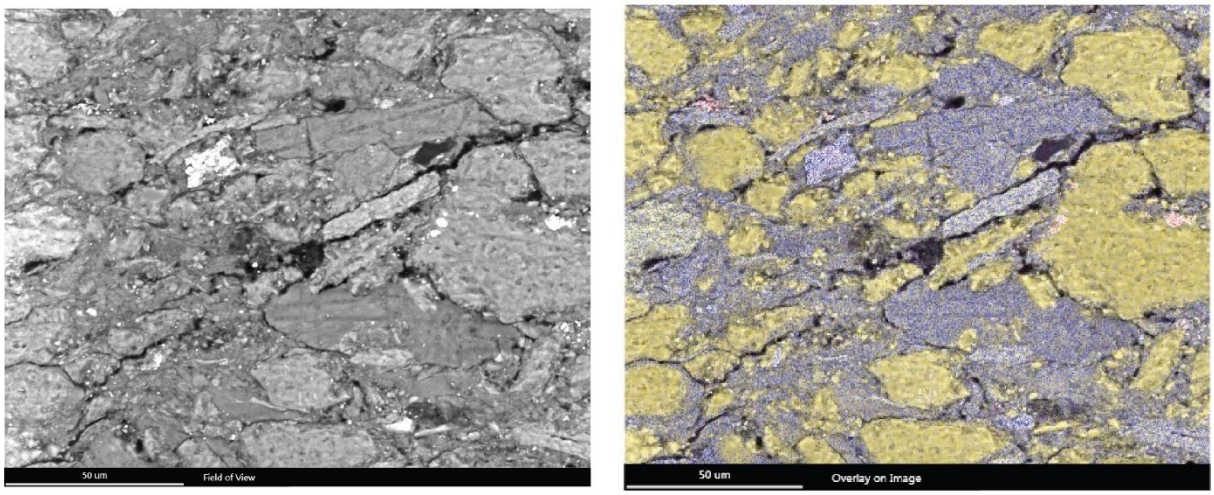

x) Microstructure features of mudstone sample in vertical section using SEM imaging from chapter 3. Right image shows element mapping. Yellow is Si, Blue is Al, Red is Fe.

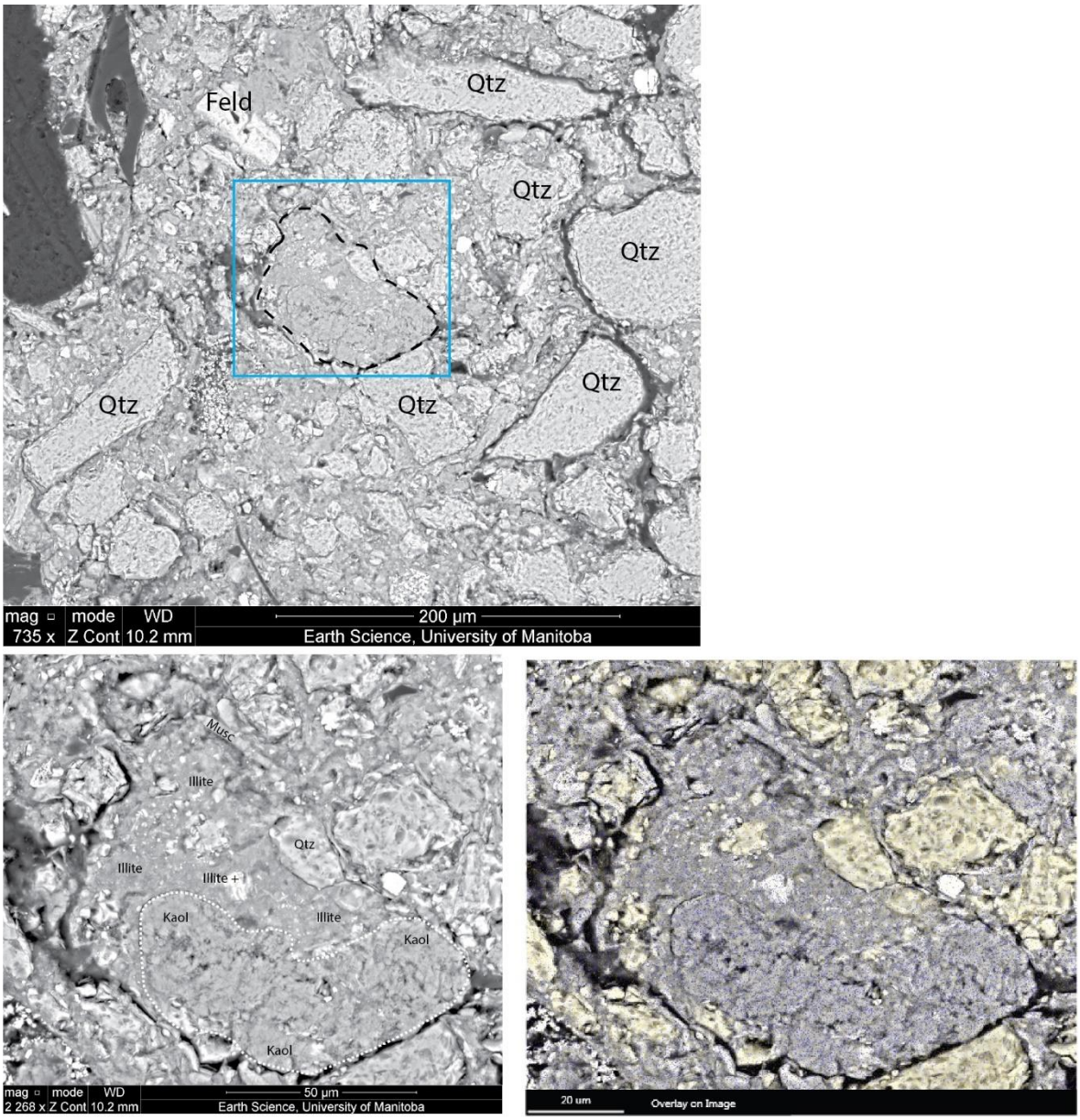

xi) Potential mudstone aggregate example in horizontal section using SEM imaging from chapter 3. The top image shows the wider shot of zoomed in locations (blue rectangle) of the bottom two images. Potential mudstone aggregate outlined with dotted black line. Bottom left shows potential mudstone aggregate and the labelled mineral constituents. The bottom right shows an element map of the same image. Yellow is Si, blue is Al.